



D 4.1

DELIVERABLE

PROJECT INFORMATION

Project Title: **Harmonized approach to stress tests for critical infrastructures against natural hazards**

Acronym: **STREST**

Project N°: 603389

Call N°: FP7-ENV-2013-two-stage

Project start: 01 October 2013

Duration: 36 months

DELIVERABLE INFORMATION

Deliverable Title: **D4.1. Guidelines for performance and consequences assessment of single-site, high-risk, non-nuclear critical infrastructures exposed to multiple natural hazards**

Date of issue: November 11, 2015

Work Package: WP4 – Vulnerability models for the performance and consequences assessment in stress tests of CIs

Deliverable/Task Leader: Ernesto Salzano (AMRA)

Reviewer: Elisabeth Krausmann (Joint Research Centre)
Bodizar Stojadinovic (ETH, Zurich)

REVISION: FINAL



Project Coordinator: Prof. Domenico Giardini
Institution: ETH Zürich
e-mail: giardini@sed.ethz.ch
fax: + 41 446331065
telephone: + 41 446332610

Abstract

Critical infrastructures are crucial for the sustainment and development of human activities. In this framework, Deliverable 4.1 is a core task within WP4. It addresses the definition of quantitative and standardized procedures and tools, which are propaedeutic to the hazard assessment and consequence analysis of the three selected single-site CI classes, namely industrial critical infrastructures (CI-A1), dams (CI-A2) and industrial harbours (CI-A3) when impacted by earthquakes and tsunamis, starting from intensity measures/scenarios related to two natural events.

For industrial installations, the occurrence of earthquakes and tsunamis may be dramatic. Indeed, any release of content results primarily in economic losses due to business (service) interruption and repair costs, but may also evolve towards severe catastrophic scenarios, such as environmental disasters, toxic dispersions, fires or explosions, depending on the hazard of the stored, processed or transported fluid, the structural design, and type of operation (NaTech risks).

A similar application has been developed for large dams. A methodology has been proposed as a step to obtain overall risk estimates for dams, which was applied to a conceptual large alpine embankment dam. Particular emphasis was placed on the model of the dam-reservoir system and its elements' vulnerability, as well as on the steps needed to characterize the impact of dam-break floods in downstream areas.

Finally, the effects of tsunami wave on warehouses, possibly containing hazardous substances, were assessed for industrial harbours.

Keywords: *NaTech, Industry, Port, Dam, Vulnerability function, Earthquake, Tsunami, Quantitative Risk Analyses, Fragility, Damage states, Risk states, Industrial installation, Non-nuclear stress test*

Acknowledgments

The research leading to these results has received funding from the European Community's Seventh Framework Programme [FP7/2007-2013] under grant agreement n° 603389.

Deliverable Contributors

ARMA Ernesto Salzano

Anna Basco

AUTH Stella Karafagka

Stavroula Fotopoulou

Kyriazis Pitilakis

Anastasios Anastasiadis

EPFL José P. Matos

Anton J. Schleiss

Table of Contents

1	Introduction	1
2	CI-A1: ENI/Kuwait oil refinery and petrochemical plant, Milazzo (IT)	3
2.1	INTRODUCTION	3
2.2	NATURAL HAZARD	4
2.2.1	Earthquake	4
2.2.2	Tsunami.....	5
2.3	TECHNOLOGICAL HAZARD	7
2.4	VULNERABILITY MODEL	10
2.4.1	Technological hazard with respect to earthquake	13
2.4.2	Technological hazard with respect to tsunami.....	31
2.4.3	Vulnerability to tsunamis debris	43
3	CI-A2: Large dams in the Valais region of Switzerland.....	47
3.1	INTRODUCTION	47
3.1.1	Main components of risk evaluation efforts for large dams	50
3.1.2	Traditional approaches for risk assessment of large dams	52
3.1.3	Overview of this contribution	53
3.2	METHODOLOGY FOR THE PERFORMANCE ASSESSMENT	54
3.2.1	The Generic Multi-Risk (GENMR) framework	54
3.2.2	Description of the studied conceptual dam.....	56
3.2.3	Natural Hazards.....	57
3.2.4	Critical infrastructure.....	63
3.2.5	Dam-reservoir system	66
3.2.6	Vulnerability model	68
3.2.7	Vulnerability functions.....	69
3.2.8	Flood routing.....	77
3.2.9	Risk model.....	84
3.2.10	Uncertainties.....	90
4	CI-B3 - Port infrastructures of Thessaloniki, Greece.....	92
4.1	INTRODUCTION	92
4.2	METHODOLOGY.....	95
4.3	THESSALONIKI PORT INFRASTRUCTURES	96

4.4	TSUNAMI FORCES.....	103
4.4.1	Determination of tsunami loading (FEMA, 2008).....	103
4.4.2	Key assumptions for estimating tsunami loading	109
4.5	NUMERICAL MODELLING	110
4.6	FRAGILITY CURVES	116
4.6.1	Definition of limit damage states.....	116
4.6.2	Construction of fragility curves	123
4.7	DISCUSSION.....	130
5	Dissemination	131
6	References	132

List of Figures

Fig. 1.1 The process flow for the vulnerability function developed in D4.1 for the single-site industrial equipment.	1
Fig. 2.1 Summary of strong ground shaking and ground failure interaction mechanisms (adapted after O'Rourke & Liu, 1999).	22
Fig. 2.2 Fragility curves for steel pipelines under SGS for a) all dataset; b) small diameter ($D < 400$ mm) and c) large diameter pipelines ($D \geq 400$ mm).	27
Fig. 2.3 Probit curves for steel pipelines under SGS for a) All dataset; b) small diameter ($D < 400$ mm) and c) large diameter pipelines ($D \geq 400$ mm).	29
Fig. 2.4 Schematic representation of atmospheric cone roof storage tank analysed in this project (API 650, 2015).	32
Fig. 2.5 Fragility function for some atmospheric tanks among the set analysed in this project, vs energy flux of tsunami.	36
Fig. 2.6 Relative increment of fragility median vs height H of atmospheric tanks for two set of tanks with diameter $D = 7$ m and 12 m, respectively.	36
Fig. 2.7 Schematic representation of horizontal, cylindrical, pressurized vessel.	38
Fig. 2.8 Critical energy flux for the failure of saddle-free horizontal pressurised tank with respect to the capacity.	43
Fig. 2.9 The cumulative distribution function and the corresponding probit function Y vs Johnson number J	45
Fig. 3.1 Aerial view of the Taum Sauk dam following its overtopping and failure, in 2005. U.S. Geological Survey.	48
Fig. 3.2 Aerial view of part of the area affected by the Taum Sauk dam-break wave. U.S. Geological Survey.	48
Fig. 3.3 View of the village of Longarone, Italy, prior to the Vajont dam disaster, 1960. Unknown author.	49
Fig. 3.4 View of the village of Longarone, Italy, after the Vajont dam disaster, 1963. U.S. Army.	49
Fig. 3.5 Proposed framing of vulnerability and loss assessment for large dams. The analysis of potentially affected areas is downstream adds to the simulation of the dam system. The relationship between both "blocks" is achieved through flood wave routing.	56
Fig. 3.6 Medvedev-Sponheuer-Karnik (MSK) intensities of ground shaking admitted for the area under study.	58
Fig. 3.7 Peak ground accelerations (PGA) admitted for the area under study.	59
Fig. 3.8 Peak flood inflows to the reservoir.	60
Fig. 3.9 Probability density of a flood's duration.	61

Fig. 3.10 Normalized hydrograph of flood inflows.....	61
Fig. 3.11 Admitted probability of occurrence of a flood throughout the year	61
Fig. 3.12 Intensity of internal erosion events admitted for the dam under study.	62
Fig. 3.13 Expected inflows into the reservoir.	65
Fig. 3.14 Target volume of the reservoir throughout the year (normalized in respect to the volume of the reservoir at the spillway level).....	65
Fig. 3.15 Maximum outflows of the reservoir as a function of the normalized volume of the reservoir.	66
Fig. 3.16 Scheme of hazards, elements, system states, and interactions considered in the application of the GenMR framework to large dams. Adapted from Mignan et al. (2015) and presented in Matos et al. (2015).	67
Fig. 3.17 Example simulation of the dam-reservoir system affected by a 10 000 year flood and a 5 000 year return period earthquake. On top: reservoir volume evolution. In the middle: outflow evolution. In the bottom: element state evolution. Adapted from Matos et al. (2015).	68
Fig. 3.18 Vulnerability curve of the dam and foundation to earthquakes.....	70
Fig. 3.19 Vulnerability of the spillway element to earthquakes.	70
Fig. 3.20 Vulnerability of the bottom outlet element to earthquakes.....	71
Fig. 3.21 Vulnerability of the hydropower system to earthquakes.	71
Fig. 3.22 Distribution of the damage induced to the bottom outlet element by equipment malfunction.	72
Fig. 3.23 Distribution of the damage induced to the hydropower system by equipment malfunction.	73
Fig. 3.24 Damage functions for several building classes derived from real field observations collected after the Indian Ocean tsunami occurred on December 26, 2004 developed during project SCHEMA by GSC. Reproduced from (Tinti et al. 2011).	74
Fig. 3.25 Fragility curves derived by Suppasri et al. (2013) for two-stories reinforced concrete buildings.	75
Fig. 3.26 Scatter plot depicting inundation depths and flow velocities simulated by a 2D model applied to the dam-break problem.....	76
Fig. 3.27 Fragility curves admitted for road infrastructure.	76
Fig. 3.28 Illustration of the area analysed downstream of the dam and depiction of the numerical grid and computational sections of the coupled hydraulic BASEMENT model.....	78
Fig. 3.29 Comparison of computational mesh and building sizes.....	79
Fig. 3.30 Outflow hydrograph estimates used for hydraulic simulation.	80
Fig. 3.31 Illustration of numerical simulation results of a dam-break wave simulated following an overtopping and using average breach parameters. Colours represent inundation depth (m) and arrows flow velocity.	80

Fig. 3.32 Illustration of numerical simulation results of a dam-break wave simulated following an overtopping and using average breach parameters. Colours represent inundation depth (m) and arrows flow velocity.	81
Fig. 3.33 Detail of the tile coverage of the potentially inundated area.	82
Fig. 3.34 Average error surface for the regression of inundation depth as a function of capacity and kernel width.	83
Fig. 3.35 Examples of inundation depths estimated through the regression models fitted for several tiles. Points were numerically simulated. Lines correspond to interpolated values.	84
Fig. 3.36 Map of damages to reinforced concrete buildings of two stories corresponding to a specific dam-break event.	86
Fig. 3.37 Map of damages road infrastructure corresponding to a specific dam-break event.	87
Fig. 3.38 Map of annual expected damage to reinforced concrete buildings of two stories. .	88
Fig. 3.39 Map of annual expected damage to road infrastructure.	89
Fig.4.1 Flowchart of the proposed methodology.....	95
Fig.4.2 Plan view of the a) MRF and b) Dual RC buildings	98
Fig.4.3 Cross-sections of the (a) 2-storey, (b) 4-storey, (c) 9-storey MRF RC buildings and the (d) 2-storey Dual RC building, designed by the 1959 Greek seismic code ..	99
Fig.4.4 Photo of a typical warehouse of Thessaloniki Port.....	99
Fig.4.5 Plan view of the warehouse.....	100
Fig.4.6 Cross-section of the warehouse	100
Fig.4.7a) Photo of a typical container crane of Thessaloniki Port and b)3D schematic view of the analytical container crane model(Kosbab, 2010).	100
Fig.4.8 Overall dimensions and section assignments (defined in Table 4.3, Table 4.4) and Table 4.5) of the studied container crane (Kosbab, 2010).	101
Fig.4.9 Cross-sections employed in the container crane and its dimensions (Kosbab, 2010).	101
Fig.4.10 Buoyant forces on an overall building with watertight lower levels (FEMA, 2008)..	104
Fig.4.11 Hydrostatic force distribution and location of resultant (FEMA, 2008).....	104
Fig.4.12 Hydrodynamic force distribution and location of resultant (FEMA, 2008).....	105
Fig.4.13 Hydrodynamic impulsive and drag forces on components of a building subjected to inundation by a tsunami bore (FEMA, 2008).....	106
Fig.4.14 Waterborne debris impact force (FEMA, 2008)	106
Fig.4.15 Maximum flow velocity of depth, d , at the ground elevation, z , and maximum run-up elevation, R . The bottom curve represents the lower limit of maximum flow velocity (FEMA, 2008).....	108
Fig.4.16 A definition sketch for upward buoyant force exerted on an elevated floor (FEMA, 2008)	109

Fig.4.17 Numerical simulation of tsunami loading for the MRF 2-storey (a) bare-frame (b) infilled building.....	112
Fig.4.18 Numerical simulation of tsunami loading for the Dual 2-storey (a) bare-frame (b) infilled building.....	112
Fig.4.19 Numerical simulation of tsunami loading for the MRF4-storey (a) bare-frame (b) infilled building.....	113
Fig.4.20 Numerical simulation of tsunami loading for the MRF 9-storey (a) bare-frame (b) infilled building.....	114
Fig.4.21 Numerical simulation of tsunami loading for the warehouse	115
Fig.4.22 Numerical simulation of tsunami loading for the crane (WS: Water Side,LS: Land Side).....	115
Fig.4.23 Definition of limit states on the seismic capacity curves for the different structure typologies considered.....	119
Fig.4.24 Definition of limit states on tsunami capacity curves for the different structure typologies considered.....	121
Fig.4.25 Definition of limit states on tsunami capacity curves for the different structure typologies considered (continued).....	122
Fig.4.26 Inundation depth- steel strain relationships for the MRF 2-storey infilled building.	124
Fig.4.27 Fragility curves for the different RC building typologies considered.	127
Fig.4.28 Fragility curves for the warehouse and the crane	128
Fig.4.29 Comparison of the numerical tsunami fragility curves for the MRF 4-storey infilled building with the corresponding empirical ones of (Suppasri et al., 2013)(Great East Japan tsunami, RC-mixed structural material).....	128
Fig.4.30 Comparison of the numerical tsunami fragility curves for the MRF 4-storey bare-frame building with the corresponding empirical ones of (a) (Suppasri et al., 2011) (Indian Ocean tsunami in Thailand, RC-structures) and (b) (Suppasri et al., 2013) (Great East Japan, RC-structures).....	128
Fig.4.31 Comparison of the numerical tsunami fragility curves for the MRF 9-storey infilled building with the corresponding empirical ones of (Suppasri et al., 2013)(Great East Japan, RC-3stories or more).....	129
Fig.4.32 Comparison of the numerical tsunami fragility curves for the warehouse with the corresponding empirical ones of (Suppasri et al., 2013) (Great East Japan) for (a) steel-structures and (b) dispersion of collapsed steel structures.	129

List of Tables

Table 2.1 Technology hazard matrix	8
Table 2.2 List of chemicals, expressed by the hazard classification of CLP (EC 1272/2008) and the corresponding amount as given in the Seveso Directive (2002).	9
Table 2.3 Risk matrix for technological hazard as defined by HSE in UK (HSE, 2005).	13
Table 2.4 Earthquake failure modes and release intensity (RS3: large release; RS2: small release; RS1: un-relevant or very small release) for atmospheric storage tank. 15	
Table 2.5 Seismic probit coefficients and threshold values (PGA_k) for anchored atmospheric steel tanks.	16
Table 2.6 Seismic probit coefficients and threshold values (PGA_k) for unanchored atmospheric steel tanks.....	16
Table 2.7 Seismic probit coefficients and threshold values (PGA_k) for pressurized horizontal steel storage tanks.	17
Table 2.8 Seismic probit coefficients and threshold values (PGA_k) for pressurized reactors.	17
Table 2.9 Seismic probit coefficients and threshold values (PGA_k) for pumps.....	17
Table 2.10 Structural aspects in the seismic behaviour of pipelines	19
Table 2.11 Typical joints commonly used for pipelines. D = Nominal diameter; OAW = oxyacetylene welding; SAW = submerged arc welding.....	21
Table 2.12 Most common empirical fragility expressions for pipelines under SGS (S: steel; CI: cast iron; WJ: welded joints; FJ: flange joints). The terms a and b are the coefficients of Eq. 2.6).....	24
Table 2.13 Structural Damage States (DS) for steel pipelines.	25
Table 2.14 Risk States (RS) for pipelines. Φ = equivalent diameter.	25
Table 2.15 Fragility parameters for steel pipelines, welded joint.	26
Table 2.16 Probit coefficients and threshold values for steel pipelines, welded joint.	30
Table 2.17 Probit coefficients and threshold values for pipelines for liquid transportation. ...	30
Table 2.18 The values of the physical parameters used in this study. ρ_w = density of water, ρ_f = density of the liquid inside the tank (gasoline), Φ = filling level of the tank; k_w = tsunami hydrodynamic coefficient.	34
Table 2.19 Design criteria and key parameters derived from API 650 (2015) used to define tank geometry in the present study	35
Table 2.20 The values of the physical parameters adopted for the pressurised equipment. ρ_w = density of tsunami water, ρ_f = density of the liquid inside the tank, Φ = filling level of the tank, ρ_s = density of the steel.....	37

Table 2.21 Parameters adopted for the definition of tsunami effect on pressurised equipment	41
Table 2.22 Threshold values for damage for Johnson’s damage number J (Nurick & Martin, 1989).	44
Table 2.23 Constant values for the equations for fragment penetration.....	46
Table 3.1 Parameters of the log-normal vulnerability functions to earthquakes (PGA).	71
Table 3.2 Parameters of the log-normal vulnerability functions to malfunctions.....	73
Table 3.3 Parameters of the log-normal fragility curves admitted for road infrastructure.....	76
Table 3.4 Summary results of the application of the GenMR framework to the dam-reservoir system. Results rounded from Matos et al. (2015).....	85
Table 4.1 Characteristics of Thessaloniki port buildings.....	98
Table 4.2 Typologies of Thessaloniki RC port buildings.....	98
Table 4.3 Terminology of labeled elements adopted in Fig.4.8 (Kosbab, 2010)	102
Table 4.4 Dimensions of J100 built-up hollow box sections(Kosbab, 2010).....	102
Table 4.5 Dimensions of J100 tube sections(Kosbab, 2010).	103
Table 4.6 Dimensions of J100 built-up wide-flange sections(Kosbab, 2010).	103
Table 4.7 Mass and Stiffness Properties of Common Waterborne Debris (FEMA, 2008)...	107
Table 4.8 Structural damage state descriptions for RC frame buildings (Crowley et al., 2004).	118
Table 4.9 Structural damage state descriptions for warehouses (Steel Light Frames)(FEMA, 2004).	118
Table 4.10 Structural damage state descriptions for unanchored/rail-mounted port cranes (FEMA, 2004).	119
Table 4.11 Definition of limit states for the different RC building typologies considered	122
Table 4.12 Definition of limit states for the warehouse and the crane	123
Table 4.13 Parameters of fragility functions	125

1 Introduction

In the Description of Work of the STREST project, task 4.1 is considered as a core task within WP4. Indeed, it was specifically aimed at producing quantitative and standardized procedures and tools for the consequence analysis of two selected single-site CI classes, namely industrial critical infrastructures (CI-A1) and dams (CI-A2), starting from intensity measures/scenarios related to natural events produced in WP3.

The task was also intended to produce vulnerability functions for the selected CIs, from the component level (e.g., element-based-fragility) to the system level. The probabilistic vulnerability models accounted, if appropriate, for time-variant issues (e.g., aging and damage accumulation due to repeated shocks) in a consistent manner.

This report describes the main results of task 4.1 and it is divided in two main parts, namely: T4.1-CI-A1: ENI/Kuwait oil refinery and petrochemical plant, Milazzo, Italy, followed by AMRA, and T4.1-CI-A2: Large dams in the Valais region of Switzerland followed by EPFL. This deliverable includes also the contribution of AUTH, which has developed a methodology for the preliminary assessment of the vulnerability of warehouses to tsunamis, with specific reference to the Port of Thessaloniki (T4.1-CI-B1).

All the definitions and concepts described in the following use the same taxonomy as in Deliverable D4.4. Accident case studies and lessons learned from natural hazard impact on refineries, petrochemical plants, large dams and port areas can be found in STREST Deliverable D2.3 that discusses lessons learned from recent catastrophic events (Krausmann, 2014).

For the three sections (CI-A1, CI-A2 and CI-B1) the proposed development may be sketched in three main steps and sub steps as reported in Fig. 1.1.

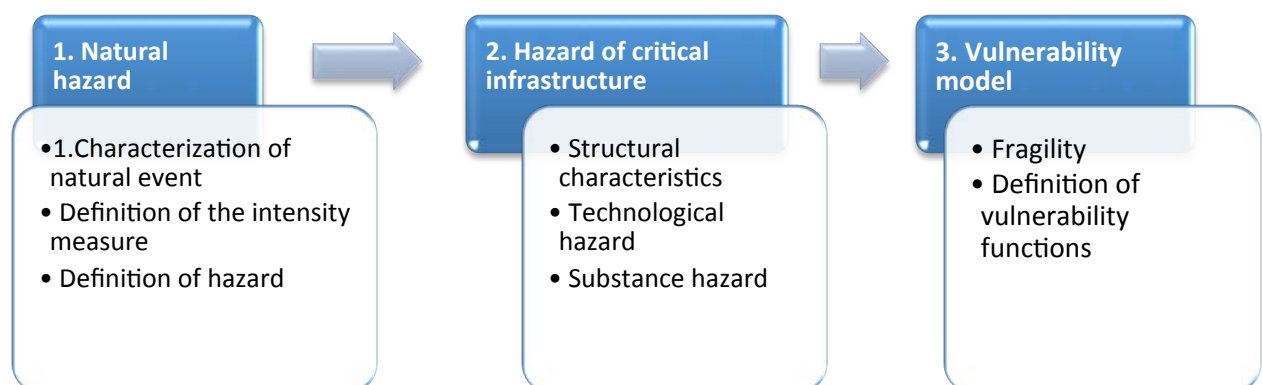


Fig. 1.1 The process flow for the vulnerability function developed in D4.1 for the single-site industrial equipment.

The step 1 reported in the previous figure may refer to one or more natural events for the same single site, each characterised by specific intensity measures and hazard. The evaluation of the hazards is the result of WP3, which is the starting point of the analysis reported in the following. Hence, they will be only briefly discussed in this deliverable. Regarding the choice of intensity measures, due to the large scale of natural events (regional, national, and international) and due to the number of assets to be analysed, a general procedure should consider a simple, cheap procedure. Hence, simplification is needed and a reduced number of intensity parameters has been chosen.

2 CI-A1: ENI/Kuwait oil refinery and petrochemical plant, Milazzo (IT)

2.1 INTRODUCTION

The CI-A1 will develop and demonstrate a risk assessment methodology for a single-site industrial installation when subjected to the impact of earthquakes and tsunamis, which can result in severe structural damage of equipment, warehouses and other infrastructures, and economic losses due to business interruption, clean-up, repair actions and more in general costs for the return-to-service.

To this aim, it is first essential to define structural vulnerability functions with respect to the two natural events of interest for industrial equipment and warehouses, to be implemented in the risk assessment tools. The structural vulnerability is certainly needed for return-to service in terms of costs but, however, the consequence of the natural events may be more dramatic if the industrial equipment or warehouses contain large amount of hazardous substances like fuels, toxic gases or even noxious substances, provided that the structural damage triggered by the natural event is sufficiently severe to result in the release of the hazardous content to the environment, and followed by fires, explosion, or environmental pollution.

These events are nowadays called NaTech events (Natural events triggering Technological accidents) (Salzano et al., 2013; Krausmann et al., 2011). NaTech events are typically characterised by the overloading of the emergency response due to the multiple, consequential and contemporary accidental events, which may seriously aggravate the damage propagation. In addition, the effectiveness of safety and emergency operations are prevented because of the failure of civil infrastructures (roads, bridges and so on) needed to reach the plant. Besides, strategic goods as fuels have to be saved. Finally, additional struggling to population may occur due to industrial events. Eventually, NaTech risks, have been now fully accepted as a fundamental contribution to the overall risk industrial risks worldwide (Krausmann et al., 2011; Salzano et al., 2013).

The methodology for the NaTech performance assessment of process industry is still discussed in the scientific community and needs to be clearly developed, starting from the state-of-art on the vulnerability assessment of industrial equipment. Quite clearly, due to the large scale of natural events (regional, national, and international) and due to the number of equipment to be analysed, the procedure must be simple, cheap and rapid, however based on sound engineering and science. Hence, simplification is needed either for the natural event characterisation or for the equipment.

2.2 NATURAL HAZARD

The methodology will be carried out firstly by identifying the hazard of two natural events, earthquake and tsunamis, through their characterisation, intensity measures, and relative hazard, with specific reference to the analysed critical infrastructure.

The analysis for the test case CI-A1 may be based on WP3 results. For the sake of single-site industrial installations, simplified measurement is however needed. To this aim, the Peak Ground Acceleration will be considered for earthquake, whereas the wave height and the wave speed, and their combination, will be considered for tsunami hazard characterization.

2.2.1 Earthquake

The interaction between earthquakes and equipment can result in large damages when hazardous industrial installations are involved. Quite clearly, NaTech procedures need multi-disciplinary effort, starting from the definition of probability of occurrence of earthquake intensity to the structural analysis for the equipment interaction with seismic actions, to the analysis of the specific response of the industrial process after the structural damage of equipment shell or supports has occurred, and finally to the evaluation of risks in global terms, following classical methodologies.

With specific reference to the seismic hazard, given the site of interest, ground motion is the main variable to take into account. More specifically, measured ground motions refer to seismic waves radiating from the earthquake focus to the site of interest and are related to the earthquake source, to the path for the seismic wave from the source to site, and to the specific geomorphologic characteristics of the site. Furthermore, the random feature of earthquakes includes energy, frequency contents, phases and many other variables, which may affect the structural response of structures.

Before quantitative seismology was developed, the seismic intensity was measured based on the damaging effects of the earthquake. Seismic intensity was mainly quantified by using the Modified Mercalli Intensity scale (MMI), which is still used nowadays for its practical implications. Quite obviously, this is not an objective scale, because the values are depending on the characteristics of the existing structural system and natural environment. Despite these limitations, several governmental agencies, as e.g. the U.S. Geological Survey (USGS), have produced MMI maps in order to describe the distribution of the earthquake effects in a given area. Therefore, many empirical relations for the performance of the structures during earthquakes, including pipelines, are dependent on MMI (Tromans, 2004).

More recently, the deployment of measurement stations on large regions has allowed the recording of the acceleration time history at the point of installation, and has addressed the use of more objective seismic parameters. Among others, the most significant, synthetic seismic parameter for structural applications is the Peak Ground Acceleration (PGA), which is the peak of the horizontal acceleration time history obtained from accelerometer measurements. For aboveground structures as buildings, the PGA is directly related to the structural damage, because of its proportionality with inertial effects due to the seismic loadings. Furthermore, empirical vulnerability analyses are often carried out in terms of PGA, as this parameter is relatively easy to infer by earthquake intensity conversion, and several extensive historical databases available on the damage due to earthquakes are usually

related to the PGA of the earthquake. Moreover, the calculation of this parameter from the typical earthquake magnitude metrics (e.g. the Modified Mercalli scale or the Richter scale) is straightforward.

Local and national authorities usually provide tools for PSHA (Probabilistic Seismic Hazard Analysis) (Cornell, 1968; Bommer, 2002) both in Europe and in the USA (<http://www.usgs.gov>). Hence, the exceedance probability of PGA occurrence calculated over 1 year or 50 years basis is nowadays available.

The exceedance probability curve is the general reference function for structural design purposes. In fact, seismic loads are usually determined from the maximum PGA of an earthquake in the site of interest over a given time periods.

When pipelines or underground structures are of concern, the damaging effects due to the passage of seismic waves in the soil are generally proportional to the Peak Ground Velocity (PGV), which is the peak value of the horizontal velocity time histories and which is less sensitive to the higher frequency component of the ground motion.

Quite clearly, the PGA and PGV are only a synthetic description of a seismogram and do not give a complete description of the local ground motion, in terms of frequency content and signal duration, which are also important parameters for the structural response. However, these instrumental, synthetic parameters are frequently used to relate structural damage and seismic intensity for their simplicity and clarity. Furthermore, the deterministic values of PGA and PGV often do not correspond to the damaged sites, with respect to the seismogram location. For this reason, it is necessary to use special predictive relations, which give an estimation of selected seismic site dependent parameter, based on other synthetic parameters, like magnitude, epicentre distance and ground conditions. These expressions are commonly called attenuation laws. A large review of the existing attenuation equations, both for ground motion parameters and spectral ordinates, is given and discussed by Douglas (2004). By using attenuation laws for each specific seismic region and instrumental information provided by the seismic network, the values of PGA and PGV may be obtained and plotted on shake maps, similarly to MMI maps.

Other details on seismic hazard and near-source analysis can be found in D3.3 of the STREST project.

2.2.2 Tsunami

A tsunami (lit. "harbour wave") is a series of water waves caused by the displacement of a large volume of a body of water generated by earthquakes, volcanic eruptions, landslides and other disturbances above or below water.

Tsunamis caused by earthquakes are the most important and frequent. In this case, the waves have small amplitude (the wave height above the normal sea surface), and a very long wavelength (often hundreds of kilometres long), whereas normal ocean waves have a height of roughly 2 meters and a wavelength of only 30 or 40 meters. Such waves travel over 800 kilometres per hour in open sea, but owing to the enormous wavelength, the wave oscillation at any given point takes 20 or 30 minutes to complete a cycle and has amplitude of less than 1 meter. Hence, tsunamis are generally difficult to detect over deep water, where ships are unable to feel their passage (FEMA, 2008).

Quite clearly, tsunamis grow in height when they reach shallower water. Indeed, as the tsunami approaches the coast, its speed decreases below 80 kilometres per hour, wavelength diminishes to less than 20 kilometres and its amplitude grows enormously. Although the impact of tsunamis is generally limited to coastal areas, their destructive power can be enormous and they can affect entire ocean basins. The 2004 Indian Ocean tsunami was among the deadliest natural disasters in human history with over 230,000 people killed in 14 countries bordering the Indian Ocean.

Tsunami waves do not resemble normal sea waves, because their wavelength is far longer. Rather than appearing as a breaking wave, a tsunami may instead initially resemble a rapidly rising tide, and for this reason, they are often referred to as tidal waves, with periods ranging from minutes to hours.

When the tsunami's wave peak reaches the shore, the resulting temporary rise in sea level is termed run-up. Run-up is measured in meters above a reference sea level. A large tsunami may feature multiple waves arriving over a period of hours, with significant time between the wave crests. The first wave to reach the shore may not have the highest run up.

All waves have a positive and negative peak, i.e. a ridge and a trough. In the case of a propagating wave like a tsunami, either may be the first to arrive. If the first part to arrive at shore is the ridge, a massive breaking wave or sudden flooding will be the first effect noticed on land. However if the first part to arrive is a trough, a drawback will occur as the shoreline recedes dramatically, exposing normally submerged areas. Drawback can exceed hundreds of meters, and people unaware of the danger sometimes remain near the shore to satisfy their curiosity or to collect fish from the exposed seabed.

A typical wave period for a damaging tsunami is about 10-12 minutes. This means that if the drawback phase is the first part of the wave to arrive, the sea will recede, with areas well below sea level exposed after 3 minutes. During the next 6 minutes, the tsunami wave trough builds into a ridge. During this time, the sea is filled in and destruction occurs on land. During the final next minutes, the tsunami wave changes from a ridge to a trough, causing floodwaters to drain and drawback to occur again. This may sweep victims and debris some distance from land. The process repeats as the next wave arrives.

Tsunamis cause damage by two mechanisms: i) the smashing force of a wall of water travelling at high speed, and ii) the destructive power of a large volume of water draining off the land and carrying a large amount of debris with it, even with waves that do not appear to be large.

From the engineering point of view, the tsunami action needs to be evaluated in terms of action on the structures and proper intensity parameters must be accounted for. In the common design practice, the main relevant parameters are the maximum water height, h_w , and the maximum water velocity, v_w . In the following, as for many flooding and tsunami analyses, we have adopted an intensity variable which is a combination of the two variables and more specifically the energy flux (J/m^2) which is the product of water density, h_w and v_w^2 .

Tsunami Hazard is a measure of the potential for a tsunami to occur at a given site. More details can be found in D3.1 of STREST project.

2.3 TECHNOLOGICAL HAZARD

Within the chemical process industry, different equipment exists, each characterised by different structural characteristics and functions. In addition, any chemical process is intended to convert raw materials or intermediate products to final products. Hence, the hazard of the substance, during processing or storage, has to be evaluated, too.

The primary sources that have the propensity to cause accidents can be determined either using the safety report of the plant or through existing risk assessment documentation. However, the selection of relevant hazardous equipment is an important step of the risk analysis procedure, because it allows the reduction of the costs and time needed for the application of the method.

For the aims of this project, equipment have been then categorized in three classes with respect to the design standard: i) Atmospheric equipment (storage tank and process); ii) Pressurised equipment (cylindrical buried; cylindrical over-ground; spheres); and iii) Pipeline system. The following sections will be devoted to these three types of equipment only.

Atmospheric storage tanks are constructed worldwide based on API 650 (2015) and are geometrically characterised as vertical cylinder. Other atmospheric process equipment as distillation towers, separation units, or cyclones, are also designed with similar procedures however with slender geometry. For the structural point of view, all these types of equipment are generally built with carbon or stainless steel, with typical Maximum Allowable Working Pressure and corresponding failure pressure of few milli-bars. Shell thicknesses range from 5 mm to about 1 cm for some sections of jumbo tanks.

Pressurised equipment is often adopted for very hazardous substances and it is geometrically characterised as cylindrical (buried or over-ground) or spheres. The thickness, and the corresponding design pressure, are clearly larger than atmospheric equipment and may reach several centimetres for small equipment like chemical reactors.

Finally, the pipeline system within the installation may be aboveground or buried. Any release from natural-event triggered ruptures may result in severe scenario. Pipelines may be continuous or segmented and are typically built from carbon or stainless steel when transporting hazardous or noxious substances.

Quite clearly, the technological hazard cannot neglect the hazards associated with the intrinsic chemical and physical hazards related to the processed or stored substances. Equipment items processing or storing flammable/toxic, highly flammable/toxic or extremely flammable/toxic substances according to the Classification, Labelling and Packaging Regulation (CLP-Regulation (EC) No 1272/2008), have surely to be considered as relevant sources of accidental events. Interestingly, studies have shown that earthquake-triggered structural damage involving water tanks is very similar to tanks containing hazardous materials and their behaviour can be described by a very similar methodology.

Besides, the physical state (gas, liquid, solid) and the operating conditions, which depend on the specific analysed process, are of also extreme importance. Eventually, a hazard matrix has been first developed and may be adopted for risk assessment (Table 2.1).

Table 2.1 Technology hazard matrix

1: low 4: high	Liquefied gas	Overheated Liquid	Gas	Cryogenic liquid	Liquid
Pressurised	4	3	3	2	1
Atmospheric	4	3	2	2	1
Pipeline	3	2	2	2	1

This result may be used for prioritizing the case study and the consequence assessment, as described in the Quantitative Risk Analysis developed in D5.1 of this project, but must be crossed with the chemical hazard.

To this aim, the REACH Regulation (the Regulation on Registration, Evaluation, Authorisation and Restriction of Chemicals of the European Union, adopted to improve the protection of human health and the environment from the risks that can be posed by chemicals) is useful, if added to the information given by the Seveso Directives (e.g. Dir 2012/18/EU of the European Parliament and of the Council of 4 July 2012 on the control of major-accident hazards involving dangerous substances, amending and subsequently repealing council directive 96/82/EC) and with CLP (Guidance to Regulation (EC) No 1272/2008 on classification, labelling and packaging (CLP) of substances and mixtures, Version 4.1, June 2015, ECHA-15-G-05-EN). Indeed, the CLP informs on the hazard characteristic for any substance, and the Seveso Directives includes a list of chemicals and related threshold amount to consider the same chemicals as dangerous for workers, population and environment (Table 2.3). The list reported in the table has been synthesized for the sake of brevity. Further details can be found in the cited Directives and regulations. Eventually, the substances to be considered will be only those that are stored or manipulated in sufficient amount to produce damage, i.e. the amount reported in Table 2.3.

Table 2.2 List of chemicals, expressed by the hazard classification of CLP (EC 1272/2008) and the corresponding amount as given in the Seveso Directive (2002).

Hazard categories	Amount (tons)
Section 'H' – HEALTH HAZARDS	
H1 ACUTE TOXIC Category 1, all exposure routes	5
H2 ACUTE TOXIC Category 2, all exposure routes; Category 3, inhalation exposure route	50
H3 STOT SPECIFIC TARGET ORGAN TOXICITY – SINGLE EXPOSURE STOT SE Category 1	50
Section 'P' – PHYSICAL HAZARDS	
P1a EXPLOSIVES, Unstable explosives or Explosives, Division 1.1, 1.2, 1.3, 1.5 or 1.6, or Substances or mixtures having explosive properties according to method A.14 of Regulation (EC) No 440/2008 and do not belong to the hazard classes Organic peroxides or Self-reactive substances and mixtures	10
P1b EXPLOSIVES, Explosives, Division 1.4	50
P2 FLAMMABLE GASES Flammable gases, Category 1 or 2	10
P3a FLAMMABLE AEROSOLS, Flammable aerosols Category 1 or 2, containing flammable gases Category 1 or 2 or flammable liquids Category 1	150
P3b FLAMMABLE AEROSOLS, 'Flammable' aerosols Category 1 or 2, not containing flammable gases, Category 1 or 2 nor flammable liquids category 1)	5 000
P4 OXIDISING GASES Oxidising gases, Category 1	50
P5a FLAMMABLE LIQUIDS, Flammable liquids, Category 1, or Flammable liquids Category 2 or 3 maintained at a temperature above their boiling point, or Other liquids with a flash point ≤ 60 °C, maintained at a temperature above their boiling point	10
P5b FLAMMABLE LIQUIDS, Flammable liquids Category 2 or 3 where particular processing conditions, such as high pressure or high temperature, may create major-accident hazards, or Other liquids with a flash point ≤ 60 °C where particular processing conditions, such as high pressure or high temperature, may create major-accident hazards	50
P5c FLAMMABLE LIQUIDS, Flammable liquids, Categories 2 or 3 not covered by P5a and P5b	5 000
P6a SELF-REACTIVE SUBSTANCES AND MIXTURES and ORGANIC PEROXIDES, Self-reactive substances and mixtures, Type A or B or organic peroxides, Type A or B	10
P6b SELF-REACTIVE SUBSTANCES AND MIXTURES and ORGANIC PEROXIDES, Self-reactive substances and mixtures, Type C, D, E or F or organic peroxides, Type C, D, E, or F	50
P7 PYROPHORIC LIQUIDS AND SOLIDS Pyrophoric liquids, Category 1 Pyrophoric solids, Category 1	50
P8 OXIDISING LIQUIDS AND SOLIDS Oxidising Liquids, Category 1, 2 or 3, or Oxidising Solids, Category 1, 2 or 3	50
Section 'E' – ENVIRONMENTAL HAZARDS	
E1 Hazardous to the Aquatic Environment in Category Acute 1 or Chronic 1	100
E2 Hazardous to the Aquatic Environment in Category Chronic 2	200
Section 'O' – OTHER HAZARDS	
O1 Substances or mixtures with hazard statement EUH014	100
O2 Substances and mixtures which in contact with water emit flammable gases, Category 1	100
O3 Substances or mixtures with hazard statement EUH029	50

2.4 VULNERABILITY MODEL

In the framework of a performance-based analysis related to natural events, each damage should be classified according to fixed levels of damage, generally called Damage States. HAZUS (HAZUS-MH MR4, 2009), e.g., provides the Damage States for many types of structures, components and groups of structures. Each Damage State DS is related to synthetic and representative intensity measures of the observed natural hazard.

In the case of NaTech analysis, different limit states related to the loss of containment from the given equipment rather than structural vulnerability, need to be developed. These limit states are often defined as Risk State RS in the existing literature (Campedel et al., 2008; Salzano et al., 2009).

Both DS and RS states are sketched and defined in the following sections. For each damage or risk state, a vulnerability function has been defined based on earthquake or tsunami intensity parameters. These functions have been retrieved from scientific literature or, if not existing, directly developed within the STREST project. The vulnerability functions will be adopted in existing tools for the quantitative risk assessment and for the scope of CI-A1 task.

When equipment is designed, any good engineering practice takes into account the possible impact of natural events like snow, wind, or earthquake. Some requirements for structural response of equipment when subjected to earthquakes are e.g. compulsory in early design phases.

With reference to the specific case of construction of atmospheric storage tanks, for instance, API 650 (2015) takes into account two response modes, for either anchored or unanchored tanks, with respect to earthquakes: a high frequency response to lateral ground motion of the liquid contents that moves in unison with shell, and a relatively low-frequency response of the liquid tank content that moves in the fundamental sloshing mode. The two modes lead to an overturning action of the tank.

Quite clearly, structural engineers can use more complex methodologies as Finite Element Analysis (see e.g. Eurocode 8 (EN 1998-1, 2003)). These tools are technically and economically sustainable only when a single case is considered or when designing new equipment with important impacts on economy, but they become hard to be adopted when performing risk analysis of large installations or for industrial areas (parks), with many equipment items to be analysed.

To this regard, it is worth noting that the cited structural design codes or more simplified methodologies often do not take into account active or passive prevention and mitigation systems and are always addressed to the structural integrity (that is, to avoid the collapse of the structure) of the item, hence they do not take into account the integrity of connections or of piping. Indeed, the main aim of early phase design is typically the loss of serviceability and economic issues for system recovery, whereas few concerns are related to NaTech accidental scenarios, which may possibly involve the population and environment located in the surrounding of industrial installation. Eventually, these methodologies are not applicable to quantitative risk assessment of large industrial installations and the use of simplified empirical equipment vulnerability models based on observational data is necessary. Besides, the number of test cases to develop from the natural event to the possible scenarios (fire, explosion, dispersion of toxic substances), combined with the elevated

number of equipment does not allow the use of even simple numerical lumped parameter models or distributed parameter models except with large economic and time efforts.

In the development of such tools, the damage classification proposed by HAZUS guideline (HAZUS-MH MR4, 2009) might be adopted and extended to any natural event in the framework of NaTech risk assessment. More specifically, limit states for structural damage (damage state, DS) may be defined for structural damages, though with specific reference to industrial purposes. According to HAZUS damage classification (1997), a slight damages to structures have been defined as DS2, a moderate damages as DS3, an extensive damages as DS4 and the total collapse of structure as DS5. The term DS1 refers to the absence of damage.

As suggested in previous section, the framework of industrial risk assessment suggests however the adoption of an even more simplified approach based on a limited number of discrete damage states (DS). In the present document and with the aim of vulnerability ranking, a lower number of damage states need to identified as a possible consequence for any equipment loaded by a seismic event (Campedel et al., 2008; Salzano et al., 2009). The definition of DS will be given for each specific equipment in the following.

Furthermore, for the aims of QRA, "Risk States" (RS) have to be defined in order to obtain a measure of the quantity and rate of hazardous substances released from containment systems, following the structural damage of industrial equipment (Salzano et al., 2003a; Salzano & Cozzani, 2007; Campedel et al., 2008) due to the impact vector characterizing the natural event.

As in the case of DS, also RS may vary between the total absence of release and the moderate release of hazardous substance, up to the extensive loss of containment. Quite clearly, the significance of RS may depend strongly on the equipment and substance type. In the case of pressurized equipment containing toxic substances, for instance, the consequences of both moderate and extensive release may be quite similar, because – due to pressurisation - even relatively small failures of shell structure may produce large damage and similar loss of containment (which depends only on loss section, due to choking flow).

Quite clearly, for any RS value a correspondent accident scenario (fire, explosion, and toxic dispersion) may be associated. This passage is not described in this deliverable and is part of the more general application of Quantitative Risk Assessment.

The damage state DS and the risk state RS can be correlated by simple analysis, which depends on the specific equipment type. Furthermore, starting from the definitions, industrial equipment vulnerability may be defined by correlating the intensity of the impact vector for the specific natural event to the probability of a given limit state (RS), for each category of equipment, by means of "fragility" curves:

$$P[RS \geq RS_i | IM] = \Phi \left[\frac{\ln(IM) - \mu}{\beta} \right] \quad (2.1)$$

where Φ is complementary cumulative normal distribution function, μ and β are lognormal mean and standard deviation values, and IM is the intensity measure i.e. the specific value of severity parameter that characterizes the natural event.

Eventually, for the generic natural event, given the equipment category (e.g. atmospheric or pressurized), we can define a NaTech vulnerability function P for each RS state as:

$$P[RS \geq RS_i] = \int_{IM} P[RS \geq RS_i | IM] \cdot h(IM) dIM \quad (2.2)$$

In other terms, the marginal Risk State probability of any equipment conditional to the occurrence of event may be assessed by considering the corresponding hazard h of the natural event. The annual rate of RS exceedance is then computed by using the annual rate of occurrence.

Cost/benefit analysis and time effectiveness lead always to the introduction of strong simplifications in the analysis in order to obtain suitable tools for risk assessment. An even more simplified approach may be required when vulnerability ranking is needed.

Threshold values for the natural intensity $IM_{nat,thresh}$ may be useful, for any Risk State defined above, in order to produce a univocal value of the natural hazard severity for the sake of prioritisation of different equipment and process systems. To this aim, the use of probit analysis is normally adopted for their mathematical definition. Details of the procedure for probit analysis are reported elsewhere (Finney, 1971). What needs to be noted is that the probability distribution function may be linearized by means of a simple integration, based on the following expression (Salzano et al., 2003a; Salzano & Cozzani, 2007; Campedel et al., 2008):

$$Y_{equipment,RS} = k_{1,equipment,RS} + k_{2,equipment,RS} \ln(IM) \quad (2.3)$$

where k_{1j} and k_{2j} are the intercept and the angular coefficient of the derived probit-function.

A classification of the event frequency may be defined by a risk matrix for the probability of occurrence based on P values. The next Table 2.3 reports a classification based in the approach introduced by the Health & Safety Executive in UK (HSE, 2005) for technological hazard.

The general mathematical methodology here presented can be applied as a vulnerability acceptance methodology if threshold values for vulnerability are given. The methodology can be easily included in the general risk assessment procedure.

In the following, the detailed analysis of vulnerability and of vulnerability classification is reported for earthquakes and tsunamis.

Table 2.3 Risk matrix for technological hazard as defined by HSE in UK (HSE, 2005).

Event probability	Hazard	Year ⁻¹
Frequent event	Very High	$> 10^{-1}$
Occasional event	High	$10^{-1} - 10^{-2}$
Un-frequent event	Moderate	$10^{-2} - 10^{-3}$
Unlikely event	Low	$10^{-3} - 10^{-4}$
Rare event	Very Low	$< 10^{-4}$

2.4.1 Technological hazard with respect to earthquake

The application of the general procedure for NaTech vulnerability classification requires the definition of a seismic function for any equipment item and for any risk state RS. The latter identifies the intensity and the characteristics of the loss of containment of hazardous materials due to the structural damage produced by the interaction of a seismic impact vector over the equipment, which is characterized by the PGA. The structural damages may be classified by Damage States (DS) using the definitions given in the previous section.

In this regard and with specific reference to earthquakes, it is worth mentioning that many guidelines, papers and books give structural fragility correlations for some categories of equipment with respect to the structural response related to seismic action or for the impact of other categories of natural events (API 650, 2015; EN 1998-1, 2003; EN 1998-4, 2003). However, the given correlations do not refer to the loss of containment and do not take into account all possible failure modes. On the other hand, the choice of Top Events or the definition of basic events for the Fault Tree Analysis may be based on simple technical considerations (though in part arbitrary), and on the correlation between the loss of containment and the structural damage.

In the following, fragility curve parameters and probit coefficients for atmospheric storage tanks, pressurized equipment, reactors and pumps are shown. The fragility parameters, when possible, were obtained for different filling levels and different types of equipment, starting from the analysis of post-earthquake observations, literature data and results of structural analysis of reference structures. As said above, the definition of both DS and RS fragility functions allows the definition of threshold values for the intensity of impact factors. Thus, probit analysis was used to obtain threshold values for the Peak Ground Acceleration in the case of earthquakes. The threshold values obtained are reported in the following for the above cited equipment categories.

Atmospheric storage tanks

Failure modes reflect the specific aspects of the seismic demand on the structure and depend upon the type of interface at the tank base. The presence of mechanical devices is used to ensure an effective connection between the base plate and the foundation (unanchored or anchored). When unanchored tanks are of concern, the friction at the base is able to ensure the needed stability of the structure under environmental actions, i.e. wind, but can be ineffective when strong ground motions take place, thus generating large relative displacements. Indeed, tank sliding reduces the maximum acceleration suffered by the equipment. However, a relatively small frictional factor may produce large relative displacements, hence large deformations and even the failure of piping and connections can occur. In addition, another large-displacement mechanism is the partial uplift of the base plate. This phenomenon reduces the hydrodynamic forces in the tank, but can increase significantly the axial compressive stress in the tank wall and the possibility that a characteristic buckling of the wall (Elephant Foot Buckling – EFB) occurs. EFB is normally associated with large diameter tanks with height to radius (H/R) ratios in the range of 2 to 3, whereas another common buckling mode, known as diamond shape buckling (DSB), is associated with taller tanks, i.e. H/R ratios of about 4. While EFB is associated with an elastic-plastic state of stress, the DSB is a purely elastic buckling. Other possible structural damages are foundation collapse due to soil liquefaction, splitting and leakage associated only with bolted and riveted tanks. Liquid sloshing during earthquake action produces several damages by fluid–structure interaction phenomena and can result as the main cause of equipment damage or collapse for full or nearly full tanks.

Historical analysis and assessment of seismic damages of storage tanks have shown that only full (or near full) tanks experienced catastrophic failures. Low H/R tanks only suffered cracks in conical roof connection, or damage by floating panel sinking.

As cited above, very common shell damage is the EFB. For unanchored tanks and $H/R < 0.8$, EFB is typically not experienced but the base plate or the shell connection can fail causing spillage. A full stress analysis is certainly the more accurate way to design and to evaluate the risk of steel tanks under earthquake loads. For base constrained and rigid tanks (anchored), a complete seismic analysis requires the solution of Laplace's equation for the motion of the contained liquid, in order to obtain the total pressure history on the tank shell during earthquakes (see Eurocode 8 (EN 1998-4, 2003)). When flexible tanks are considered, a structural deformation term must also be added to take account of the “impulsive” and “convective” contributions. Actually, the quantitative assessment of risk within a complex industrial installation requires the analysis of a large number of components. Hence, in the light of simplification, statistical and empirical tools derived from post-accident analysis are useful to define easy to manage and general vulnerability functions.

Table 2.4 reports the structural failure modes for the specific case of atmospheric steel storage tanks, and the relevance of hazardous liquid release in the risk state RS3 (instantaneous release of the complete inventory), RS2 (continuous release of the complete inventory in ten minutes), and RS1 (continuous release from a hole having an equivalent diameter of 10mm) as obtained by (Campedel et al., 2008).

Table 2.4 Earthquake failure modes and release intensity (RS3: large release; RS2: small release; RS1: un-relevant or very small release) for atmospheric storage tank.

Failure mode	Definition	Release
Elephant Foot Buckling	Large axial compressive stresses due to beamlike bending of the tank wall	RS3
Base uplifting	Overturning moment may be cause a partial uplift of base plate; this vertical displacement can cause the failure of tank wall and/or the failure of piping connection.	RS3
Sloshing	Roof or Top damage due to liquid movement	RS1
Sliding	For un-anchored tank only: the horizontal relative displacement between tank and base can cause the failure of I/O piping	RS2
Collapse (Liquefaction)	Rapid release of content due to total collapse of structure for the ground liquefaction due to earthquake	RS3

The data in Table 2.4 can be related to the probability of RS1-RS3 classes, which are related directly to structural vulnerability models, and may be associated with the occurrence of fires, explosions, toxic dispersion, as included in existing risk analysis software (Campedel et al., 2008). On the other hand, the defined failure modes may be the starting point for numerical analysis of equipment structural failure when subjected to seismic waves with a given PGA. It is however worth saying that detailed structural analysis is time-consuming and the level of detail may exceed that required in a QRA framework, even if the development of improved numerical analysis techniques, in the near future, may refine the results obtained by simplified methodologies.

Table 2.5 and Table 2.6 report the coefficients μ and β of the cumulative log-normal distribution for the probability of occurrence of RS limit states for anchored and unanchored storage tank respectively, and the correspondent coefficients k_1 and k_2 for the probit function, with respect to PGA expressed in terms of g (acceleration of gravity) as defined by Salzano et al. (2003a), based on observation of several earthquakes that occurred worldwide.

Probit functions are essential for the definition of threshold values for the PGA for each limit state (PGA_k), also reported in the Tables. The PGA_k value corresponds to the PGA value below which the probability of occurrence of any Risk State is negligible. These values are of utmost importance in the development of early warning systems that will be discussed in the following.

Table 2.5 Seismic probit coefficients and threshold values (PGA_k) for anchored atmospheric steel tanks.

Risk State (RS)	μ (g)	β	k_1	k_2	PGA_k (g)
≥ 2	0.30	0.60	7.01	1.67	0.074
3	1.25	0.65	4.66	1.54	0.275

Table 2.6 Seismic probit coefficients and threshold values (PGA_k) for unanchored atmospheric steel tanks.

Risk State (RS)	μ (g)	β	k_1	k_2	PGA_k (g)
≥ 2	0.15	0.70	7.71	1.43	0.029
3	0.68	0.75	5.51	1.34	0.118

A first comparison of the given threshold values is possible by considering the values obtained by Talaslidis et al. (2004) who carried out a numerical analysis for an atmospheric storage tank, 50% filling level, with a volume of about 37000 m³. Similar to the present approach, five limit states for the structural damage were defined and fragility curves were produced, one for each limit state, although no reference was made to the loss of containment. The basic failure modes considered by Talaslidis and co-workers is material yielding, whereas local buckling (EFB) and other failure modes, such as sliding, sloshing and uplifting were neglected. Consequently, the values obtained as threshold PGAs are higher than those reported in previous Tables, which consider all possible failure modes.

The results reported in Table 2.5 and Table 2.6 can be used as the starting point for the prediction of accident scenarios like fires (pool fire, flash fire, and tank fire), explosions (in the case of formation of a large vapour cloud) or, when toxic vapours are formed, for atmospheric dispersion analysis.

Pressurized horizontal tanks, reactors and pumps

Although a large amount of data and analyses are reported in the literature for atmospheric storage tank, little information is found for pressurized equipment, reactor vessels and pumps, which may be useful for risk assessment. Results reported in Table 2.7, Table 2.8 and Table 2.9 were derived from the data obtained by Seligson et al. (1996). It is worth noting that in the case of pressurized equipment, DS1 corresponds to slight movement of tank support or low probability of failure of some connecting pipe, with negligible release of content (RS1), whereas DS2 corresponds to failure of most connection pipes and/or tank support system, with high likelihood of release of tank content from pipes (RS2). Finally, DS3 and RS3 correspond to total failure of tank (with buckling), with an instantaneous release of

content from the storage tank and pipelines. It is also relevant to note that in the case of pressurized flammable or toxic gases, small failures in the tank shell would lead to large releases of pressurised gas and to catastrophic accident scenarios.

Table 2.7 Seismic probit coefficients and threshold values (PGA_k) for pressurized horizontal steel storage tanks.

Risk State (RS)	μ (g)	β	k_1	k_2	PGA _k (g)
≥ RS1	0.83	0.99	5.36	1.01	0.069
≥ RS2	1.85	0.85	4.50	1.12	0.196
RS3	4.91	0.84	3.39	1.12	0.526

Table 2.8 Seismic probit coefficients and threshold values (PGA_k) for pressurized reactors.

Risk State (RS)	μ (g)	β	k_1	k_2	PGA _k (g)
≥ RS1	0.79	0.92	5.46	1.10	0.080
≥ RS2	2.02	0.78	4.36	1.22	0.249
RS3	6.35	0.95	3.30	0.99	0.526

Table 2.9 Seismic probit coefficients and threshold values (PGA_k) for pumps.

Risk State (RS)	μ (g)	β	k_1	k_2	PGA _k (g)
RS2	0.81	1.29	5.31	0.77	0.032
RS3	2.44	1.00	4.30	1.00	0.195

The reported threshold values can be easily used in the vulnerability analysis of equipment to earthquakes, given the occurrence probability of the PGA value.

Pipelines

When pipelines or underground structures are of concern, the damaging effects due to the passage of seismic waves in the soil are generally proportional to the Peak Ground Velocity (PGV), which is the peak value of the horizontal velocity time histories and which is less sensitive to the higher frequency component of the ground motion. However, for structural

applications on aboveground pipelines, the use of the PGA, which is instead the peak of the horizontal acceleration of the time history, is preferable.

Quite clearly, the PGA and PGV are only synthetic description of a seismogram and do not give a complete description of the local ground motion, in terms of frequency content and signal duration, which are also important parameters for the structural response. However, these instrumental, synthetic parameters are frequently used to relate structural damage and seismic intensity for their simplicity and clarity.

Also for the performance of pipelines, many analytical and empirical formulations are based on PGA or PGV (Tromans, 2004).

For the aims of this project, we have considered two types of pipeline: those used for gas and those for liquids, either aboveground or underground, following the work of Salzano and co-workers, which in some recent parts has been developed within this project (Lanzano et al., 2013; Lanzano et al., 2014a; Lanzano et al., 2014b; Lanzano et al., 2015).

With specific reference to effects of earthquake on pipelines, the Federal Emergency Management Agency in the U.S. gives specific indications and tools for the estimation of possible damage scenarios due to natural catastrophic events, although somehow simplified (FEMA, 2008). These indications are collected under the well-known guidelines of Hazard in US or HAZUS (HAZUS-MH MR4, 2009). In the European context, concerning the seismic behaviour of industrial systems and equipment, very few indications are given in existing codes, even if the part 4 of Eurocode 8 (EC8) (EN 1998-4, 2003) gives some general principles to ensure earthquake protection for aboveground pipelines and buried pipelines. In particular, the EC8 prescribes that for gas and liquid buried pipelines the soil/structure interaction should always be considered, whereas for aboveground pipelines, the geotechnical effects are essentially related with the loss of support of the structure and differential movements. Furthermore, the hydraulic dynamic effects are considered negligible, due to the filling level inside the pipelines, except for the case of wastewater system. Finally, the use of continuous pipelines for systems, which commonly treat flammable and pollutant material, is mandatory.

A fundamental classification of pipeline system has to first be carried out by separating transportation and distribution network. The transportation network is generally used to transfer the liquid or gas from the production place to the industrial plants or urban distribution system.

With respect to gas, the overland transportation pipelines operate generally at high pressure (> 70 bars), in order to transfer a large amount of fluid in the unit time. In the U.S., e.g. the large scale natural gas transmission system includes around 300,000 km of high-strength, steel pipelines, with diameters between 0.6 m and 0.9 m and pressures between 34 and 97 bars (Folga, 2007). This system will not be considered in this section, which is intended for single-site. However, from a structural point of view, the difference between transportation and distribution systems is essentially related to the nominal diameter of pipelines. According to HAZUS, with specific reference to the seismic vulnerability analysis of pipeline systems, two large categories can be recognized: a) $D \geq 400$ mm for high pressure transmission system; and b) $D < 400$ mm for distribution and low pressure transmission systems.

When distribution system is of concern, which is the case of this deliverable, the most common materials for pipelines are cast iron, ductile iron, steel and polymers. Cast iron has been largely adopted in the last century. This material shows high fragility and lacks ductility,

which is an important safety requirement. For these reasons, pipelines are nowadays made of ductile iron, steel and plastic material like polyvinylchloride, polyethylene (HDPE) and glass reinforced fiber polymers. Other construction materials, as concrete, are used for water and wastewater pipelines.

If seismic response is of concern, the damage patterns occurring in these structures are largely dependent on the material base properties and the joint detailing. For this reason, all the possible combinations of material and joints were divided in two significant categories, namely continuous pipelines (CP) and segmented pipeline (SP). It is worth noting that a similar approach has been already adopted in the context of HAZUS, where the pipelines are divided in brittle (SP) and ductile (CP) based on the seismic performance, in terms of pre-failure deformations.

Table 2.10 reports the main structural aspects which are essential for gas and liquid pipelines. It is worth noting that hazardous materials (toxic, flammable) must be transported only in continuous pipelines, which have high strength and large deformations before structural break and consequent fluid release.

Table 2.10 Structural aspects in the seismic behaviour of pipelines

Pipelines	Materials	Joints	Damage patterns
Continuous (CP)	Steel; Polyethylene; Polyvinylchloride; Glass Fiber Reinforced Polymer.	Butt welded; Welded Slip; Chemical weld; Mechanical Joints; Special Joints	Tension cracks; Local Buckling; Beam buckling
Segmented (SP)	Asbestos cement; Reinforced Concrete; Polyvinylchloride (PVC); Vitrified clay; Cast iron	Caulked joints; Bell end Spigot joints.	Axial Pull-out; Crushing of bell end; Crushing of Spigot Joints; Circumferential Failure; Flexural Failure.

The choice of the joints is a crucial issue in the seismic design of pipelines, particularly for those used for gas. Indeed, in order to avoid that the pipeline joints perform as weak point for the structure, they must be designed aiming at restoring the continuity of the pipeline body, in terms of strength and stiffness. To obtain this goal, the most used joints are mainly welded, according to different technology. However, in some cases, mechanical and special joints are also used (Table 2.11).

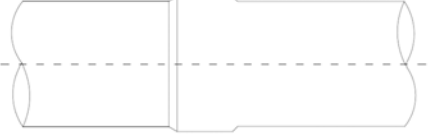
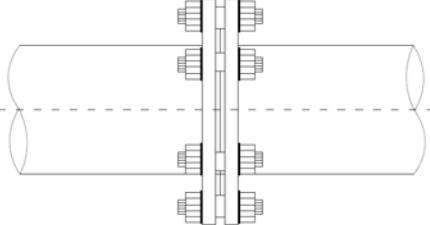
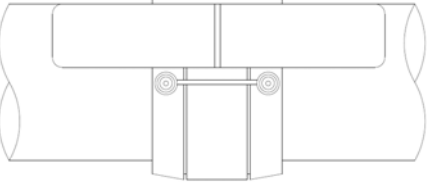

Despite these considerations on continuity restoration, significant cases of damage to welded steel joints were found in past earthquakes, especially when the breaks or leaks are related to bad quality or execution of welds. However, these latter cases are related to very old pipelines (first half of the last century), because of a lack in the protocols of quality controls.

Among the different welding technologies, three are remarkable for steel pipelines: i) oxyacetylene welding (OAW); ii) submerged arc welding (SAW); iii) high quality welding. In

the past, the most used welding belonged to the first and second categories: the SAW gives a good strength recovery compared to OAW, which suffered extensive damage in past earthquakes. O'Rourke and Deyoe (2004) observed a different performance between the spigot and socket welded joints and the butt welding, showing a better resistance recovering for the second category.

No damage data for high quality welding have been found in the available post-earthquake literature or documents. This is a clear evidence of the very good performance of this joint during seismic events.

Table 2.11 Typical joints commonly used for pipelines. D = Nominal diameter; OAW = oxyacetylene welding; SAW = submerged arc welding.

Joint	Drawings	Use/Technology
<p>Welded joints:</p> <p>a) butt welded</p> <p>b) cylindrical welded slip joint</p> <p>c) spherical welded slip joint</p>		<p>Steel pipelines (OAW or SAW):</p> <p>a) all;</p> <p>b) $D \leq 150$ mm;</p> <p>c) $D > 150$ mm.</p>
<p>Mechanical joints:</p> <p>a) slip-on welding flanges;</p> <p>b) welding neck flanges</p>		<p>Steel pipelines/HDPE:</p> <p>These joints are commonly used in buried/above-ground pipeline as regulator station, metering/reduction pressure station</p>
<p>a) electro-fusion welding</p> <p>b) coupling joints</p>		<p>HDPE pipelines:</p> <p>a) Two techniques:</p> <p>1) First involves heating and ends of the pipe to be joined against an electrically heated plate.</p> <p>2) Electro-fusion joining involves an electrically conducting implant being incorporated into special couplings.</p> <p>b) Steel couplings fixed with screws</p>
<p>Compression fittings</p>		<p>HDPE, LDPE pipelines:</p> <p>$D < 110$ mm.</p>

An important distinction is clearly between underground and aboveground pipelines. Generally, the burial depth of gas pipelines is in a range of 1-2 m. On the other hand, pipelines with very large diameter are buried deeper. For the above-ground case, the use of support is common.

Gas pipes are frequently placed under the ground level. The burying process is beneficial for two main reasons. Quite obviously, the landfill protects the pipeline from above ground damaging events, natural or human accidents. Secondly, the lateral confinement given by

the surrounding soil, which increases with depth, reduces the seismic effects. Therefore, the pipeline tends to accommodate the soil deformation and the performance of the structure is strongly related to the geotechnical effects only.

Based on experience and data collected during past earthquakes, geotechnical dynamic effects related to the pipeline damage can be divided in two categories (O'Rourke & Liu, 1999) (Fig. 2.1):

- Strong ground shaking (SGS): the effect is a deformation of the soil, which surrounds the pipeline, without breaks or ruptures in the soil depending on the earthquake intensity;
- Ground failure (GF): the surrounding soil is affected by failure phenomena caused by the earthquake as active fault movement (GF1), liquefaction (GF2) and landslides induced by the shaking (GF3). Quite clearly, these seismic failure mechanisms could appear only in specific geotechnical conditions, so that they are site dependent (i.e., for the loose sands under groundwater level for the GF2 phenomenon).

Ground shaking is the common seismic phenomenon for the design of industrial and civil systems whereas other seismic-induced phenomena may produce permanent deformation only for specific site conditions and therefore, in some cases, may be neglected.

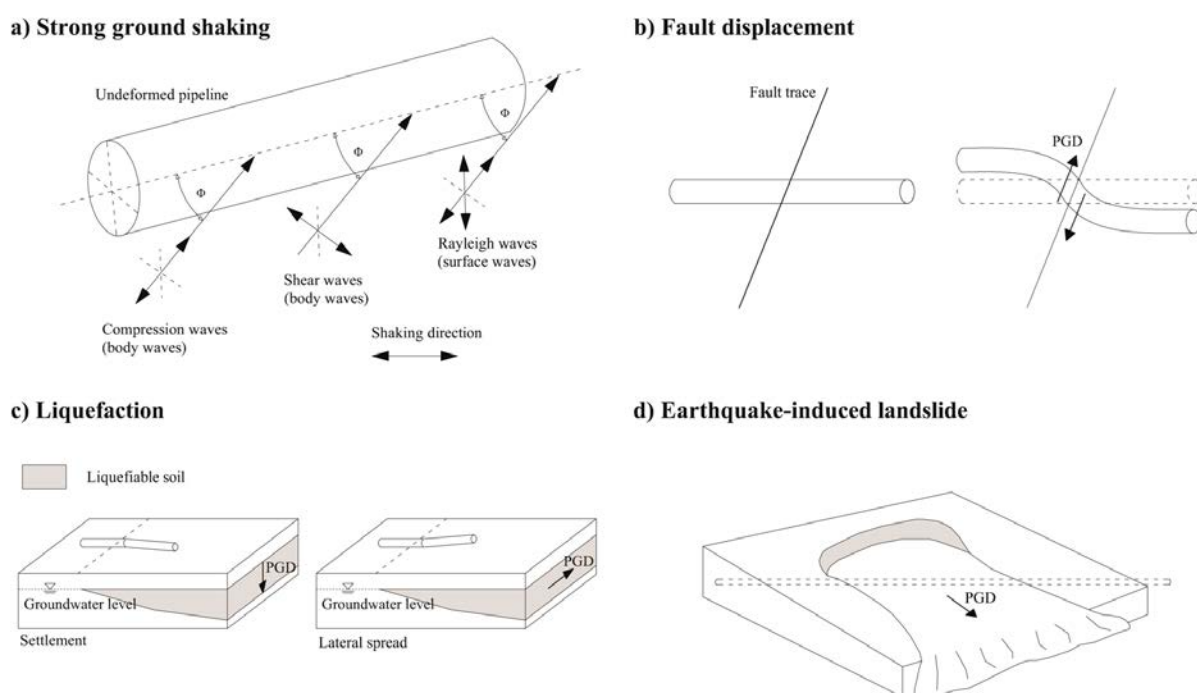


Fig. 2.1 Summary of strong ground shaking and ground failure interaction mechanisms (adapted after O'Rourke & Liu, 1999).

A review of the existing fragility curves for pipelines transporting gas and liquid is given by Tromans (2004). In that work, the most used performance indicator for the damage of pipeline due to the earthquake is clearly the repair rate (RR), which gives the numbers of repairs for a unit length of pipeline. O'Rourke and Deyoe (2004) observed that a possible limit in the calculation of RR is the reference length of pipe. Hence, they proposed a criterion to obtain the limit pipe length for a given RR, in order to select reliable data for the fragility construction.

The intensity indicators for the seismic action, instead, are strictly dependent on the geotechnical aspects related to the pipeline damage. Pineda-Porras and Najafi (2010) have discussed the most common fragility formulations for seismic damage estimation of pipelines (including water pipelines). Almost all the available formulations give however the RR as a power function of the seismic intensity measures IM:

$$RR (n^{\circ} \text{repairs} / km) = a \cdot IM^b \quad (2.4)$$

where a and b are two constants which depend on pipeline characteristics. In Table 2.12, a list of the most used fragility formulations for gas pipelines and PGV as IM are given. The table includes the information on the number of earthquakes used for the curve construction and the different criteria performed to account for the different structural, geotechnical, geological and seismological aspects.

The repair rate RR cannot be considered as the only objective parameter, also for its dependence on the reference length of pipeline, which is not uniform among the different formulations. Furthermore, these empirical formulations are mainly based on few data, with the exception of ALA (2001). Finally, the RR value does not refer to the probability of structural damage and accident scenarios, which may be triggered by the earthquake action. In such perspective, the investigation developed in this work is aimed at developing seismic fragility curves able to fit specific requirements of industrial risk analysis methodologies, following the general methodology for the seismic damage estimation given for aboveground tanks (Salzano et al., 2003a; Fabbrocino et al., 2005). Similar procedures for the evaluation of seismic vulnerability of the geotechnical structures based on performance criteria were however also adopted by the PEER (Pacific Earthquake Engineering Research) and discussed by Kramer et al. (2009).

The methodology is essentially based on a large collection of post-earthquake data and in the definition of significant classes for the pipeline failure based on structural Damage State (DS) and Risk State (RS) indicators.

Table 2.12 Most common empirical fragility expressions for pipelines under SGS (S: steel; CI: cast iron; WJ: welded joints; FJ: flange joints). The terms a and b are the coefficients of Eq. 2.6).

N° earthquakes	N° points	a (10 ⁻⁴)	b	Reference
6	11	0.3 (ductile)	2.25	HAZUS-MH MR4, 2009
7	~19	0.829 (S, WJ, small D, unknown soil) 1.330 (S, WJ, small D, corrosive soil) 0.497 (S, WJ, small D, non-corrosive) 0.249 (S, WJ, large D, all soils)	1.98	Eidinger, 1998
18	81	0.995 (S, WJ, small D, unknown soil) 1.490 (S, WJ, small D, corrosive soil) 0.497 (S, WJ, small D, non-corrosive) 0.249 (S, WJ, large D, all soils) 2.160 (S, FJ, small D, all soils)	1.00	ALA, 2001
5	14	64.0 (Rayleigh waves, mainly CI) 3.5 (body waves, mainly CI)	0.92	O'Rourke & Deyoe, 2004

In Table 2.13, the structural damage indicators (DS) have been properly recalibrated from the simplified classification of HAZUS. They give an approximated correlation between damage patterns (breaks or leaks) and geotechnical aspects (SGS or GF): the result is that most of SGS are related to leaks and most of the GF to breaks.

The two HAZUS damage levels correspond approximately to DS1 and DS2 of Table 2.13, which are better defined in each damage point, including an initial class of negligible damage for pipeline working.

Based on the complete database and on the observed behaviour of pipelines, five possible classes of fragility curves have been then recognized: a) buried CP under SGS; b) buried CP under GF; c) buried SP under SGS; d) buried SP under GF; e) aboveground pipelines (AP).

Table 2.13 Structural Damage States (DS) for steel pipelines.

States	Damage	Patterns
DS0	Slight	Investigated sections with no damage; slight pipe buckling; damage to the supports of aboveground pipelines without damage to the pipeline.
DS1	Significant	Significant pipe buckling; longitudinal and circumferential cracks; compression joint break.
DS2	Severe	Tension cracks for continuous pipelines; joint loosening in the segmented pipelines.

The Damage State refers to the type of structural damage to the pipeline. However, either Qualitative or Quantitative Risk Analysis or Land Use Planning, need other indicators. Hence, like for other type of equipment described above, Risk States (RS) were qualified on the basis of the possible negative effects on the external environment or population, i.e. on the possible harmful effects derived from the release of content from the damaged pipe (Table 2.14). Quite clearly, the indicators have been distinguished on the basis of the transported fluid. In order to correlate the structural damage to the release of containment, an equivalent diameter Φ of a crack in the pipelines has been defined.

Table 2.14 Risk States (RS) for pipelines. Φ = equivalent diameter.

States	Risk	Release of containment	
		Gas/Vapour/Liquefied Gas	Liquid
RS0	Negligible	No losses	Limited loss
RS1	Low	Very limited losses: Toxic ($\Phi < 1$ mm/m); Flammable ($\Phi < 10$ mm/m)	Limited, time-distributed loss of hazardous substance: multiple losses ($\Phi < 10$ mm/m)
RS2	High	Non-negligible losses	Large loss (e.g. entire tube surface) or multiple losses ($\Phi > 10$ mm/m)

In the table, the RS levels may be organized in order to match the corresponding damage states DS.

For gas pipelines, we have defined the following RS:

- i) RS1 was formulated in order to match DS1 class, which includes all the damage that cause the loss of a limited or time-distributed amount of gaseous fluid;
- ii) RS2 has the highest level of risk and accounts for all the damage in DS2, relative to the release of large amount of gaseous fluid in a very short time interval.

Similar risk states RS were also formulated for liquid pipelines, however with some difference:

- i) RS1 was formulated in order to match DS1 class, with limited, but time-distributed, release of content;
- ii) RS2 has the highest level of risk and accounts for the case of complete failure of pipe section.

In the following, for the RS classes, fragility and probit functions are shown for continuous pipelines under strong ground shaking (SGS), which is the most common seismic effect (O'Rourke & Liu, 1999), with respect to PGV value.

Fig. 2.2 shows the fragility curves for continuous pipelines under SGS for $RS \geq RS1$ (low risk) and $RS = RS2$ (high risk). The curves represent the probability of each possible damage, as function of PGV. They are considered strictly valid for steel pipelines with welded joints, which are commonly used for gas pipelines but can be applied for liquid pipeline also. As regards the pipeline diameters, three different classes of fragility curves were considered: all diameters, small diameters ($D < 400$ mm) and large diameters ($D \geq 400$ mm).

Table 2.15 Fragility parameters for steel pipelines, welded joint.

Diameter	Risk state	Fragility	
		μ (cm/s)	β
D	RS	μ (cm/s)	β
All	$\geq RS1$	45.22	0.39
All	$= RS2$	71.16	0.20
< 400 mm	$\geq RS1$	37.21	0.29
< 400 mm	$= RS2$	63.25	0.12
≥ 400 mm	$\geq RS1$	50.14	0.23
≥ 400 mm	$= RS2$	49.43	0.41

The results show an increase of the value of median parameter μ from $RS \geq RS1$ to $RS = RS2$, coherently with the increase of the risk state. An exception is the case of $RS = RS2$ for $D \geq 400$ mm, where the median decreases and the shape parameter β increase. This different behaviour is due to a less reliable estimation of fragility, because it was based on a limited number of data (27 samples) and of investigated earthquakes (only 2). For this reason, for the transmission pipelines, at the present stage, it is recommended to refer to the fragility curve derived for all diameters. It is however expected that further work and data can provide a more reliable definition of the fragility function for DS2 in the case of large

diameters ($D \geq 400$ mm). Accordingly, in the next section, the results referring to large diameters and $RS = RS2$ are not provided for transmission pipelines.

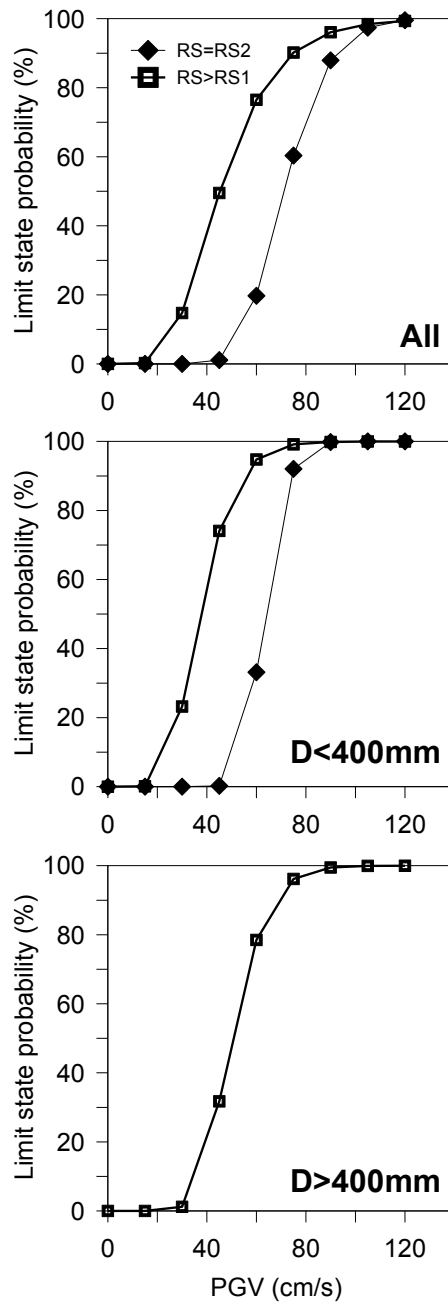


Fig. 2.2 Fragility curves for steel pipelines under SGS for a) all dataset; b) small diameter ($D < 400$ mm) and c) large diameter pipelines ($D \geq 400$ mm).

Similar tools were retrieved also for segmented pipelines, which are mainly adopted for the transportation of non-hazardous liquids, including water and wastewater (Table 2.16). Because the limited amount of samples, the fragility parameters have been obtained only for $RS \geq RS1$.

Table 2.16 Fragility coefficients for liquid pipelines under SGS. IM = PGV expressed in cm/s.

Diameter	Risk state	Fragility	
		μ (cm/s)	β
All	\geq RS1	21.80	0.26

The seismic vulnerability of pipelines has been estimated by using the classical probit analysis as defined in previous sections. The probit functions are shown in Fig. 2.3. The calculated probit coefficients k_1 e k_2 , together with the threshold values of the PGV are reported in Table 2.16.

In the table, the threshold values IM_0 were obtained through a “cut-off” of the probit curve with the abscissa, which is the PGV providing a value of the probit corresponding to the zero probability. The values have to be considered as intrinsic strength parameters for the pipeline structural performance and for the soil/structure interaction during the seismic events. The physical meaning of IM_0 is defined as the limit value of the seismic parameter, above which a certain level of damage should be considered in the risk analyses of the pipeline network.

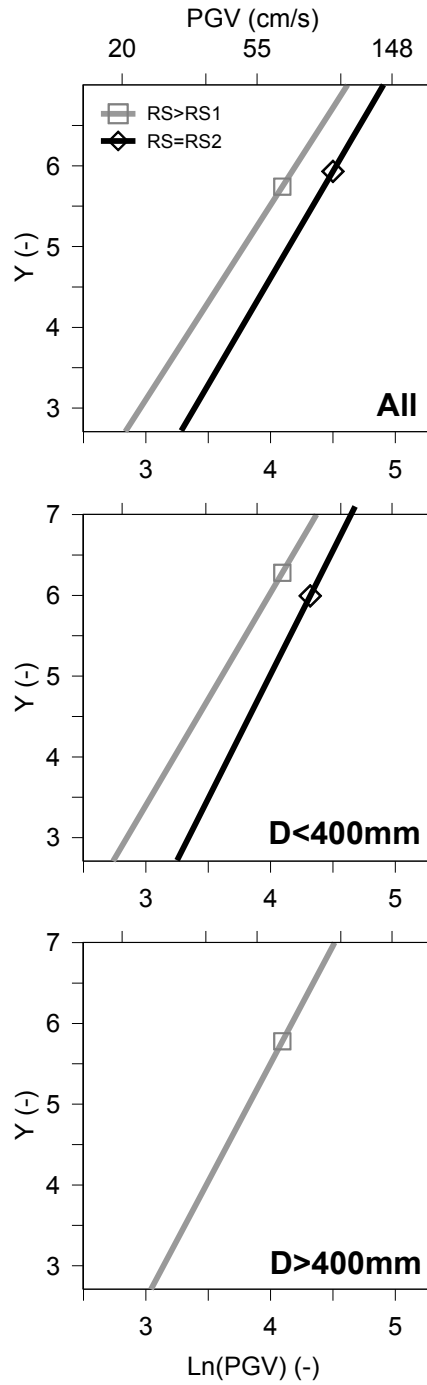


Fig. 2.3 Probit curves for steel pipelines under SGS for a) All dataset; b) small diameter ($D < 400 \text{ mm}$) and c) large diameter pipelines ($D \geq 400 \text{ mm}$).

Table 2.16 Probit coefficients and threshold values for steel pipelines, welded joint.

Diameter	Risk state RS	Probit		Threshold PGV (IM ₀)
		k ₁	k ₂	(cm/s)
All	≥ RS1	-4.12	2.41	17.05
All	=RS2	-5.95	2.64	26.58
D<400 mm	≥ RS1	-4.49	2.63	15.45
D<400 mm	=RS2	-7.26	3.07	25.72
D≥400 mm	≥ RS1	-6.16	2.92	20.95

The difference in the threshold PGV values for RS ≥ RS1 and RS2 is about 10 cm/s both for “All” and D < 400mm classes. The threshold values for all diameters are coherently averaged between small and large diameter; the corresponding PGV increase is about 5 cm/s.

Analogously, Table 2.18 gives the probit coefficients for liquid pipelines.

Table 2.17 Probit coefficients and threshold values for pipelines for liquid transportation.

Diameter	Risk state RS	Probit		Threshold PGV (IM ₀)
		k ₁	k ₂	(cm/s)
All	≥ RS1	-0.36	1.79	5.50

The threshold value for SP under SGS is quite low (5.5 cm/s) compared to corresponding value of CP (17 cm/s). In this case, the difference between the two risk threshold levels is about 10 cm/s.

2.4.2 Technological hazard with respect to tsunami

The definition of tsunami vulnerability functions has been addressed by considering the three main components of tsunami: wave speed (for the impact), wave height (for the surge) and debris. The existing methodologies for FEMA (2008) and those obtained for flooding fragilities have been considered in the development.

Starting from the assumption that the event phenomenology is practically identical, the existing fragilities of industrial components subjected to flood have been adapted for the case of tsunami hazard.

Analytical procedures developed to estimate the vulnerability of atmospheric vertical tanks (Landucci et al., 2012) and pressurized horizontal tanks to tsunami waves (Landucci et al., 2014) were then adopted. These components were already identified as the most vulnerable to flood hazard (Cozzani et al., 2010), not only because of their structural properties and the response to the flood loadings, but also due to the severe consequences related to a possible damage, in terms of release of hazardous content.

Structural damage from tsunamis can be attributed to:

- a) direct hydrostatic and hydrodynamic forces from water inundation;
- b) impact forces from water-borne debris;
- c) fire spread by floating debris and combustible liquids;
- d) scour and slope/foundation failure; and
- e) wind forces induced by wave motion.

Few data were available in the literature concerning the damage to structures due to tsunami actions, especially if compared to purely seismic data. This is probably due to two reasons: the relative low occurrence of tsunami compared to earthquakes; the very recent (basically from 2004 event) practice of analysing and collecting these specific damage data. As a consequence, observational models are difficult to implement and modelling is still necessary.

The structural components for which the tsunami vulnerability functions have been defined, in the framework of NaTech risk analyses, are:

- Atmospheric vertical tanks;
- Horizontal pressurized tanks;
- Sphere
- Pipeline connection to tankers.

The first two equipment types have been analysed in this project. Future development will be devoted to spheres and pipelines, which may however assimilate to horizontal pressurised tanks as a first approximation and conservatively.

Atmospheric vertical storage tank

Atmospheric cylindrical vessels represent the tank category most frequently involved in natural events leading to loss of containment, due to the low structural resistance (Cozzani et al., 2010).

Following the similarity with the flooding impact, the present analysis is devoted to the assessment of the vulnerability of atmospheric vertical vessels to tsunami wave due to the pressure associated to both water wave speed (v_w) and height (h_w). To this aim, a mechanical model has been developed, based on the model developed by Landucci et al. (2012) for flooding. Hence, storage tanks consisting of vertical cylindrical vessels for liquid storage operating at atmospheric pressure, with a conical roof, anchored flat bottom directly fixed to the ground, has been considered. The design by API 650 (2015), a standard used worldwide for the construction of this category of storage tanks, at least in the oil and gas industry, has been assumed for reference (Fig. 2.4).

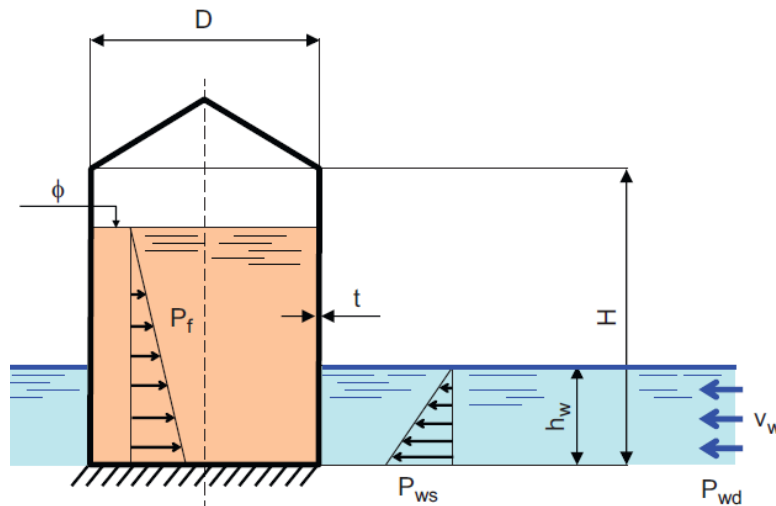


Fig. 2.4 Schematic representation of atmospheric cone roof storage tank analysed in this project (API 650, 2015).

Fig. 2.5 schematizes the forces acting on the vessels when impacted by a tsunami wave. The external load present on the tank shell, namely P_w , is obtained as the sum of a “static” pressure component and a “dynamic” pressure component

$$P_w = P_{ws} + P_{wd} \quad (2.5)$$

The static pressure component P_{ws} is due to the hydrostatic load of the floodwater and its maximum value may be expressed as it follows:

$$P_{ws} = \rho_w g h_w \quad (2.6)$$

where g is the gravity constant (9.81 m s^{-2}) and ρ_w is the density of the tsunami water. The second pressure component P_{wd} is due to the drag force associated to the kinetic energy of the wave, and may be expressed as:

$$P_{wd} = \frac{1}{2} \rho_w k_w v_w^2 \quad (2.7)$$

where k_w is the hydrodynamic coefficient (Tilton, 1999; Gudmestad & Moe, 1996). For the sake of simplicity, a constant temperature of 293 K and an atmospheric pressure of 1.01 bar were assumed in the present study, thus considering constant the fluid properties in the above relations.

The internal pressure of the tank, P_f , related to the hydrostatic pressure of the internal liquid, has an important role in the evaluation of the resistance of the tank to the external pressure. The maximum P_f value, at the bottom of the vessel, may be expressed as follows:

$$P_f = \rho_f g H \Phi \quad (2.8)$$

where ρ_f is the density of the inner fluid, H is the height of the tank and Φ is its filling level. Therefore, the net pressure P_{net} on the vessel shell may be derived from a simple force balance

$$P_{net} = P_{ws} + P_{wd} - P_f \quad (2.9)$$

The failure of this type of vessels, when undergoing an external pressure on the shell, is mostly due to buckling. This phenomenon, described in the literature by (Timoshenko & Gere, 1961), may occur if the net pressure, P_{net} , affecting the vessel outer shell, reaches a critical value, indicated in the following as P_{cr} (critical pressure). P_{cr} depends on the vessel geometry and on the construction material, and is independent from the loading conditions. P_{cr} may be calculated by the following correlation:

$$P_{cr} = K_1 C + K_2 \quad (2.10)$$

where C is the tank capacity in m^3 and K_1 and K_2 are two constants whose values are -0.199 and 6950 respectively.

Eventually, the following condition leads to failure for instability:

$$P_{net} \geq P_{cr} \tag{2.11}$$

The failure model may be used to evaluate the resistance of vessels undergoing different tsunami conditions (represented by different values of v_w and h_w).

Table 2.16 reports the values of the physical parameters used in our study.

Table 2.18 The values of the physical parameters used in this study. ρ_w = density of water, ρ_f = density of the liquid inside the tank (gasoline), Φ = filling level of the tank; k_w = tsunami hydrodynamic coefficient.

ρ_w	k_w	ρ_f	Φ
(kg/m ³)	(-)	(kg/m ³)	(-)
1000	1.8	750	0.8

It is worth to remark that the model may be applied both to fixed and floating roof tanks, since an infinite rigidity is assumed on the top of the cylindrical shell. This is justified either by the presence of the top ring in the case of floating roof tanks, or by the weight of the roof itself for the other type of tanks. However, in the case of floating roof tanks the slight increase in the inner pressure due to the weight of the roof on the upper liquid surface is neglected in the model, thus obtaining conservative results.

The following table reports the set of tank as API 650 (2015) adopted for the analysis reported in this project.

Table 2.19 Design criteria and key parameters derived from API 650 (2015) used to define tank geometry in the present study

Item	Value	Notes
D, m	3 ÷ 66	Typical diameter range among O&G tank farms and storage facilities
h_b , m	1.8	Standard height of the board which constitutes the vessel height
n_b	2 ÷ 10	The number of layers boards depends on the tank diameter
H, m	$n_b \times h_b$	Tank height
t_{min} , mm	5 ($D < 15$ m); 6 ($15 \text{ m} \leq D < 36$ m); 8 ($36 \leq D \leq 60$ m); 10 ($D > 60$ m)	Minimum thickness is a function of the tank diameter. Board maximum thickness is 12.5 mm for vessel with diameter lower than 60 m.

In this project, about 120 different tanks with different diameter, height and filling level were analysed. For each tank, a fragility function has been calculated by solving the equation systems reported previously and considering the absence of buckling as zero probability (whatever the value of J/m^2), the complete and certain buckling (whatever the value of J/m^2) and reconstructing the probability as a linear function between the two extreme points for the definition of 50% probability.

Some of the obtained fragility curves obtained by solving the model reported above are shown in Fig. 2.5 and Fig. 2.6. In general, we can affirm that no clear functional indications are given if referring to diameter or height. On the contrary, fragility is clearly representative if considering as the main intensity parameter the energy flux in J/m^2 , which is equivalent to $\rho_w h_w v_w^2$ or, in other terms, the combination of kinetic and potential (i.e. buoyancy) energy of the water wave.

The plot in Fig. 2.5 shows the buckling probability as function of the energy flux ($= \rho_w h_w v_w^2$) produced by the impact of the tsunami wave on four different tanks. In particular we have considered two sets of tanks, with a capacity of 636 m^3 and 1030 m^3 , respectively. Quite obviously, the buckling probability increases as the energy flux increases for all the tanks. For the same storage capacity, both sets of tanks show that the higher the tank, the more resistant it is with respect to energy flux of water impact. This is essentially due to the increased hydraulic resistance.

Fig. 2.6 shows the relative increment of the fragility median with respect to the tank height for a large set of tanks with two diameter D.

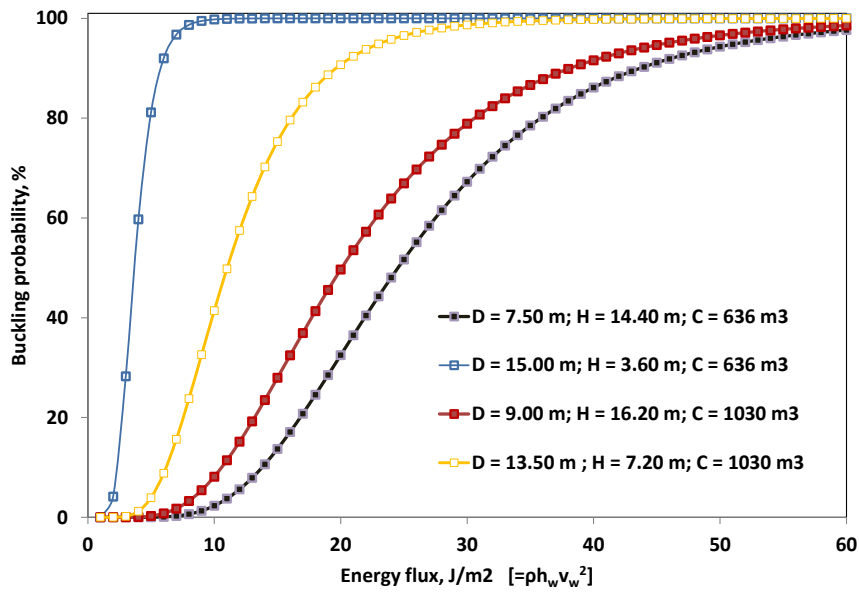


Fig. 2.5 Fragility function for some atmospheric tanks among the set analysed in this project, vs energy flux of tsunami

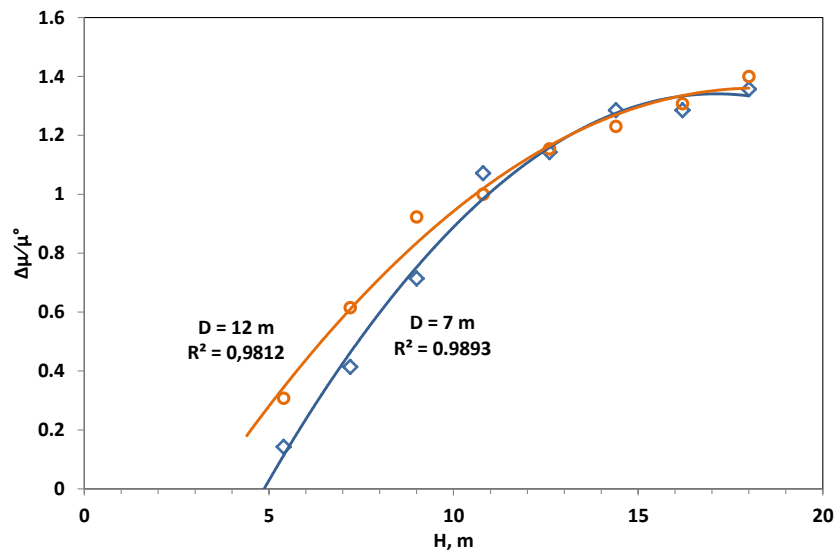


Fig. 2.6 Relative increment of fragility median vs height H of atmospheric tanks for two set of tanks with diameter D = 7 m and 12 m, respectively.

The plot shows that the resilience of the tank with respect to the height increases approximately with the same trend, whatever the diameter (and capacity). Furthermore, a plateau is observed for higher tanks.

Pressurized tanks

Specific fragility models for equipment vulnerability in the case of tsunamis are not available for pressurised storage tanks. Nevertheless, past accident data analysis showed that this type of equipment was often damaged in NaTech events triggered by floods.

The present analysis is devoted to the development of a model for the vulnerability assessment of horizontal, cylindrical, pressurised storage tanks with spherical edges, involved in tsunami events.

In order to evaluate the resistance of the equipment items considered, a mechanical model was developed based on results obtained for flooding accidents (Cozzani et al., 2010). To this aim, the references for the design and features of the tanks considered in the present study were the API standard (API 620, 2015) and the ASME Pressure Vessel Code (Sec. VIII) of the ASME Boiler and Pressure Vessel Code (ASME, 2015).

Table 2.20 The values of the physical parameters adopted for the pressurised equipment. ρ_w = density of tsunami water, ρ_f = density of the liquid inside the tank, Φ = filling level of the tank, ρ_s = density of the steel.

ρ_w	ρ_f	ρ_s	Φ
(kg/m ³)	(kg/m ³)	(kg/m ³)	(-)
1000	500	7800	0.50

The schematic representation of these vessels is shown in Fig. 2.7a. As shown in the figure, one of the vessel saddles is assumed to be fixed to the ground with a bolt connection, while the other assumed to be only laid on the ground. This configuration is frequently adopted in the process industry in order to limit the stress due to steel work thermal expansion.

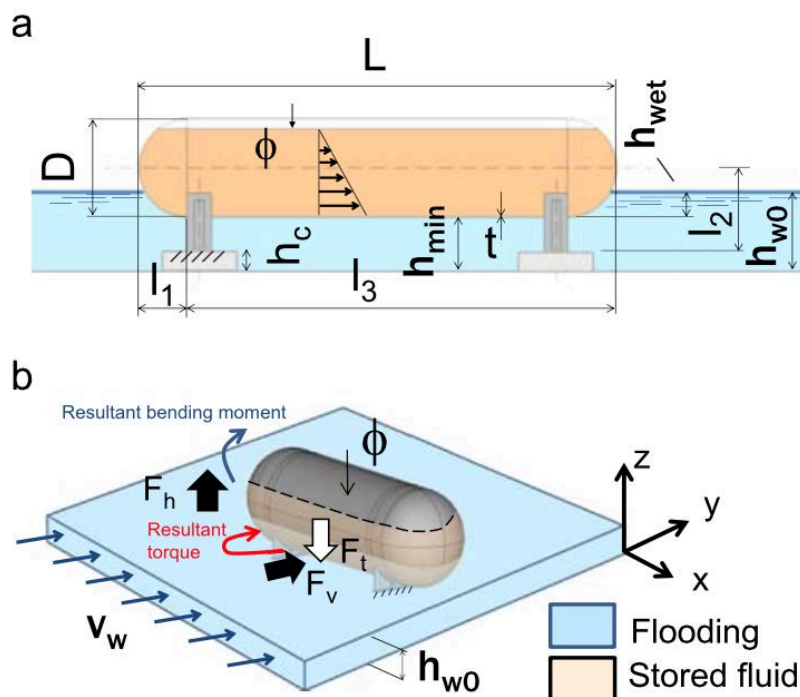


Fig. 2.7 Schematic representation of horizontal, cylindrical, pressurized vessel.

Horizontal cylindrical vessels are likely to experience different failure mechanisms with respect to vertical atmospheric vessels describe above. Indeed, the analysis of past accidents involving flooding in industrial facilities (Campedel et al., 2008; Cozzani et al., 2010) showed that failure caused by buckling was never experienced for horizontal vessels. Indeed, horizontal cylindrical vessels are mostly damaged due to displacement caused by water drag and/or to floating (Campedel et al., 2008; Cozzani et al., 2010).

Actually, horizontal cylindrical vessels, either atmospheric or pressurized, have a higher resistance to buckling with respect to vertical cylindrical storage tanks used in industrial applications, due to the higher thickness/diameter ratio (typically 2 orders of magnitude).

Eventually, the analysis of past accidents evidenced that this category of vessels is more prone to undergo failures due to displacement. In particular, the rupture of the saddle framework and of its connection to the ground was experienced in several cases.

This resulted in the displacement of the vessel, with the consequent rupture of the vessel connections and, in some cases, in the impact of the displaced vessel with adjacent vessels or structures (Gruntfest & Pollack, 1994). Therefore, the mechanical model was developed focusing on the integrity of the saddle-type support, which is the element required to fail in the case of vessel displacement caused by tsunami wave.

The schematic representation of the tsunami wave impact on a horizontal cylindrical vessel is reported in Fig. 2.7b. As shown in the figure, the vessel is subject to the hydrostatic lift force (F_h), which causes a vertical lift action, and, at the same time, to a horizontal drag force caused by the tsunami wave (F_v). Buoyancy (F_n) is the net force obtained considering the opposite actions of hydrostatic lift and of overall weight force (F_t), resulting from vessel weight and from the weight of the fluid inside the vessel:

$$F_n = F_h - F_t \quad (2.12)$$

Buoyancy may thus be expressed as a function of vessel geometry, weight and filling level:

$$F_n = \omega V_{ext} \rho_w g - g [W_t + \Phi V_{int} \rho_l + (1 - \Phi) V_{int} \rho_v] \quad (2.13)$$

where ω is the fraction of the vessel volume wetted by water, g is the gravity constant (9.81 m s^{-2}), W_t is the “tare weight” of the tank (i.e. the mass of the empty tank in kg), ρ_l is the liquid average density, ρ_v is the average density of the vapor in the top space of the vessel, ρ_w is the density of floodwater, V_{int} and V_{ext} are the inner and outer vessel volume respectively, and ϕ is the vessel volumetric filling level defined as the fraction of liquid volume respect to the total vessel inner volume V_{int} . If the value of vessel weight, W_t , is not available, this parameter may be estimated assuming the value of steel density ρ_s :

$$W_t = \rho_s (V_{ext} - V_{int}) \quad (2.14)$$

The drag force due to the tsunami wave kinetic energy (F_v) may be calculated as follows (Tilton, 1999; Gudmestad & Moe, 1996):

$$F_v = \frac{1}{2} \rho_w k_w v_w^2 A_{ext} \quad (2.15)$$

where k_w is the hydrodynamic coefficient and A_{ext} is the projected area of the vessel external surface impacted by tsunami wave in a plane normal to water flow. In order to obtain a conservative evaluation for the drag force, the water flow is assumed to impact on the side of the vessel featured by a higher external surface. Both the buoyancy, F_n , and the drag force, F_v acting on the vessel generate a stress on the vessel support (e.g., the saddle connected to the ground).

As shown previously, the tsunami severity can be quantified by two parameters: water effective depth (h_w) and water speed (v_w). The effective depth should take into account the possible effect of protection measures, such as concrete supports higher than the ground level to which the vessels addles are fixed. Taking into account the schematization in Figure 2a, if the height of the supports (h_c) is considered, the effective tsunami wave height h_w may be then calculated as follows:

$$h_w = h_{w0} - h_c \quad (2.16)$$

where h_{w0} is the actual depth of water wave. Clearly enough h_w is equal to h_{w0} if no protections are available.

Besides, a minimum value of tsunami wave height is also introduced (namely, h_{min}), that is the minimum possible tsunami wave height affecting vessels mounted on saddles. This parameter depends on the type of vessel and may be derived as follows (see Figure 2a):

$$h_{min} = l_2 - \frac{D}{2} \quad (2.17)$$

where l_2 is the height of the saddle and h_{min} is the minimum flooding height needed to wet the surface of the horizontal vessel.

Finally, in the evaluation of vessel damage due to tsunami wave impact, a further parameter is introduced in order to estimate the height of the vessel effectively wetted by water wave,:

$$h_{wet} = h_w - h_{min} \quad (2.18)$$

This latter parameter, representing the effective water height, is particularly significant for the evaluation of vessels failure due tsunami impact.

The stored fluid has a strong impact on the failure of the vessels. An increase in the filling level and/or a higher density of the stored fluid result in an increased resistance of the vessel to the action of buoyancy. Therefore, once the storage system is defined (i.e. defining the geometry of the vessel and the substance stored) the filling level φ is the only operating parameter that affects the vessel resistance to buoyancy caused by a given set of impact conditions. A critical filling level (CFL) of a vessel may thus be defined as the minimum value of φ able to ensure the tank resistance to buoyancy caused by a flood having a given intensity.

Simplified correlations are provided in the following to allow a simplified straightforward evaluation of vessel failure probability. The correlations are based on the analysis of the CFL behaviour with respect to the water effective height (h_w) assuming a reference value, ρ_{ref} , for the density of the stored substance. The effect of water speed is not taken into account to assess the CFL, since the CFL affects significantly only the resistance to buoyancy and has a limited influence on the resistance to the action of tsunami water drag force.

A linear empirical correlation may be then used to relate the CFL to water height, given the vessel geometry and the stored fluid density:

$$CFL = Ah_w + B \quad (2.19)$$

where the parameters A and B are only a function of the vessel geometry (hence, operating pressure and volume).

The reference fluid density (ρ_{ref}) of the stored fluid has been assumed as 1000 kg m^{-3} . The extended application of the mechanical model allowed the calculation of the values of the A and B parameters as a function of the geometrical features of the vessel.

It is worth mentioning that the CFL has a maximum value related to the operating capacity of the vessels (i.e. the maximum CFL value is equal to ϕ_{max}). Thus, the following empirical correlations were obtained for the A and B parameters with respect to vessel features:

$$A = K_1 Da \quad (2.20)$$

$$B = K_2 (W_t + K_3) b \quad (2.21)$$

The values calculated for the K_1 , K_2 , K_3 , a, and b parameters are reported in Table 2.18 for each category of vessel considered.

Table 2.21 Parameters adopted for the definition of tsunami effect on pressurised equipment

P_d	K_1	K_2	K_3	K_4	K_5	K_6	a	b	c
1.00	1.331	-2.163	-288.6	9.91	-0.037	-0.399	-0.990	-0.260	-0.718
1.50	1.287	-1.144	-499.2	9.91	-0.037	-0.399	-0.952	-0.112	-0.718
2.00	1.290	-1.305	-546.0	9.91	-0.037	-0.399	-0.966	-0.109	-0.718
2.50	1.256	-6.068	-234.0	9.91	-0.037	-0.399	-0.951	-0.263	-0.718

In order to take into account the actual density of the stored fluid, the following changes may be introduced:

$$CFL = A' h_w + B' \quad (2.22)$$

The values of the A' and B' coefficients may be calculated from the A and B parameters obtained using the reference fluid density ρ_{ref} :

$$A' = \frac{\rho_{ref} A}{\rho_l - \rho_v} \quad (2.23)$$

$$B' = \frac{(\rho_{ref}B - \rho_v)}{\rho_l - \rho_v} \quad (2.24)$$

where ρ_l is the actual density of the stored liquid and ρ_v is the density of the vapor phase inside the vessel.

The approach discussed above allows the calculation of a critical filling level below which the vessel may fail due to buoyancy. In order to account also for the action of the drag force, the simplified model needs however to be extended.

Tsunami waves with high water speed, v_w , may lead to vessel failure due to drag force even in the case of limited water depth. Hence a critical water velocity, $v_{w,c}$, was defined as the v_w value able to damage a given vessel for an assigned value of wetting height (h_{wet}). As a matter of fact, in case of a tsunami wave with a small h_{wet} value, thus unable to cause damages by buoyancy, $v_{w,c}$ represents the critical flood velocity value which causes the minimum drag force value required to damage the vessel. This parameter may be derived applying the mechanical model, and simplified correlations based on h_{wet} were obtained from failure plot analysis:

$$v_{w,c} = Eh_{wet}F \quad (2.25)$$

Again, it was possible to obtain empirical correlations for the E and F parameters with respect to vessel geometry:

$$E = K_4Lc \quad (2.26)$$

$$F = K_5 \ln\left(\frac{L}{D}\right) + K_6 \quad (2.27)$$

where L is the vessel length and D is the vessel diameter and c, K_4 , K_5 , and K_6 are the parameters reported previously.

The model has been applied to about 100 tanks of different diameter, length, and design pressure. Generalisation of the results, in terms of fragility, cannot be obtained.

Figure 2.7 reports the critical value for the tank failure in terms of energy flux ($= \rho_w h_w v_w^2$), for each tank of the database analysed, with respect to the capacity of the tank itself.

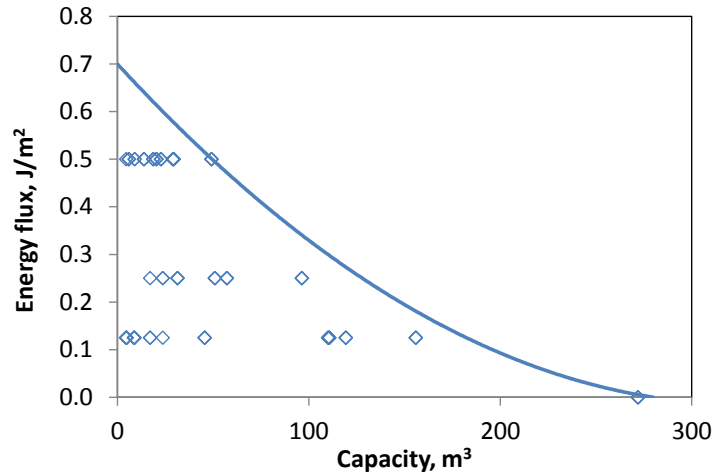


Fig. 2.8 Critical energy flux for the failure of saddle-free horizontal pressurised tank with respect to the capacity.

In the plot, it is clear that the critical energy flux decreases with the capacity (volume) of the tank, due to Archimedes' thrust.

2.4.3 Vulnerability to tsunamis debris

The vulnerability of target equipment when impacted by debris depends on process conditions (temperature, pressure), structural design (material, thickness) and layout options (mounded, buried, over-ground, racks, catch basin) but also on the intrinsic hazard of the substance (or mixture of) handled, stored or processed in the target equipment, which is dependent on hazard classification, process conditions, and physical state.

From classical analysis, it can be written:

$$\frac{\partial \Sigma}{\partial X} = \frac{\rho u_0^2}{\sigma_D} \frac{\partial \zeta}{\partial t} \quad (2.28)$$

where ρ is the target density, u_0 is the impact velocity and σ_D is the dynamic yield stress of the target material. This equation includes the essential a-dimensional term J , which in impact dynamics is called Johnson's damage number and may be adopted for evaluating the severity of the impact on a continuum loaded impulsively and impinged by the initial velocity pulse u_0 :

$$J = \frac{\rho u_0^2}{\sigma_D} \quad (2.29)$$

Actually, the damage number J can be obtained by other physics other than by the motion equation, e.g. as a measure of the order of strain imposed in the region where severe plastic

deformation occurs, or the ratio of inertia forces of the loading (numerator) to the resistance ability of the dynamically loaded material (denominator). Or, the damage number can be regarded as a measure of the fluid-like (hydrodynamic) behavior imposed in the region of severe plastic deformation during velocity impact. Also, it is comparable with the Cauchy number, which is the similarity parameter for the dynamic elastic response of material under impact loading as obtained by using $\Sigma = \sigma/E$, where E is the Young's modulus or the modulus of elasticity of the material.

The range values of Johnson's number with the corresponding regimes are defined by (Nurick & Martin, 1989) and reported in Table 2.22.

Table 2.22 Threshold values for damage for Johnson's damage number J (Nurick & Martin, 1989).

J	Regime	Probability of failure
$1 \cdot 10^{-3}$	Quasi-static elastic	0.0
$1 \cdot 10^{-2}$	Moderate plastic behaviour	0.1
$1 \cdot 10^{+1}$	Extensive plastic deformation	0.5

As reported in the table, Johnson's number values of 10 may be considered as the threshold value for the extensive plastic deformation and alternatively the minimum value for the failure of the target, including shells as in the case of tanks or pipelines.

Quite evidently, the Johnson equation does not take into account the shape effects of a fragment. However, a first approximation with respect to fragment mass, velocity and impact area for damage is possible and useful for the Johnson's damage number validation. Indeed, in order to take into account of annealing, the Johnson number has been modified in Corbett et al. (1996) as:

$$J = \frac{u_0^2 m_p}{\sigma_D \theta r_p^2} \quad (2.30)$$

where m_p and r_p are the projectile mass and the radius.

For the aims of QRA, we can then consider a zero probability for quasi-static elastic regime. By using a sigmoidal function, which is centred (probability = 0.5) on the J value corresponding to the extensive plastic deformation, a probit analysis can be performed (Cozzani & Salzano, 2004) (Fig. 2.9):

$$Y = k_1 + k_2 \ln(J) \quad (2.31)$$

where $k_1 = 4.5$ and $k_2 = 0.3$. These values can be easily included in QRA assessment.

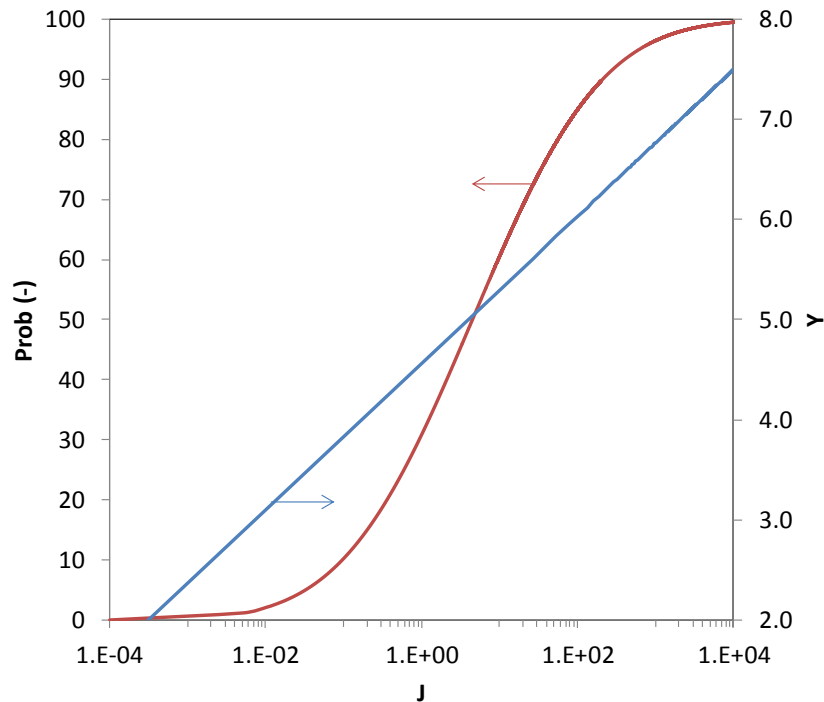


Fig. 2.9 The cumulative distribution function and the corresponding probit function Y vs Johnson number J.

A useful review for evaluating the mass and the velocity of the projected objects for domino effects can be found in the recent literature (Tugnoli et al., 2013). Here, it is worth noting that the characteristics of debris are completely different from the fragmentation of a warhead or more in general cased explosives, and typical equations like Gurney's correlation are not reliable (Salzano & Basco, 2015). Indeed, in applying the damage number, it can be assumed that the produced fragments are always within the "moderate velocity" regime i.e. in the sub-ordnance range (up to approximately 500 m/s), and that fragments have non-perforating shape as in military bullets. Besides, there is very little non-military investigation into larger scale impact situations such as those that may be encountered following an explosion of a piece of machinery, i.e. thick plates struck by flat faced, non-perforating projectiles (Salzano et al., 2003b).

For industrial accidents, the penetration depth ζ by projectile or debris may be in the first instance the reference value for the loss of containment and subsequent accident scenario. If ζ exceeds the wall thickness θ of the shell of reactors, tanks, or equipment, a domino effect is likely. To this aim, the penetration by small and large fragments has been reported in the classic Lees' textbook (Mannan, 2005; Gubinelli et al., 2004) in terms of minimum thickness $\zeta = \theta$ (in meter), which is required to stop the penetration of fragment with mass m_p (in kg):

$$\zeta_{small} = k_s m_p^a u_o^b \quad m_p \leq 1 \text{ kg} \quad (2.32)$$

$$\zeta_{large} = k_L \frac{m_p}{A_p} \log_{10}(1 + 5 \cdot 10^{-5} u_o^2) \quad m_p > 1 \text{ kg} \quad (2.33)$$

where u_o is impact velocity, k is the constant for small (S) or large (L) fragment with surface A_p (m^2); a and b are constants which depend on the target material, as reported in the following Table 2.23.

Table 2.23 Constant values for the equations for fragment penetration.

Target material	k_s	K_L	a	b
Concrete	$1.8 \cdot 10^{-5}$	$1.0 \cdot 10^{-3}$	0.4	1.5
Brickwork	$2.3 \cdot 10^{-5}$	$2.5 \cdot 10^{-3}$	0.4	1.5
Steel	$6.0 \cdot 10^{-5}$	$5.0 \cdot 10^{-5}$	0.3	1.0

3 CI-A2: Large dams in the Valais region of Switzerland

3.1 INTRODUCTION

Large dams vary greatly in terms of design, size, and aim. Some of the main purposes of large dams are water storage for irrigation and human consumption, hydropower production, or flood control, but some others exist (Schleiss & Pougatsch 2011). Often, multipurpose dams aim to fulfil several of these in parallel. Naturally, purposes affect operations and, ultimately, the dam's behaviour and vulnerability.

Although the definition of "large dam" is not universally agreed upon, it is usually based on dam height and reservoir storage volume. Infrastructures commonly classified as large dams can range from 15 m to more than 300 m in height, holding reservoirs from a few million cubic meters to more than 100 cubic kilometres.

In terms of design, two main types of large dams can be highlighted: embankment and concrete dams. While numerous subclasses exist, embankment dams can be summarily divided into earthfill and rockfill structures, depending on the materials used, while most concrete dams can be broadly identified as arch, gravity, or buttress, depending on the load distribution within the structure and the interaction with the foundation and the abutments.

Regardless of their specific characteristics, dams operate by storing substantial volumes of water in the upstream reservoir, the release of this water to downstream areas being controlled according to operational guidelines and targets. In view of that, in order to correctly frame risk and vulnerability assessments for dams, one should consider, beyond the dam body, the reservoir, the appurtenant structures (e.g. spillways, bottom outlets, or hydropower systems) and, most importantly, the downstream areas potentially affected by floods.

Following a dam failure, typically characterized by an uncontrolled release of the reservoir, a large amount of water travels downstream in the form of a dam-break wave. Such waves travel extremely fast and have enormous eroding power, as well as transport capacity. They affect downstream areas more seriously than natural floods due to their velocity, magnitude, and the large amount of debris usually carried.

While the dam-reservoir system is vulnerable to several hazards and monetary losses associated with it in the event of a failure amount to very large figures, the lion's share of the losses associated with a dam failure are likely to occur downstream.

A recent example that illustrates the destructive power of a dam-break wave is the Taum Sauk Upper Reservoir failure that took place in Missouri, U.S.A., December 2005 (Hendron Jr. et al., 2006). In this pump-storage system, the overtopping of the approximately 30 m high dam was prompted by water continuing to be pumped in after the reservoir attained its full level (Fig. 3.1). Following the overtopping and ensuing erosion of the embankment, nearly 8 million m³ of water were released downhill, stripping the slope clean of trees and the first layers of soil (Fig. 3.2).



Fig. 3.1 Aerial view of the Taum Sauk dam following its overtopping and failure, in 2005. U.S. Geological Survey.



Fig. 3.2 Aerial view of part of the area affected by the Taum Sauk dam-break wave. U.S. Geological Survey.

Another example of the extraordinary destructive power of water is the Vajont disaster, which took place in Italy, October 1963. The event was prompted by a major landslide of 270 Mm³ at the slope of Mount Toc, which, upon reaching the partially filled reservoir, led to a wave of over 100 m overtopping the dam (Müller-Salzburg, 1987; Hendron Jr & Patton, 1987; ICOLD, 2000). Although the dam structure withstood the event, the village of Longarone, roughly 2 km downstream, was destroyed by the wave (see Fig. 3.3 and Fig. 3.4 for a before/after comparison). Along the Piave valley, the villages of Pirago, Rivalta, Villanova, and Faè were also affected. In total, approximately 2000 lives were lost.



**Fig. 3.3 View of the village of Longarone, Italy, prior to the Vajont dam disaster, 1960.
Unknown author.**



**Fig. 3.4 View of the village of Longarone, Italy, after the Vajont dam disaster, 1963.
U.S. Army.**

Although, as was emphasized, the downstream areas are extremely important for vulnerability and loss assessments, they are mostly reactive and have usually little effect on the dam-reservoir system, where failures start to unfold. As such, it is customary and advantageous to split dam failure analyses in two distinct parts: the dam-reservoir system and the downstream areas.

The dam and the reservoir constitute a dynamic system with significant feedback interactions by which dam states affect the evolution of reservoir volumes and the reservoirs, in turn, condition the dam's behaviour.

While the number of basic functional elements of a large dam (e.g. dam body, foundation, spillways, bottom outlets and, eventually, hydropower system) is relatively restricted when compared to other industries, most of these elements have at least indirect impacts on the system's integrity as they play a role in the management of the reservoir. Also, failures are not always prompted by the physical loss of components following an extreme event such as a major earthquake or flood; often they are the results of "softer" mishaps such as sensor malfunctions, deficient communications and responses, lack of power, difficult access to control points, etc. Taking into account all these aspects can render the risk assessment for a large dam a very complex exercise.

As put forward in Mignan et al. (2015) dams can be affected by natural, internal, operational, and societal hazards. Among the first are earthquakes, floods, landslides, rock falls, avalanches, ice, outlet blockage, and meteor strikes. Internal hazards relate to a deterioration of the dam, foundation, or key operational elements such as spillways. They can come in the form of seepage, piping, sediment accumulation, instability on the foundation or abutments, embankment erosion, embankment settlement, or concrete deterioration, for example. Operational hazards can be related to human errors and equipment malfunction (e.g. gate jamming or loss of power). Finally, societal hazards can take the form of acts of war, terrorism, vandalism, and others (Darbre, 1999).

Historically, dams have been most vulnerable during the initial filling of the reservoir with an acknowledgeable number of the recorded failures having taken place at this stage. Beyond the initial phase, the largest share of failures has been associated with embankment dams. In past records, floods have been the main natural hazard triggering dam collapse (Lemperiere, 1999). Focusing on embankment dams, Foster et al. (2000) evidence also the risk posed by piping – a form of internal erosion. In addition to these, aging, upstream dam break waves, and earthquakes are other examples of important hazards.

Because dams can be built in a range of varying designs – adapting to topography, hydrology, geology, availability of materials, technology, and intended purpose – there are many failure modes. Some few examples can be cracking of the shell or localized block instability for concrete arch dams, sliding or turning for concrete gravity dams, or internal erosion, overtopping, sliding, and liquefaction for embankment dams. Probing the causes leading up to failures adds an additional layer of complexity to the problem, as they are seldom routed in a single hazard and, more often than not, result from unfortunate combinations of events (e.g. Mignan et al., 2015).

3.1.1 Main components of risk evaluation efforts for large dams

The basic task in the attempt of evaluating the risk associated with a large dam is hazard quantification. Typical hazards that are taken into account are earthquakes, floods, mass slides into the reservoir, and equipment malfunction.

While the quantification of earthquake and flood hazards have been focused by researchers for decades, both fields remain dynamic and evolving at a fast pace. Quantification of other hazards, such as mass slides, equipment malfunctions, or communication failures, difficult accessibility, or human error, is much less developed and seldom addressed in detail.

After hazards have been quantified, their effect on the dam and appurtenant structures is evaluated. Typically, this is done by focusing on a limited number of reference scenarios, usually focused on a single hazard or the pre-determined combinations (e.g. through requirements that rare floods have to be successfully routed following an earthquake, or by assuming partial blockage or inoperability of outlet structures during extreme floods). For each scenario, the response of the dam-reservoir system is thoroughly evaluated, be it by conducting the mass-balance evaluation of the reservoir's contents during floods, or by analysing structural responses by means of finite element models.

Although nowadays such models can reproduce structural responses in great detail, there is little opportunity for validation in the face of extreme loadings. As a response, the International Commission on Large Dams (ICOLD) has sponsored 13 benchmark workshops that, from 1991 onwards, have served as a means for experts to compare and evaluate approaches, as well as to transfer knowledge. Details on past benchmark workshops can be found in ICOLD (2013).

As the potential losses associated with dam failures are often most relevant in downstream areas, the next component of risk evaluation is the estimation of outflow hydrographs and the flood routing downstream. In this regard, the responses of concrete and embankment dams vary substantially. In fact, while concrete dams tend to experience sudden collapses, embankment dams are expected to fail more gradually, as material is progressively washed downstream and the breach on the dam body widens. In both cases, the phenomena have been studied in the past and translated into simplified approaches for hydrograph estimation (e.g. Pilotti et al. 2010; Froehlich, 2008; Wahl, 2004). In particular cases, numerical 1D, 2D, and 3D approaches can also be used, including smoothed-particle hydrodynamics (e.g. Crespo et al., 2008).

Once the outflow hydrograph is known, the flood's propagation downstream must be focused. In order to characterize it, numerical models come again into play. Traditionally, and in particular for narrow, straight valleys, studies have been carried out resorting to simplified approaches (e.g. Paquier and Robin, 1997) or 1D numerical modelling (e.g. Gee & Brunner, 2005; Wurbs, 1987; Hicks & Peacock, 2005). Nowadays 2D approaches, more fit to model flood propagation through wide and/or winding valleys with obstacles to the flow (such as houses), are being increasingly used to that end (e.g. Frazão & Zech, 2002; Soares-Frazão & Zech, 2008).

Once inundation parameters have been estimated at the interest points downstream (traditionally water depth and time of arrival, but also water velocity, momentum, or shear stress), vulnerability of existing structures and infrastructures to these parameters must be accounted for and damages, along with loss of life, estimated. In this regard, only limited knowledge is available focusing on dam-break floods. While several authors have studied the impact of floods on several man-made structures, limited knowledge is available on the specific effects of dam-break waves, which are particular owing to their fast development, magnitude, and the fact that they usually carry a large amount of debris. In this sense, existing studies on the vulnerability to tsunamis can serve as a better proxy of the effects of dam-break waves. In order to estimate losses, damages can then be combined with economic values of buildings and infrastructure on the affected areas.

Finally, loss of life following dam failures is extremely difficult to predict and validate. This is because there have been relatively few areas affected by such events – providing little data on the subject – and because there are many factors affecting loss of life beyond inundation

parameters. In many cases, areas downstream of dams are equipped with flood warning infrastructure and populations are aware of the risks and of emergency procedures. The warning time before the arrival of the flood is therefore crucial, but so is the timing of the event (e.g. night vs. working hours), the performance of the warning system, the response of the authorities, the preparedness of the population, and the condition of the transport infrastructure.

In all, from hazard quantification to loss assessment, risk evaluation for dams is an intricate process which requires large computational efforts and from which a large measure of uncertainty cannot be removed. Due to this, risk assessments for dams, in their vast majority, tend to focus on risks associated with specific hazards or scenarios, whose true probabilities are hard to evaluate, instead of attempting to quantify overall risks.

3.1.2 Traditional approaches for risk assessment of large dams

The cost, complexity, and safety concerns associated with large dams justify that they are, to a large extent, considered prototypes in the scope of risk assessment endeavours. Also, regulators, designers, dam owners, and society in general are very much aware of the consequences of a large dam failure. Accordingly, design and safety criteria guidelines are regularly updated in national regulations and in the documentation issued by the International Commission on Large Dams (ICOLD).

Most countries promote a deterministic approach to dam safety assessment, according to which, it must be proven that the system can withstand extreme events, but the evaluation of the actions that would lead to failure is not necessarily undertaken. As a result, the actual probability of a dam failure remains in many cases unknown and, consequently, so does the associated risk (Mignan et al., 2015).

Designers' focus is placed in large measure on structural responses and hydraulic behaviours, which are nowadays predicted with great accuracy. However, studies look above all else to selected limit scenarios based on the paradigm that systems designed to overcome extreme events will be able to withstand combinations of more frequent and less severe hazards. Also, they are often conservative in an attempt to abide by regulations and good practices, and not necessarily concerned with quantifying risk. Although historically this paradigm can be argued to have served society well, as dam engineering and dam safety regulations evolve and dams become increasingly apt to resist limit scenarios, the main sources of risk can progressively shift from these "hard" limit scenarios to "softer" combinations of events.

Dams, like many other complex systems, can be vulnerable to unforeseen combinations of relatively common events, either independently of following a major hazard, bringing about a dam failure. In fact, it can be argued that many failures resulted not from extreme demands alone, but rather due to combinations of extreme demands with much more common occurrences (e.g. equipment malfunctions, human error, communication difficulties, etc.). Attention these composite scenarios have only now began to gain weight among the dam engineering community. At present, they remain very difficult to study and characterize.

Despite the prevalent deterministic approach to dam design and safety regulations, there have been attempts to prepare generic frameworks for the classification and prioritization of the risks associated with dams. Part of these has been notably based on Failure Modes and Effects Analysis (FEMA), Event Tree Analysis (ETA), and Fault Tree Analysis (FTA)

(Hartford & Baecher, 2004). Although providing valuable insight on risk, these methodologies are not practical when aiming to look into the risk associated with several concurrent hazards and many interacting system components. In addition, they rely heavily on expert judgement in order to identify which failure modes to include in the analysis and quantify the transition probabilities in each node of the logical trees. Such probabilistic risk assessments for dams are rare and costly procedures, mostly justified only when particularly sensitive assets can potentially be affected by a dam failure (e.g. nuclear power plants). Because of the specificity of each infrastructure, the findings of the limited number of detailed probabilistic risk assessments carried out to date are also not easily transposed to other systems (Mignan et al. 2015).

3.1.3 Overview of this contribution

The present contribution follows the work described in STREST deliverable D3.5 (*Report on cascading events and multi-hazard probabilistic scenarios*), in which the Generic Multi-Risk (GenMR) framework was adapted and applied to large dams.

Recognizing that the dam-reservoir system is intrinsically dynamic and subject to numerous interactions between different components of the dam, the reservoir, and hazards, the proposed framework aimed to assess the overall risk associated with a conceptual large alpine dam operating from a period of one year. In other words, beyond looking at isolated sources of risk or reference scenarios, the methodology sought to gain insight on the role of hazard interactions and the dynamical nature of the system.

In the scope of D3.5, the analysis was limited to the dam-reservoir system. Here, it was extended as to include additional types of hazard interactions and to encompass the downstream areas.

The emphasis at this stage is placed on vulnerability – mostly related to the outflow hydrograph and flood propagation – losses being deferred to a subsequent document.

In the following subchapters, the methodology is described based on a conceptual case study of a large alpine earthfill dam. The GenMR framework principles, natural hazard characterization, modelling of the dam-reservoir system, flood routing, vulnerability assessment, and risk model are addressed with reference to literature and the proposed conceptual case study. Finally, acceptability criteria and risk-informed decision, along with the uncertainties that are unavoidable in such an endeavour, are discussed.

3.2 METHODOLOGY FOR THE PERFORMANCE ASSESSMENT

3.2.1 The Generic Multi-Risk (GENMR) framework

The GenMR framework is based on a sequential Monte Carlo method and its principles are well described in Mignan et al. (2014). It presents a powerful and flexible way to characterize the often broad range of risks associated with complex systems and is particularly well-suited to model hazard interdependencies. In short, it conducts multiple simulations of a given system for a chosen period (usually one year), generating random events, evaluating the system's responses to them, computing damages, and assessing losses.

In order to frame the problem, events must be defined in terms of their probability of occurrence, intensity, and timing. The characterization of system elements requires the statement of vulnerability functions, recovery rates, and associated losses. Finally, event dependencies must be stated, notably in the form of an altered probability of occurrence, which constitutes a remarkably powerful approach.

As GenMR addresses low-probability events, it requires that a very high number of simulations is undertaken in order to quantify risks. For complex systems, the computation burden of executing a full evaluation for each simulation can be overwhelming. Also, it can be wasteful due to the fact that, in the large majority of the simulations, the low-probability events that may have an impact on the system will simply not occur.

The problem is elegantly solved by performing two separate evaluations of the system. The first focuses solely on the generation of primary hazards and is computationally cheap. The second evaluation, which requires that the full evolution of the system is performed, is only carried out for the simulations which registered at least one primary hazard. During this second evaluation – also referred to as resampling – the system is incrementally evaluated from one event to the next event. At each step, future events that are directly or indirectly dependent of those already observed are resampled. At the heart of the methodology are the matrices that define event dependencies and thus, control the process.

The application to large dams profits from the GenMR framework's capability to cope with the difficulties underpinning the assessment of the risks associated with a large dam. It builds on two preliminary adaptation of GenMR to large dams (Mignan et al. 2015; Matos et al., 2015).

Regarding dams as dynamic systems, there was a need to couple a reservoir routing model with GenMR. Resorting to it, the reservoir's volume and outflows are computed at each step of the resampling. As this is done, the functionality of each outflow element of the dam (such as hydropower system, bottom outlet, spillways, or crest), incoming flows (including floods), and operational orders (such as drawdown attempts) are taken into account.

All is coded in terms of events (actions or acknowledgement of an internal state) and elements (objects within the system). Events can be triggered spontaneously (if they have an associated return period), as the result of earlier events, due to specific element states (e.g. a threshold damage of the dam), or as a response to reservoir levels.

After describing the dam-reservoir system, information on outflows becomes available. In the minority of the resampled years where a failure is predicted, a simulated hydrograph must be propagated downstream. Although depending on valley geometry and occupation, it can be said that, in general cases, simplified models for dam-break flood routing can be inaccurate.

On the other hand, detailed 1D and, particularly, 2D numerical models applied for flood routing can be computationally demanding and, thus, cannot be possibly run for every failure event generated within the GenMR framework.

Accordingly, it is proposed that coupled 1D/2D models are applied for a range of possible outflow hydrographs and resulting inundation parameters are evaluated over the affected areas downstream. Using these results as a basis, a regression model can then be employed in order to predict, in a computationally efficient way, inundation parameters for all possible hydrographs outflowing from the dam.

Based on selected predicted inundation parameters, combined with vulnerability functions for structures and infrastructures downstream, damages can be assessed. Adding information about economic values, losses can also be estimated. Regarding loss of lives, a similar process may be employed.

Uncertainty is prevalent within the GenMR process. It stems not only from the range of possible hazards that are considered, but also from the inaccurate information on the system elements' responses (regarding functionality and vulnerability), the deficient information about model parameters, and the possible shortcomings of the models themselves.

Through the application of GenMR to large dams, some insight can be gained on the overall risk associated with these infrastructures throughout one year of operation. The proposed approach represents a breakthrough regarding dam risk assessments as most previous attempts typically focused on a very restricted set of hazards and departed from fixed initial conditions (e.g. full or empty reservoir levels). Notwithstanding its flexibility to include a wide array of different hazards and model a large number of system elements and their interactions, the results obtained by GenMR are bounded by the quality of available information on hazards and the system itself. Where large dams are concerned, there is still a shortage of information on human causes for failure, as well as a lack of information on the distinct system components' vulnerabilities. Additionally, with GenMR resorting to Monte Carlo sampling, the more hazards and elements are added to the system, the more sampling points need to be retrieved in order to obtain stable results.

In all, the proposed approach is still far away from being able to present very accurate figures for the overall risk associated with large dams. Despite this, it can be profitably used in order to identify the most relevant sources of risk and compare competing solutions. A scheme of the proposed framework is presented in Fig. 3.5.

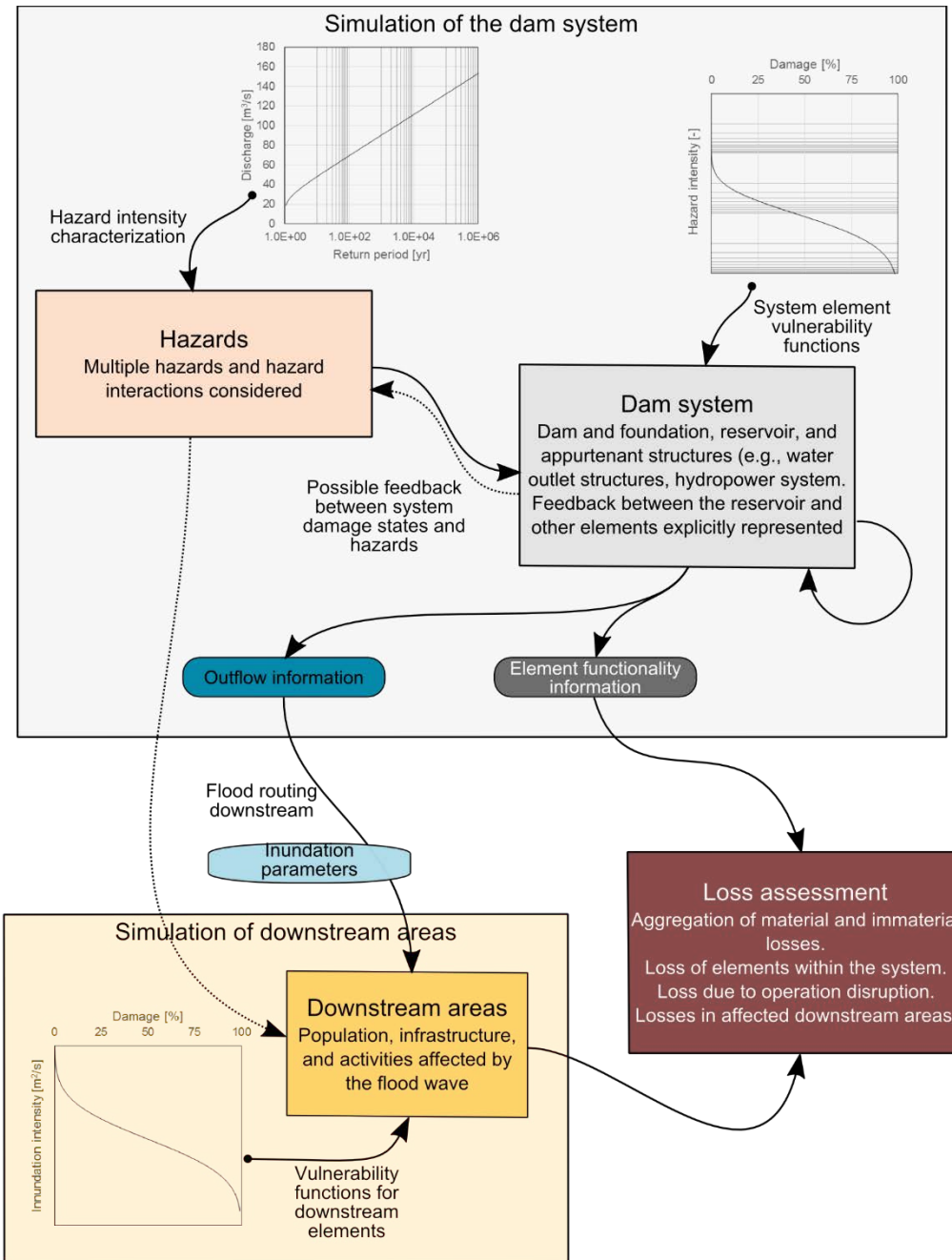


Fig. 3.5 Proposed framing of vulnerability and loss assessment for large dams. The analysis of potentially affected areas is downstream adds to the simulation of the dam system. The relationship between both “blocks” is achieved through flood wave routing.

3.2.2 Description of the studied conceptual dam

The proposed framework was applied to a conceptual large earthfill Alpine dam in Switzerland which, although inspired in existing structures, had some of its key characteristics modified.

The structure was assumed to be 90 m high, with embankment slopes of 2:1 and an 800 m crest, 10 m wide at the top.

The relevant appurtenant structures were assumed to be an uncontrolled spillway, a bottom outlet, and the hydropower system.

The drainage basin was admitted to have a surface of 40 km² and, in behaviour typical of high altitude Alpine catchments, runoff is mostly concentrated during the spring and summer seasons, when snow melting adds to rainfall. Inflows were also considered uninfluenced by hydraulic structures upstream.

The maximum supply level was assumed to be 93 Mm³, and uncontrolled spillage starts when the reservoir holds 100 Mm³. The crest is reached at 107 Mm³ and average yearly inflows amount to 120 Mm³ of water. The freeboard was set at 5 m.

The main purpose of the dam was assumed to be hydropower production. As such, the full volume of the reservoir was allowed to be exploited throughout the year. Minimum levels are attained just before spring, when the reservoir starts to fill up until the end of the summer. The simulations always start in March, from a practically empty reservoir level, in order to discount as much as possible eventual contributions from events occurred in earlier years.

3.2.3 Natural Hazards

Overview

In agreement with STREST's stated goals, the present work focuses on natural hazards. Among these, dams are notably affected by earthquakes, floods, and mass slides. In addition, embankment dams are critically vulnerable to episodes of internal erosion and seepage and Alpine dams are potentially vulnerable to icing.

References on the characterization of earthquakes and flood hazards are numerous and, in every large dam design or safety assessment, they are accounted for in detail. Convenient summaries of the vast body of knowledge amassed on both subjects and its application to dams can be found in the bulletins of ICOLD (1992; 2003; 2014; 2012). Mass slides, including landslides, rockslides, debris flows, or avalanches, have also been addressed by ICOLD (2000). In relation to earthquakes and floods, they are more site-specific and arguably harder to quantify. Also, their effects on the dam-reservoir system are heavily dependent on reservoir geometry (Sarrasin, 2015).

Icing can have an impact on the forces acting on a dam's structure, however, it affects mostly mechanical equipment such as spillway gates and, as stated before, our conceptual spillway was assumed to be uncontrolled. As such, icing was not accounted for.

GenMR accounts for discrete intervals of hazard intensity. In the case of primary hazards, these intervals were divided from a return period of 10^{2.5} (roughly equivalent to 316 years), to a return period of 10^{6.3} (roughly equivalent to 1 260 000 years), which exponent variations of 0.3. In all, 12 bins were analysed.

Earthquakes

As reported in STREST's D3.5 (Mignan et al., 2015), the earthquake hazard was quantified with basis on the Swiss dam safety regulations (OSOA, Ordonnance sur la Sécurité des Ouvrages d'Accumulation) (Federal Office for Water and Geology, 2002). In order to do so,

Medvedev-Sponheuer-Karnik (MSK) intensities of ground shaking for return periods of 1 000, 5 000, 10 000 years were quantified and used to fit a law in the form of Eq. (3.1) here I_{MSK} represents the ground shaking intensity, T stands for the return period, and a and b are constants:

$$I_{MSK} = \left(\frac{\ln T}{b}\right)^a \quad (3.1)$$

From the ground shaking intensity, the Peak Ground Acceleration (PGA) was derived using Eq. (3.2), as in the OSOA.

$$PGA = 10^{[0.26 \cdot I_{MSK} - 1.81]} \quad (3.2)$$

The resulting laws are illustrated in Fig. 3.6 and Fig. 3.7 as a function of the return period of the earthquake.

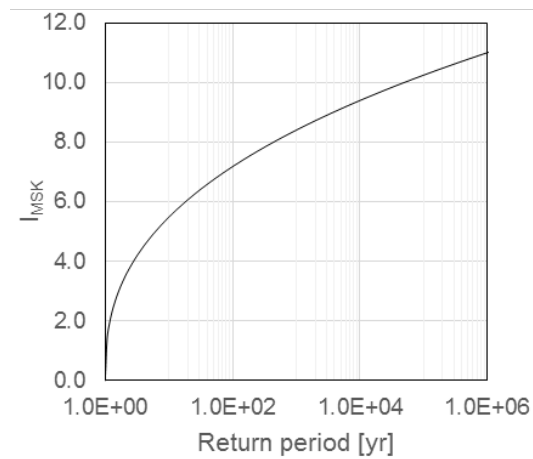


Fig. 3.6 Medvedev-Sponheuer-Karnik (MSK) intensities of ground shaking admitted for the area under study.

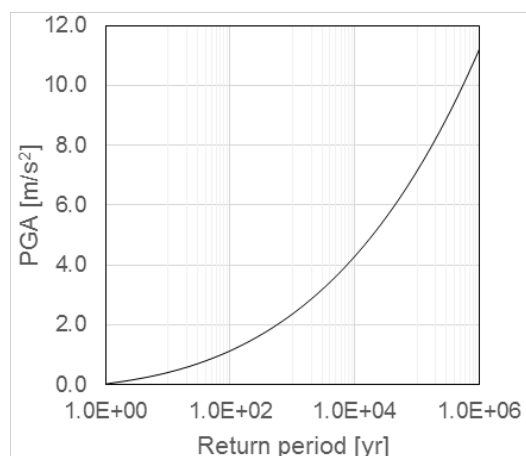


Fig. 3.7 Peak ground accelerations (PGA) admitted for the area under study.

Although the method proposed in the OSOA documentation is aimed at dam design, not necessarily being the best option for a risk assessment effort, at the present state its adoption is enticing as large dams in Switzerland have been evaluated in regard to it. Facing presently the lack of accurate vulnerability functions generically applicable to large dams, the possibility of comparing the vulnerability curves put forward below with a reference earthquake that the system was designed to withstand is interesting.

Earlier this year, new Swiss earthquake hazard intensity maps have been published. They can point towards higher intensities than the maps upon which current regulations are based for the very high return periods and how this new information will ultimately influence future legislation and recommendations is still under study. It should be highlighted that, although insight on the effect of the new estimates of earthquake intensity measures on existing dams is very valuable, the present work is based on the old figures.

Floods

Flood hazard quantification was updated in relation to the one used in STREST's D3.5 (Mignan et al. 2015). The probability of the peak discharge was modelled using the Generalized Extreme Value (GEV) distribution, one of the common options to probabilistically represent peak discharges:

$$F(x|\mu, \sigma, \xi) = e^{-\left[1+\xi\left(\frac{x-\mu}{\sigma}\right)\right]^{-1/\xi}} \quad (3.3)$$

The parameters of the distribution are μ (location), σ (scale), and ξ (shape). The admitted extreme discharge distribution is presented in Fig. 3.8.

Beyond the peak discharge, duration must be associated with the flood event in order to allow for the computation of flood volumes and their influence on reservoir levels. Although possibly modelled by joint distributions (e.g. Grimaldi & Serinaldi, 2006; Favre et al., 2004), peak discharges and flood durations can also display very low correlations. After an exploratory analysis of the hydrological data over the region, the duration of the flood was considered independent from its peak discharge. Based on historical records of floods in an alpine catchment of similar characteristics to the one envisaged in this conceptual case, a probability density for the flood's duration was approximated using the lognormal distribution (Fig. 3.9). Based on the same records, a simplified normalized hydrograph, specifying the time distribution of the flood event, was computed (Fig. 3.10).

Finally, it was supposed that the probability of a flood event taking place is not constant throughout the year. In a simplified manner, it was assumed that the distribution of flood events throughout the year follows roughly the distribution of discharges inflowing to the dam. This distribution is represented in Fig. 3.11.

Interactions between flood events of different return periods were also accounted for. In this sense, the fact that an extreme flood occurs will lead to an update of the probability of occurrence of more frequent flood events, which become marginally more likely until the end of the simulation. The process is described in Mignan et al. (2015).

Going well beyond the chosen characterization of the flood events affecting the conceptual dam under study, a wealth of methods and models for flood peak estimation have been proposed in literature and the topic remains very much active today. Of particular interest to risk assessment efforts is the study of the uncertainty associated with each method, which were not included in this application of GenMR, but would be extremely interesting to look into.

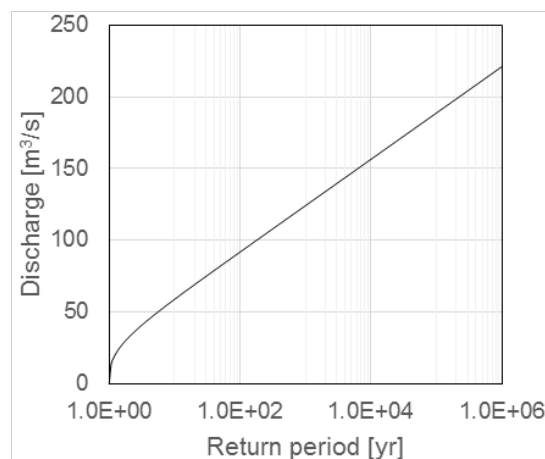


Fig. 3.8 Peak flood inflows to the reservoir.

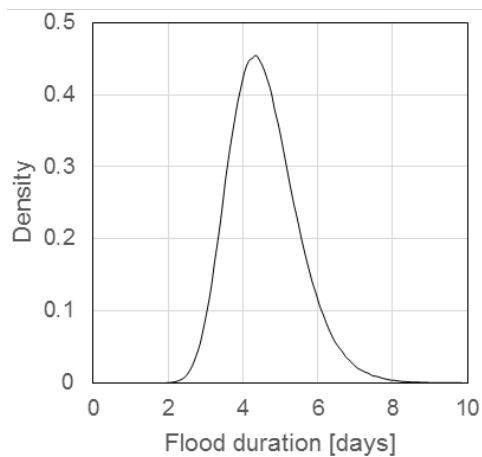


Fig. 3.9 Probability density of a flood's duration.

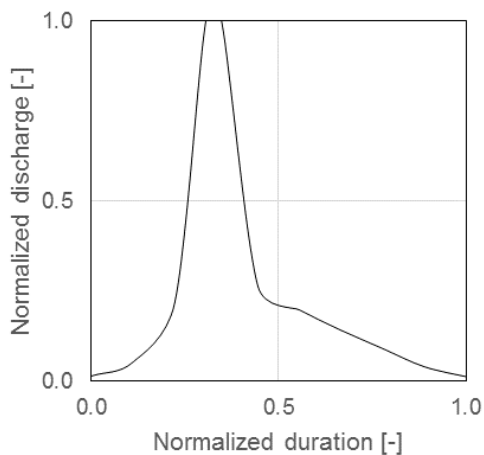


Fig. 3.10 Normalized hydrograph of flood inflows.

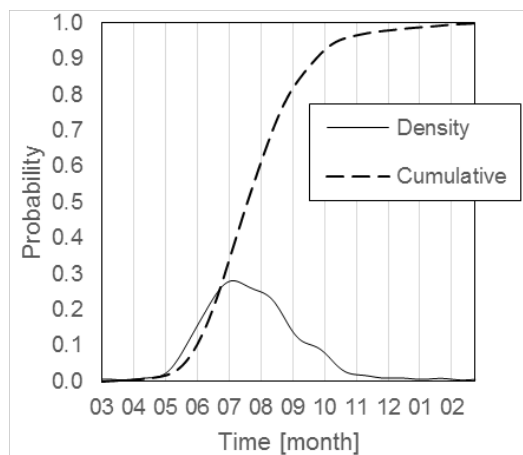


Fig. 3.11 Admitted probability of occurrence of a flood throughout the year

Internal erosion

The quantification of the internal erosion hazard in embankment dams is complex due to the multiple factors that affect its occurrence (e.g. foundation material, dam composition and design, quality of the construction, reservoir levels, or maintenance standards) and the relatively small historical record of internal erosion episodes in large dams (conditioning the employment of statistical approaches). Frameworks for its inclusion in probabilistic risk assessments have, however, been developed (e.g. Altarejos-Garcia et al., 2014).

Very recently, in the scope of the 13th ICOLD International Benchmark Workshop on Numerical Analysis of Dams, a session was organized in order to discuss different strategies and methodologies to assess the probabilities of failure on homogeneous core earthfill dams (Andreev & Zhelyazkov, 2015; Mouyeaux et al., 2015; Westberg & Borragan, 2015). Although promising, the reported findings focused on slope instability and overtopping events and can only, therefore, be of indirect application to internal erosion or seepage hazards.

Expert judgement was used to quantify the phenomenon for the studied conceptual dam resorting to a cumulative lognormal distribution function. The resulting law is illustrated in Fig. 3.12. In its derivation it was assumed that the conceptual dam structure and foundation present a large factor of safety regarding internal erosion and that it was designed, built and operated following state-of-the-art practices.

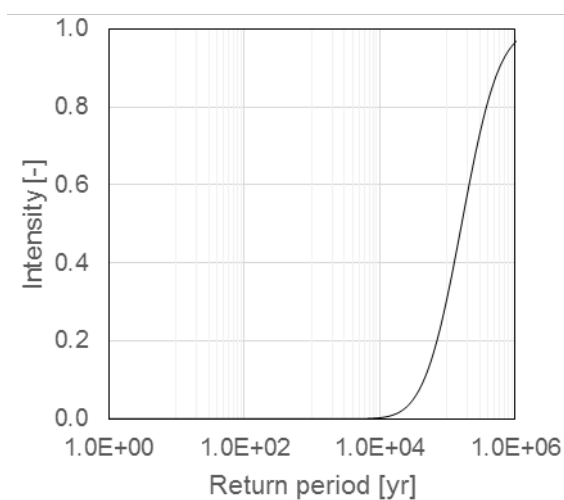


Fig. 3.12 Intensity of internal erosion events admitted for the dam under study.

Soil mass slides

Soil mass slides present a relevant hazard for dams, particularly so when the reservoir stands on relatively narrow valleys flanked by steep slopes. In addition, at high altitudes excessive accumulation of snow can lead to avalanches of significant mass.

Unlike foods or earthquakes, for whose characterization regional laws or maps can be employed, soil mass slides are very much dependent of specific slope characteristics and geotechnical properties which are not always readily available. Once the moving soil mass displaces the water, impulse waves are generated through a complex process (Heller et al.,

2008; Fritz, 2002) and start traveling through the reservoir, gradually losing energy and, eventually, interacting with the dam's body and/or margins. The process of wave run-up and overland flow that takes place once the waves reach the limits of the reservoir has also been characterized (Fuchs, 2013). An overview of the whole process can be found in Heller et al. (2009).

If the impulse wave overtops an embankment dam, a process of erosion of the aggregate material that comprises the dam might start to take place. Whether this process is severe enough to lead to a breach being formed depends on the level of the reservoir, the geometry and material of the dam, the duration of the overtopping event, and its eroding capacity.

Though numerical simulation of several possible soil mass slides on an alpine reservoir with volume similar to the one considered in the present conceptual application, Sarrasin (2015) has concluded that the point of impact of the mass slide on the reservoir also plays a major role in the likelihood of an eventual overtopping, because mass slides that enter the reservoir in a direction parallel to the dam's crest are expected to reflect between opposite margins, with a relatively lesser effect on the dam wall.

Due to the large uncertainty that still surrounds the generation and consequences of mass slides, their inclusion in GenMR's application to large dams has not been carried out in the scope of this document.

3.2.4 Critical infrastructure

Overview

The critical infrastructure in the scope of this problem is clearly the dam body. It can be affected by overtopping events, earthquakes, internal erosion and seepage, and slope instability.

The effects of these hazards and/or their likelihood are, however, intrinsically linked to the reservoir level and its variations. This is the case for earthquakes, whose effects on the dam are a function, not only of earthquake characteristics, but also of the mass of water that is mobilized against the dam and the distribution of interstitial pressures within the structure, which can provoke local instabilities or liquefaction. Again, this is the case for overtopping events, which can be a consequence of excessive inflows (floods), soil mass slides, or inoperability of outlet structures, but are always a function of initial reservoir levels. Finally, the reservoir plays also a role in internal erosion and seepage events as these ultimately prompted by a pressure gradient across the dam body and, as water levels in the reservoir become lower, this gradient tends to decrease.

The reservoir

The reservoir, in turn, is affected by inflows and dam operations. Stored water volume is a function of inflows (mainly in the form of contributions from rivers and rainfall) and outflows (a sum of evaporation, infiltration, and controlled discharges at the dam). The mass balance or retention equation that represents the process is transcribed below:

$$V_{t+1} = V_t + Q_t^{in} + P_t - Q_t^{out} - E_t - I_t \quad (3.4)$$

where V_t is the reservoir volume at time t , Q_t^{in} are the inflows, P_t is the direct contribution of precipitation over the reservoir, Q_t^{out} are the outflows controlled by the dam, E_t represents evaporation, and I_t is the infiltration component.

Inflows usually display significant intra- and inter-annual variability, even discounting the contributions of large floods. This variability is considered during dam design and should be taken into account in the scope of full risk assessment. In this case, however, in order to reduce the number of Monte Carlo samples required for GenMR's results to reach some stability, an average inflow scenario was adopted and floods superimposed on it.

Water flowing out of Alpine dams – characterized by relatively small reservoirs and limited evaporation – is almost exclusively controlled by the appurtenant structures, with the negligible exception of seepage flows (which, albeit extremely important in order to prevent internal erosion events, are usually insignificant in terms of the reservoir's mass balance). As such, spillways, bottom outlets, and the hydropower system, are responsible for reservoir control. In the rare event of overtopping, water flows also over the dam's crest, in an uncontrolled fashion and can, eventually, create a breach in the dam through which the reservoir's contents are quickly released.

The purpose of the conceptual dam being hydropower production, operations are assumed to be planned so that, as much as possible, power production and, consequently, outflows are constant throughout the year. When, due to abnormal inflows or disturbances to normal operations, the reservoir level departs from what is expected or desired, adaptations are made. This is done resorting to the bottom outlet or spillways. In the case of this conceptual case study, the spillway is uncontrolled and is functional while the reservoir's volume is over 100 Mm³. As shall be seen later, some hazards can affect the functionality of the appurtenant structures. When damaged, their outflow capacity is reduced and, therefore, so is the maximum outflow capacity of the dam.

The reservoir's contents are simulated according to Eq. 3.5). At each time step, t , the variation of the reservoir volume, V , is equal to the difference between gross inflows, $I(t)$ – a function of the time of the year –, and gross outflows, $O(\delta, \omega, V)$ – dependent on the damage state of relevant elements, δ , operational decisions, ω , and V :

$$\frac{dV}{dt} = I(t) - O(\delta, \omega, V) \quad (3.5)$$

Expected inflows, from March to February, are illustrated in Fig. 3.13. In order to simplify the analysis, a target volume curve was admitted. Given a history of inflows, operations are planned in order to approach this curve. When the simulated volume, V_{sim} , departs from the target volume, V_{tar} , at a given time step, the dam operation will attempt to outflow O_{att} according to Eq. 3.6). In the same equation α is the number of days that the system is given for V_{sim} to match V_{tar} from the end of the inflow perturbation. Δt represents the time step used in the calculations. The adopted target volume curve is represented in Fig. 3.14.

$$O_{att} = \frac{V_{sim} - V_{tar}}{\alpha} \cdot \Delta t \quad (3.6)$$

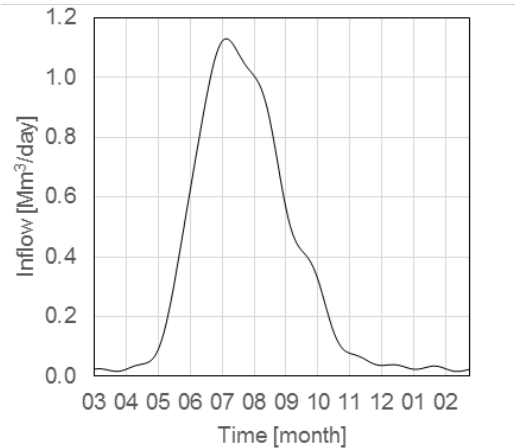


Fig. 3.13 Expected inflows into the reservoir.

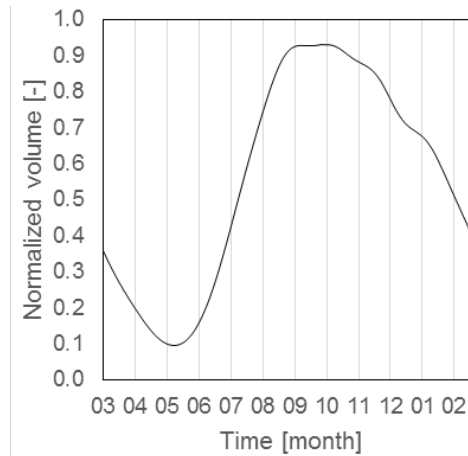


Fig. 3.14 Target volume of the reservoir throughout the year (normalized in respect to the volume of the reservoir at the spillway level).

Component description

The dam body is the main component of the system, as the main damage and risk states, addressed in a later section, are associated with it. A dam failure corresponds to an uncontrolled release of the reservoir. Following extreme loads, it can tolerate moderate deformations and develop cracks as long as the outflows remain under control. Beyond failure there is, however, little to add about the dam body from a system functionality perspective as it is considered to have no direct impact on other system components or downstream areas.

After a departure from the target curve, the simulated outflow cannot always be computed using Eq. 3.5). On the one hand, it is constrained by the maximum outflow capacity of the system and, on the other hand, it is subject to minimum outflows over the spillway and dam crest.

In a nutshell, the outflow capacities of the different appurtenant structures are a function of available energy (or water head) and losses of energy (head losses). Discharge functions for most types of appurtenant structure can be estimated using relatively simple equations, available in several books on hydraulics (e.g. Hager & Schleiss 2009). For a more detailed description of how discharges were computed for the case study, please refer to STREST's deliverable D3.5 (Mignan et al. 2015).

The maximum discharges associated with each element for a given reservoir volume can be inspected in Fig. 3.15.

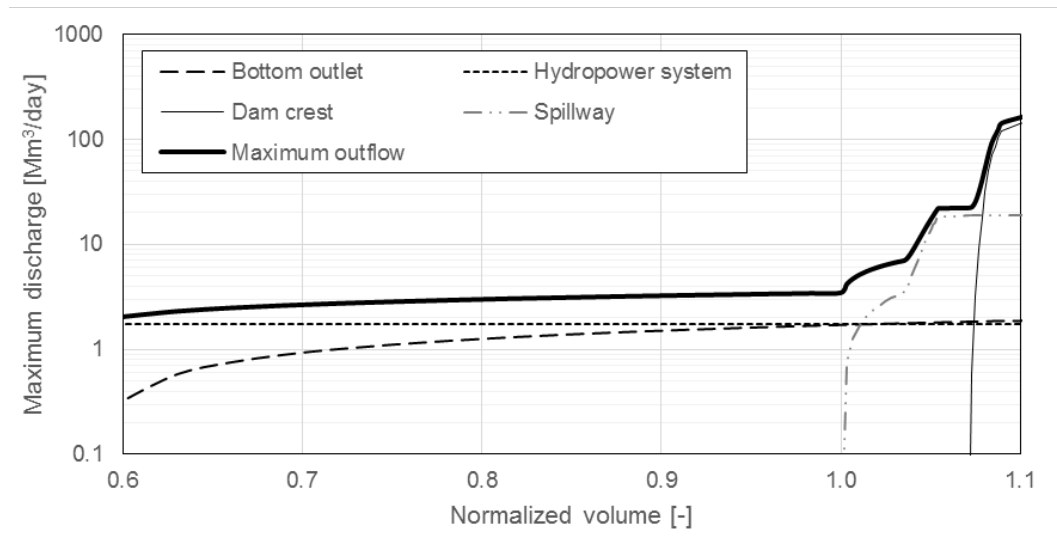


Fig. 3.15 Maximum outflows of the reservoir as a function of the normalized volume of the reservoir.

3.2.5 Dam-reservoir system

The dam-reservoir system, whose analysis is crucial in order to quantify risk states and establish conditions for downstream flood propagation has been described over the preceding subsections.

The scheme of considered interactions between hazards, elements, and reservoir, is synthesized in Fig. 3.16.

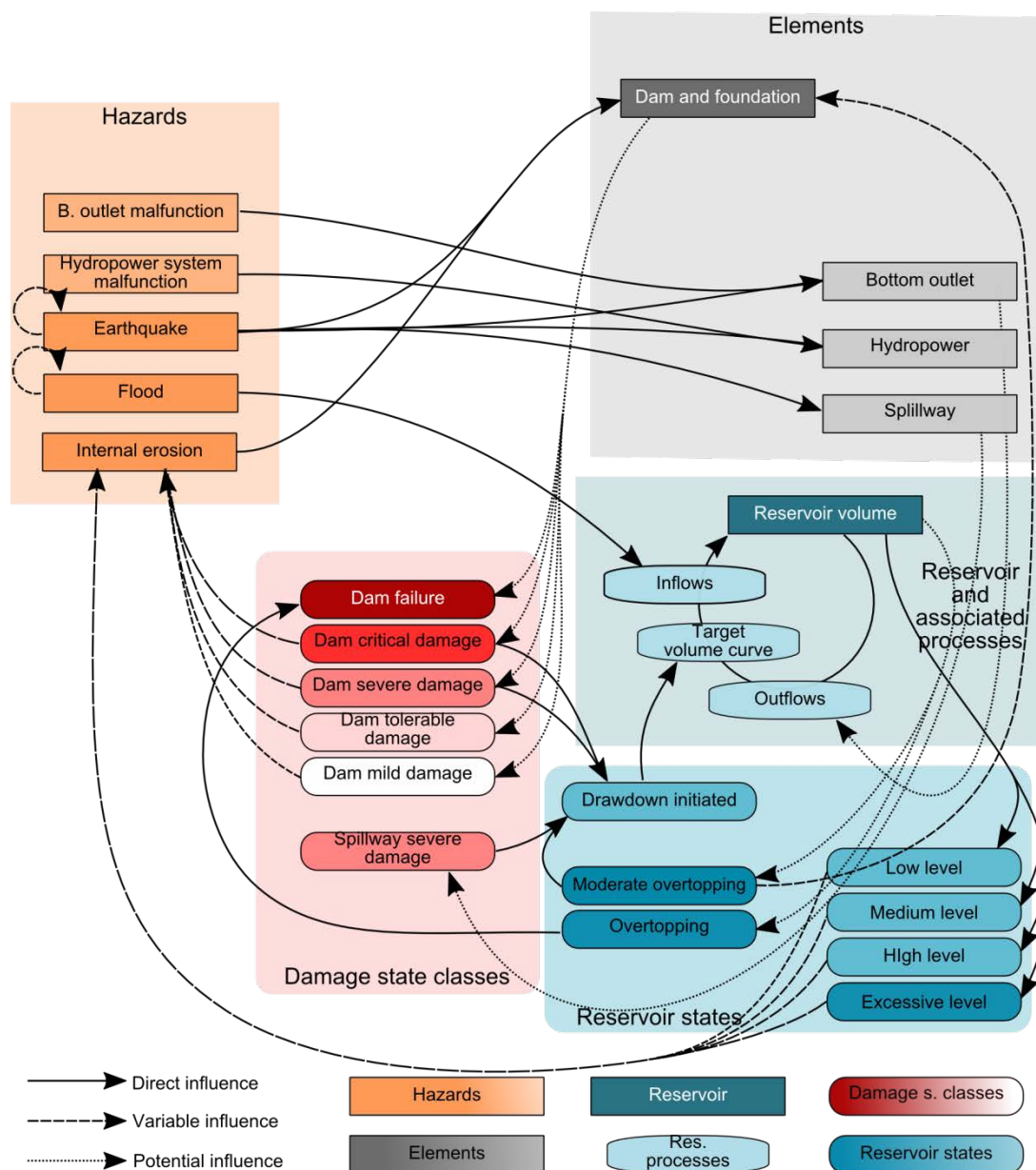


Fig. 3.16 Scheme of hazards, elements, system states, and interactions considered in the application of the GenMR framework to large dams. Adapted from Mignan et al. (2015) and presented in Matos et al. (2015).

Despite great simplification, the dynamic nature of the system is obvious and, it is believed, in order to account for it adequately, a time simulation of the system is required.

As an example, one can choose internal erosion. A relevant cause of failure for embankment dams, this hazard corresponds to the progressive “washing” of material from the dam body or foundation through pipes that progress upstream and can eventually lead to the formation of a full breach in the dam. The probability of occurrence and severity of internal erosion events is widely recognized to be both a function of reservoir levels and the integrity of a dam’s low permeability core, as well as filtering and drainage layers (if existing). As such,

this hazard should reflect both past damages to the dam, as well as reservoir levels; in other words, the history of the system.

In order to model this and other interactions, for each GenMR sample including at least one primary event, the dam-reservoir system was, albeit in a simplified fashion, modelled for a period of one year. An example of such a simulation is presented in Fig. 3.17.

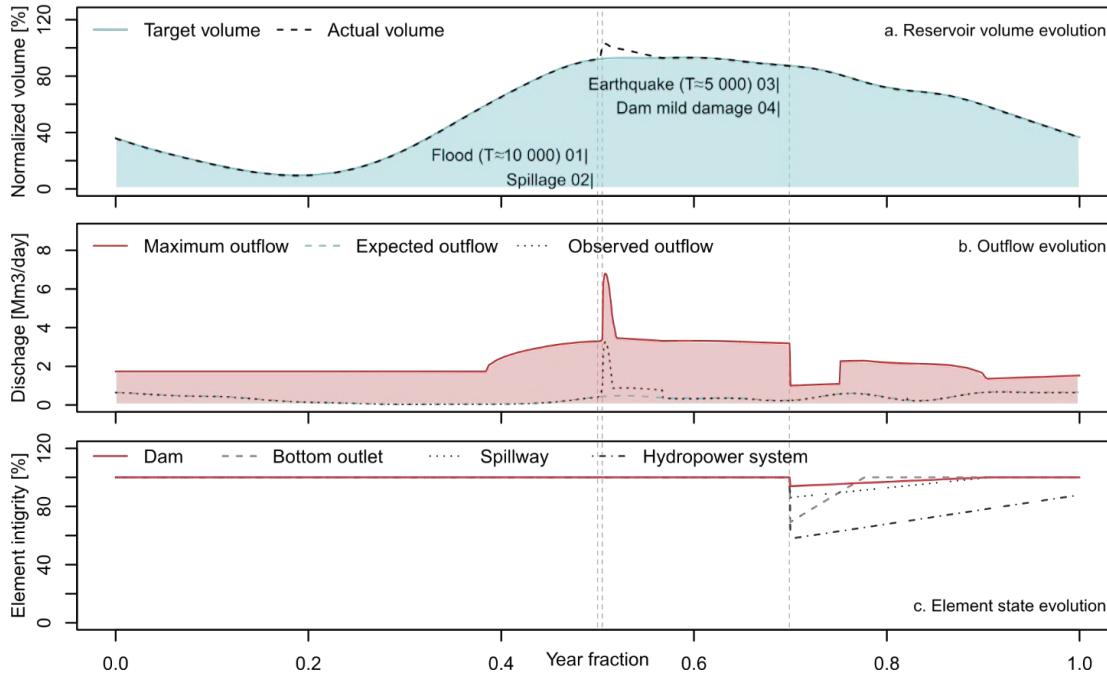


Fig. 3.17 Example simulation of the dam-reservoir system affected by a 10 000 year flood and a 5 000 year return period earthquake. On top: reservoir volume evolution. In the middle: outflow evolution. In the bottom: element state evolution. Adapted from Matos et al. (2015).

3.2.6 Vulnerability model

Damage states

The damage states considered were focused on the dam and foundation element and spillway. For the remaining system elements considered in the analysis, functionality was assumed to be proportional to integrity, down to a chosen threshold, below which the element is considered inoperable (in practical terms it cannot be used to regulate reservoir levels).

Assuming that, at 50% integrity, the dam is no longer capable of holding the reservoir, damage states were quantified as follows:

- Dam not damaged: integrity between 95 and 100%,
- Dam mildly damaged: integrity between 90 and 95%,
- Dam tolerably damaged: integrity between 80 and 90%,

- Dam severely damaged: integrity between 70 and 80%, and
- Dam critically damaged: integrity between 50 and 70%.

The spillway was associated with a single damage state – spillway severely damaged – which corresponds to an integrity below 85%. Below this level, the spillway was considered inoperable.

Not damage states per se, but relevant nonetheless, are the integrity thresholds below which the remaining outflow structures are assumed not to function. These amount to 90%, for the bottom outlet, and 50% for the hydropower system.

Risk states

The admitted risk states are of three sorts. Firstly, the issue of a drawdown order that signals the attempted reduction of the reservoir level by all means necessary in order to prevent eventual further damage to the dam. Drawdown orders were assumed to be issued if the dam is either severely or critically damaged or the spillway is severely damaged. Secondly, the occurrence of moderate and “full” overtopping. Moderate overtopping occurs when the water level over the crest is marginal (lower than 50 cm on a limited section of the crest) and, although the dam endures some damage, a full breach is not immediately developed. In opposition, “full” overtopping implies the failure of the dam. Finally, the dam failure risk state is considered in two forms – either caused, or not, by overtopping – as this is relevant for outflow hydrograph estimations.

3.2.7 Vulnerability functions

Critical components

Vulnerability functions for the proposed elements of the dam-reservoir system are hard to quantify without further work, for example resorting to finite element models. In fact, designers and, thus, most existing studies, are concerned with dam safety and, thus, focus on fragility rather than vulnerability.

Despite this, within the proposed GenMR framework application, which aims to assess overall risk, it is desirable that the history of damages to the dam is “recorded”, and fragility functions are not directly suitable to that end. In parallel, and as was mentioned before, most large dams should be regarded as prototypes and analysed in detail.

While such an analysis is highly recommended in a practical application, it is beyond the scope of this contribution and largely irrelevant to the demonstration of the proposed methodology. Therefore, it was assumed that the conceptual dam and appurtenant structures were designed in order to meet Swiss regulation requirements. From that assumption, vulnerability curves were derived through a reverse-engineering reasoning.

Earthquakes

In Figures 3.18 to 3.21, vulnerabilities to earthquakes for the different elements considered in the dam-reservoir system are depicted. As embankment dams are recognized to be particularly resilient to earthquakes, it was assumed that a 10 000 year return period earthquake would damage the structure without prompting the release of the reservoir, finally failing for a return period of approximately 1 000 000 years.

Resorting to a similar reasoning, the spillway’s vulnerability was defined such that, for a 10 000 year return period earthquake, it remains functional while, for a 475 years return period event, it withstands little damage. Given the range of different building solutions for spillways, it is also recommended that these elements’ vulnerabilities are individually evaluated prior to practical applications of the methodology.

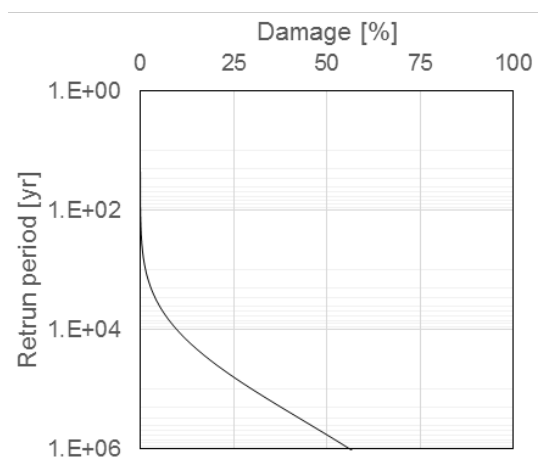


Fig. 3.18 Vulnerability curve of the dam and foundation to earthquakes.

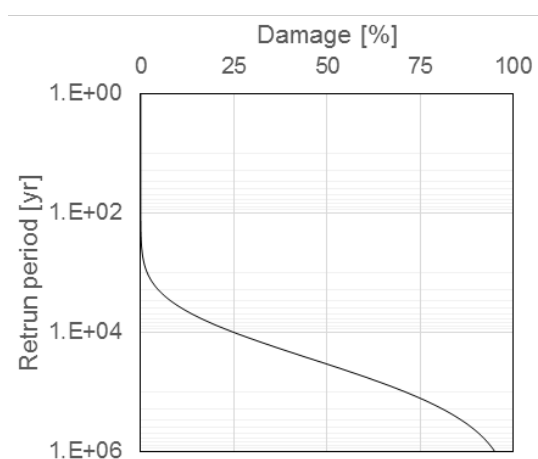


Fig. 3.19 Vulnerability of the spillway element to earthquakes.

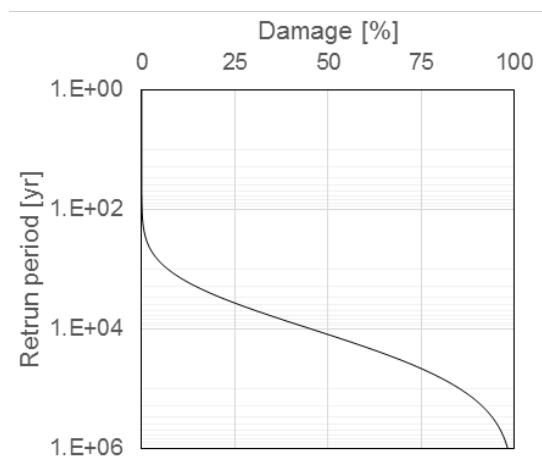


Fig. 3.20 Vulnerability of the bottom outlet element to earthquakes.

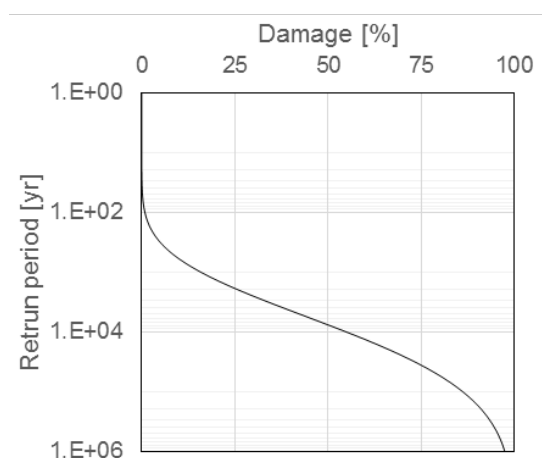


Fig. 3.21 Vulnerability of the hydropower system to earthquakes.

The bottom outlet and hydropower systems, including mechanical equipment, were modelled as being more vulnerable to the earthquake hazards than the spillway, particularly due to the risk of gates jamming. Again, there was little information found in literature that contributes to the quantification of the vulnerabilities of such elements to earthquakes.

The parameters of the applied log-normal curves, applied to PGA, are shown in Table 3.1.

Table 3.1 Parameters of the log-normal vulnerability functions to earthquakes (PGA).

Element	Location parameter (μ)	Shape parameter (σ)
Dam and foundations	-2	0.23
Spillway	-1.85	0.18
Bottom outlet	-1.95	0.19
Hydropower system	-1.6	0.29

Internal erosion

Only the dam and foundation element is considered vulnerable to internal erosion events. Internal erosion is a process which, after initiated, tends to develop very fast. In fact, as the more of the dam's material gets eroded, less resistance there is to the flow. This leads to more water exiting the dam body and ever more material being eroded, ultimately leading to a full breach being formed.

Due to this progressive behaviour, which is likely – but not guaranteed – to end a failure of the dam, it is not straightforward to specify the hazard's intensity measure and corresponding vulnerability function. As such, the intensities that were used to characterize the hazard in Fig. 3.12 are assumed to be proportional to the damage endured by the structure. The curve is particularly steep in order to capture the evolving nature of the hazard, but although based in engineering judgement, its applicability is admittedly debatable and should be the target of further investigation. The admitted parameters for this log-normal were μ of -12 and σ equal to 1.

Equipment malfunction

The equipment malfunction hazard affects the bottom outlet and hydropower system. It represents the possibility of gates being jammed, under maintenance, or inoperable due to motor failures. Unlike for the previous vulnerabilities, damages associated with equipment malfunction are limited, as neither system is expected to be completely destroyed by such an event. The proposed functions, based on statistics for mechanical equipment failure rates (Pohl, 2000), are depicted in Fig. 3.22 and 3.23 and detailed in Table 3.2. It should be stated, however, that such failure rates are heavily dependent on maintenance efforts and operability checks and, thus, are expected to vary widely between countries and even between dam operators.

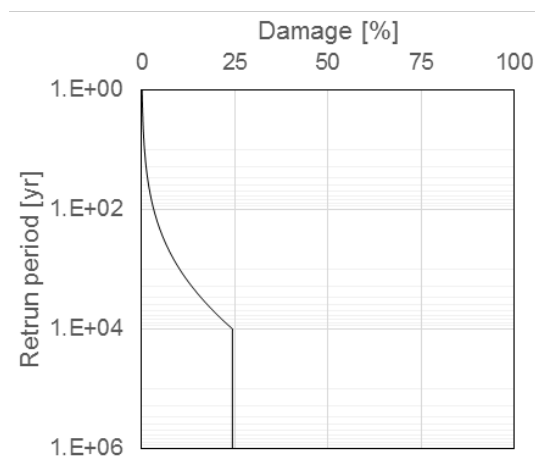


Fig. 3.22 Distribution of the damage induced to the bottom outlet element by equipment malfunction.

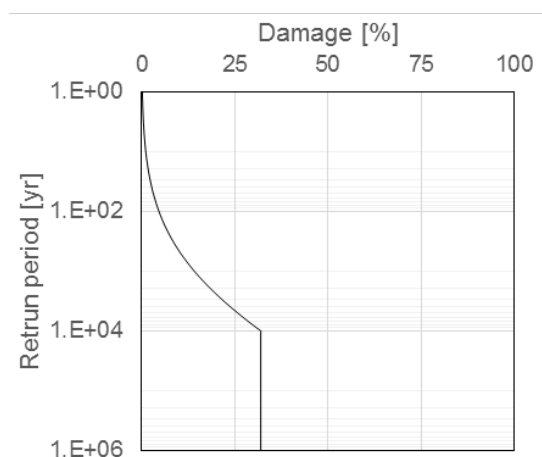


Fig. 3.23 Distribution of the damage induced to the hydropower system by equipment malfunction.

Table 3.2 Parameters of the log-normal vulnerability functions to malfunctions.

Element	Location parameter (μ)	Shape parameter (σ)	Cut-off value (damage, %)
Bottom outlet	-12	4	25
Hydropower system	-11	3.8	30

Moderate overtopping

Finally, the vulnerability of the dam to moderate overtopping was modelled as a uniform random variable, being that for every moderate overtopping event it suffers a damage of 5 to 20%.

Downstream structures and infrastructure

The vulnerability of downstream structures and infrastructures was modelled on the basis of inundation parameters. Unfortunately, there is little published information on the specific vulnerability of buildings to dam-break waves. As such, in the scope of this problem vulnerabilities are based on publications made for natural floods and tsunamis, the latter particularly interesting as they are expected to – similarly to dam-break waves – carry a large amount of debris and travel fast.

Inundation depth

There is a plethora of different potential sources for vulnerability functions to floods based on inundation depth. Notably the Hazus-MH software (Department of Homeland Security Division Federal Emergency Management Agency Mitigation Division 2006), includes over 700 functions adapted to different buildings and contents, vehicles, etc.

As put forward above, however, dam-break floods differ from natural ones in several aspects and, perhaps, a better proxy for damages associated with dam-break waves result from vulnerabilities derived for the tsunami hazard. In addition, vulnerability functions depend on the building practises in each country and are marked by great uncertainty, varying widely among publications (e.g. de Moel & Aerts, 2011). Adequate vulnerability functions Switzerland were not found.

An example of vulnerability functions specific for tsunamis were derived from the project SCHEMA following the 2004 Indian Ocean tsunami (Tinti et al., 2011). These are presented in Fig. 3.24 for five different classes of buildings. Of the five, A, B and C correspond to light and not reinforced structures unlikely to represent a large percentage of urban constructions in Switzerland. The remainder, curves D and E₁, are applicable, respectively, to “large villas or collective buildings residential, or commercial buildings: concrete not reinforced” and “residential or collective structures or offices, car parks, schools, towers: reinforced concrete, steel frame”.

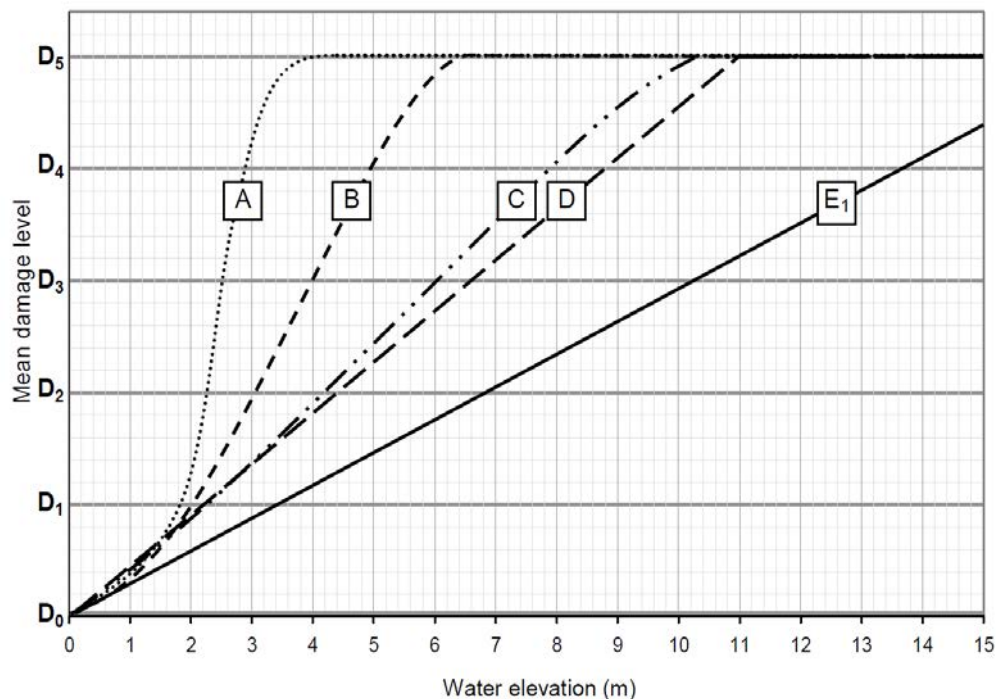


Fig. 3.24 Damage functions for several building classes derived from real field observations collected after the Indian Ocean tsunami occurred on December 26, 2004 developed during project SCHEMA by GSC. Reproduced from (Tinti et al. 2011).

Beyond the vulnerabilities derived in the scope of SCHEMA, a wealth of information on the fragility of buildings to tsunami action ensued from the 2011 Great East Japan tsunami (Suppasri et al., 2013). Fragility curves published from reinforced concrete structures were employed on the present case study.

Fragility curves derived by Suppasri et al. (2013) for two-stories reinforced concrete buildings are illustrated in Fig. 3.25 for six damage classes. These are:

- a) Minor damage;

- b) Moderate damage;
- c) Major damage;
- d) Complete damage;
- e) Collapsed;
- f) Washed away.

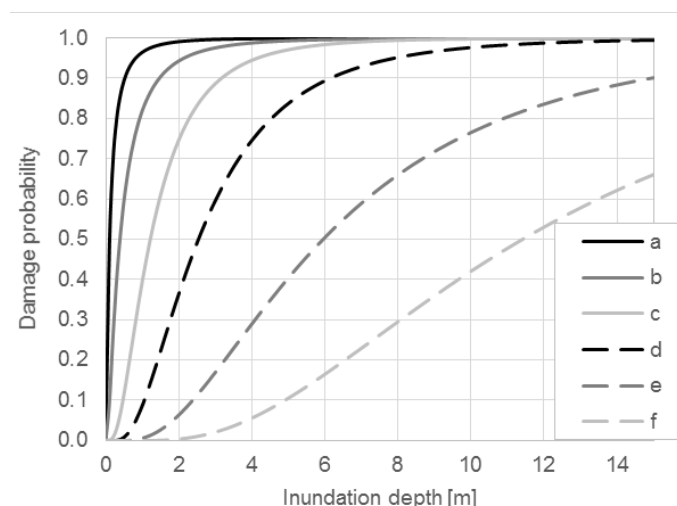


Fig. 3.25 Fragility curves derived by Suppasri et al. (2013) for two-stories reinforced concrete buildings.

Additionally to presenting curves for several types of building material and height, the authors highlight that building height plays an important role in observed damages, with constructions with more than three stories much less likely to be washed away, regardless of the building material.

Flow velocity

While water height is relatively easy to assess following a flood event, water velocity is more difficult to estimate. Partly due to this, the vast majority of flood-related vulnerability and fragility curves are based on the former. According to Kreibich et al. (2009), however, although water height constitutes a good predictor of structural damage to residential buildings, flow velocity works better as an independent variable for assessing damages to road infrastructure.

Even for buildings, it can be argued that accounting for flow velocities is important. In fact, for natural floods, the estimation of damages based on inundation depth alone implicitly assumes that either flow velocities remain below levels which pose a risk of structural damages or that flow velocity behaves as a function of water height. Dam-break waves can attain flow velocities that largely surpass those of natural floods and display highly unsteady behaviour, with steep rise and descent of water levels. Consequently, none of the implicit assumptions can be applied to them.

As an example, for the current case study and making use of only a fraction of the simulated data (roughly 1 000 000 points, refer to subsection 3.2.8), one can see that, although a correlation between simulated inundation depth and flow velocity indeed appears to be clear, there is ample scattering of the results (Fig. 3.26).

Because no fragility curves were found for road infrastructure affected by dam-break waves or tsunamis, four fictitious fragility curves were assumed in order to test the model (Fig. 3.27 and Table 3.3). These correspond to minor (a), moderate (b), major (c), and complete damage (d).

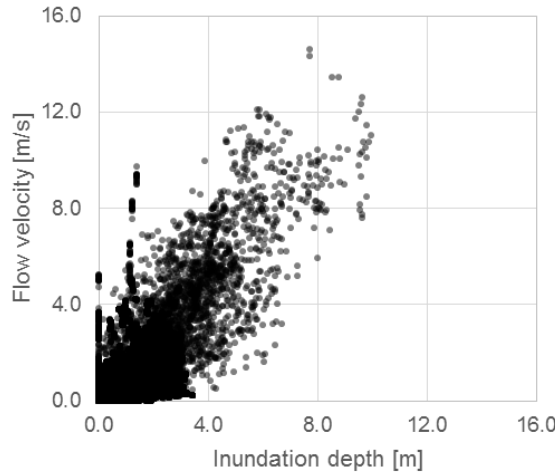


Fig. 3.26 Scatter plot depicting inundation depths and flow velocities simulated by a 2D model applied to the dam-break problem.

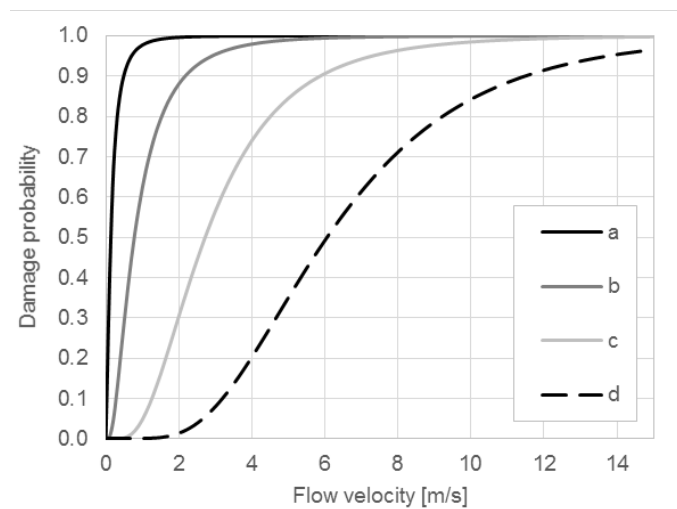


Fig. 3.27 Fragility curves admitted for road infrastructure.

Table 3.3 Parameters of the log-normal fragility curves admitted for road infrastructure.

Damage state	Location parameter (μ)	Shape parameter (σ)
a	-2	1
b	-0.25	0.8
c	-1	0.6
d	1.8	0.5

3.2.8 Flood routing

Outflow hydrograph estimation

Once a breach is opened in the embankment dam, either following an overtopping event or by alternative means, it starts to develop. This development is highly variable and is believed to depend on several parameters such as reservoir bathymetry, dam geometry, tailwater channel geometry, embankment materials, and initial condition of the breach (e.g. Wahl, 2004). Even physically based models, such as NWS-BREACH (Fread, 1988), are sensitive to initial location and morphology of the breach, being highly sensitive to analysts' assumptions.

Today, breach development and outflow hydrograph estimations can be achieved with physical models (Volz, 2013), conceptual models (Peter et al., 2015), or regression equations (e.g. Froehlich, 2008). Here, the breach parameters and evolution were obtained resorting to the latter publication, which presents a convenient way of including the phenomena in the GenMR simulations. The proposed regression equations can be used to estimate average breach width, breach formation time, and breach progression. Furthermore, the proposed regression equations are associated with the respective uncertainty, which is naturally interesting to risk assessment endeavours. As input data, the basic geometry of the embankment, the volume of the reservoir, the final height of the breach, and information on whether the breach was initiated by overtopping or not are required.

With this data, a simple model accounting for the reservoir's mass balance and equations for discharge over broad-crested trapezoidal weirs could be employed in order to estimate outflow hydrographs.

It should be highlighted that the current tools for outflow hydrograph estimation are quite uncertain. In order to fully capture this uncertainty, Peter et al. (2015) argue that the problem should be regarded through a probabilistic perspective and that a conceptual model (e.g. BASEBreach) can be used in order to obtain the probability distribution of possible outflows.

For concrete dams, the failure is usually assumed not to be progressive. In order to compute dam-break outflows from these structures one can resort to the Ritter equation (which is an analytical solution to an idealized problem) alternative simplified methods (e.g. Pilotti et al. 2010), or physically based numerical models, for example based on smoothed-particle hydrodynamics (Crespo et al., 2008). It should be taken into account, however, that physically based numerical models, either applied to embankment or concrete dams, will not be easily integrated in a Monte Carlo approach such as GenMR due to heavy computational demands.

Flood routing model

The dam-break wave propagation in the area downstream of the dam was modelled using a coupled 1D/2D numerical model: BASEMENT (Vetsch et al. 2005). The coupled numerical model allows for a relatively fast computation in narrow valley areas where buildings are not

significantly present, and invests resources on a more detailed reproduction of urban, relatively flat, and flow direction alteration areas.

The basic data used for setting up the model was the swissALTI3D Digital Elevation Map (DEM), made available by the Swiss Federal Office of Topography. It is a DEM with a pixel size of 2x2 m, with reported average error of ± 0.5 m below 2000 m.a.s.l. and between ± 1 and ± 3 m above that mark. Infrastructure, structures, and land use information was retrieved from the VECTOR25 dataset, also made available by the Swiss Federal Office of Topography.

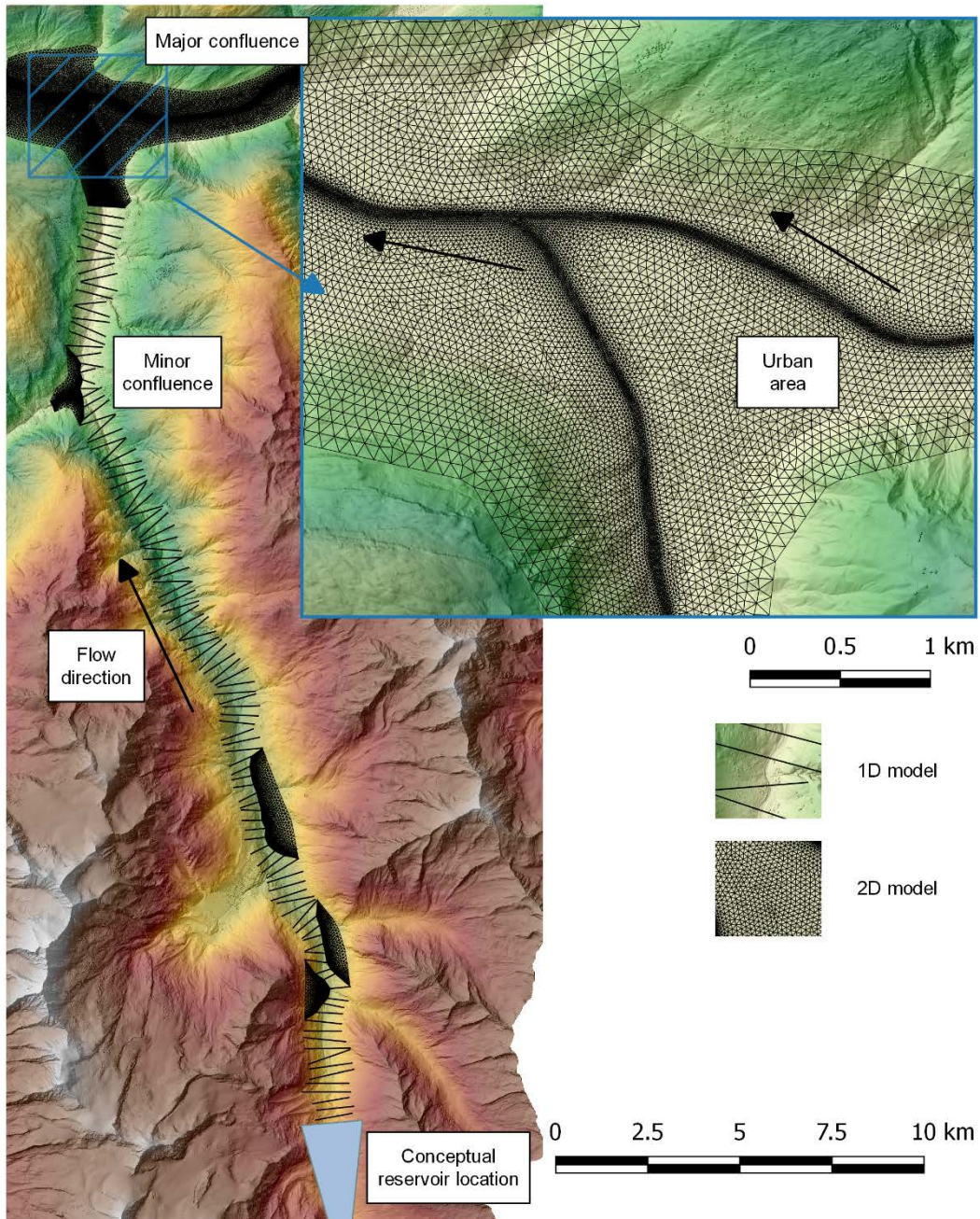


Fig. 3.28 Illustration of the area analysed downstream of the dam and depiction of the numerical grid and computational sections of the coupled hydraulic BASEMENT model.

These resources were used to model a selected Alpine valley, including confluences and urbanized areas, covering a length of over 30 km downstream of the conceptual dam (Fig. 3.28).

Terrain roughness was modelled resorting to the land use layer of VECTOR25 and Strickler coefficients indicated in literature for each type of terrain.

Because the region covered by the model is large, there were limitations on the number of 2D mesh elements dictated by computational concerns. While a fine grid was maintained at the river beds, it was not practical to use a sufficiently detailed grid between edifications (Fig. 3.29).

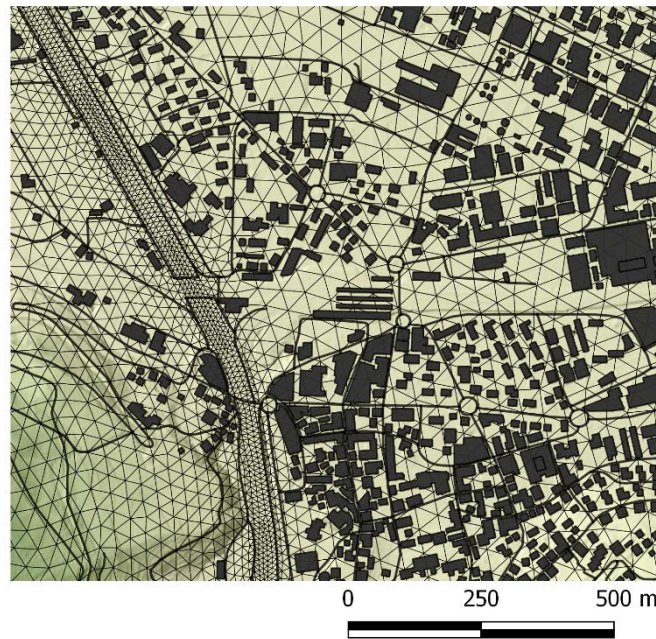


Fig. 3.29 Comparison of computational mesh and building sizes.

In order to account for obstacles to the flow posed by buildings in spite of the relatively coarse computational grid, a corrected roughness coefficient, \hat{K} , was employed in urban areas. Eq. 3.7 was used to that end:

$$\hat{K} = K(1 - A_b)(1 - P_b^\alpha) \quad (3.7)$$

With K being the Strickler coefficient, A_b the proportion of mesh element area occupied by buildings, P_b the proportion of mesh element area in contact with a building wall (assessed at a discretization of 2 m), and α a constant assumed equal to 2.

Based on the regression equations for breach formation cited in the previous subsection, 21 distinct hydrographs were produced by varying initial reservoir volume conditions and the breach formation time Fig. 3.30. Subsequently, each of the hydrographs in the set were routed using the coupled numerical model.

Simulated time series for inundation depth and flow velocity were recorded for each case, with dam-break wave arrival times also derived.

Illustrative results of the numerical simulation for a dam-break wave simulated following an overtopping and using average breach parameters are shown in Fig. 3.31 and in Fig. 3.32 providing inundation depths and flow velocity vectors in a densely urbanized area downstream of the dam at different time intervals from the start of the breach formation.

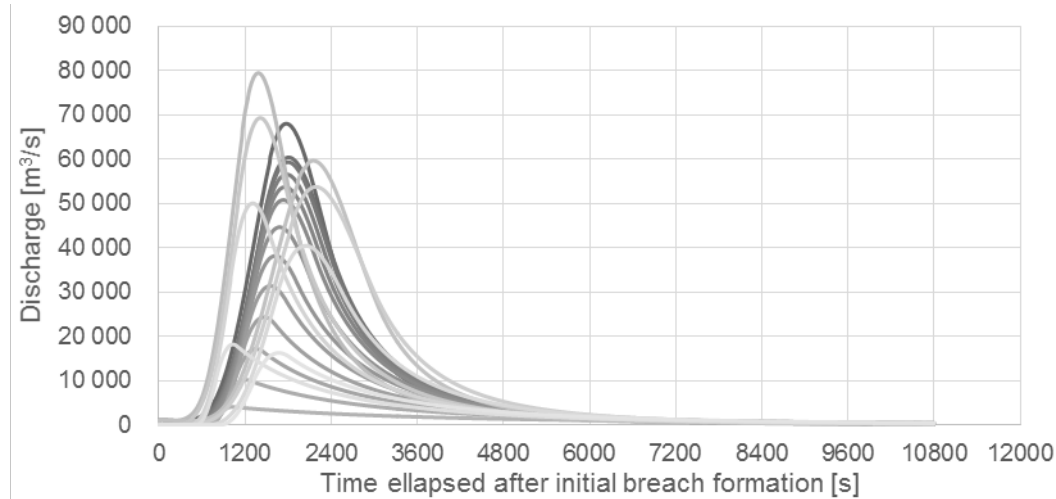


Fig. 3.30 Outflow hydrograph estimates used for hydraulic simulation.

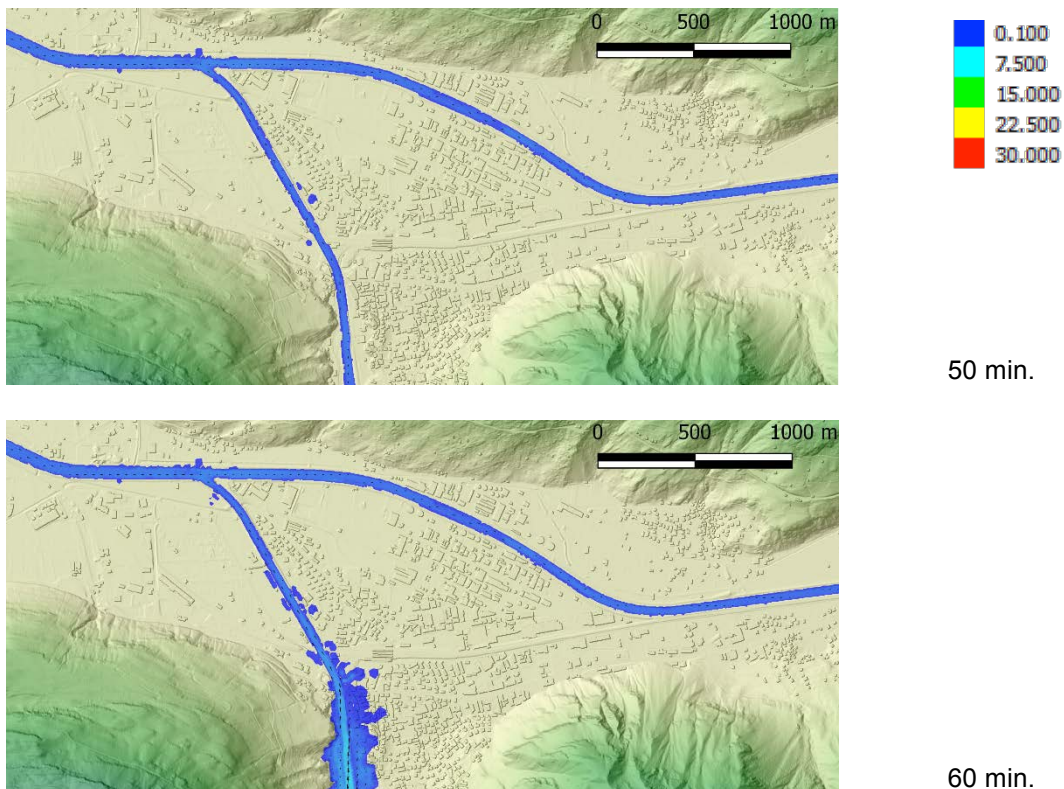


Fig. 3.31 Illustration of numerical simulation results of a dam-break wave simulated following an overtopping and using average breach parameters. Colours represent inundation depth (m) and arrows flow velocity.

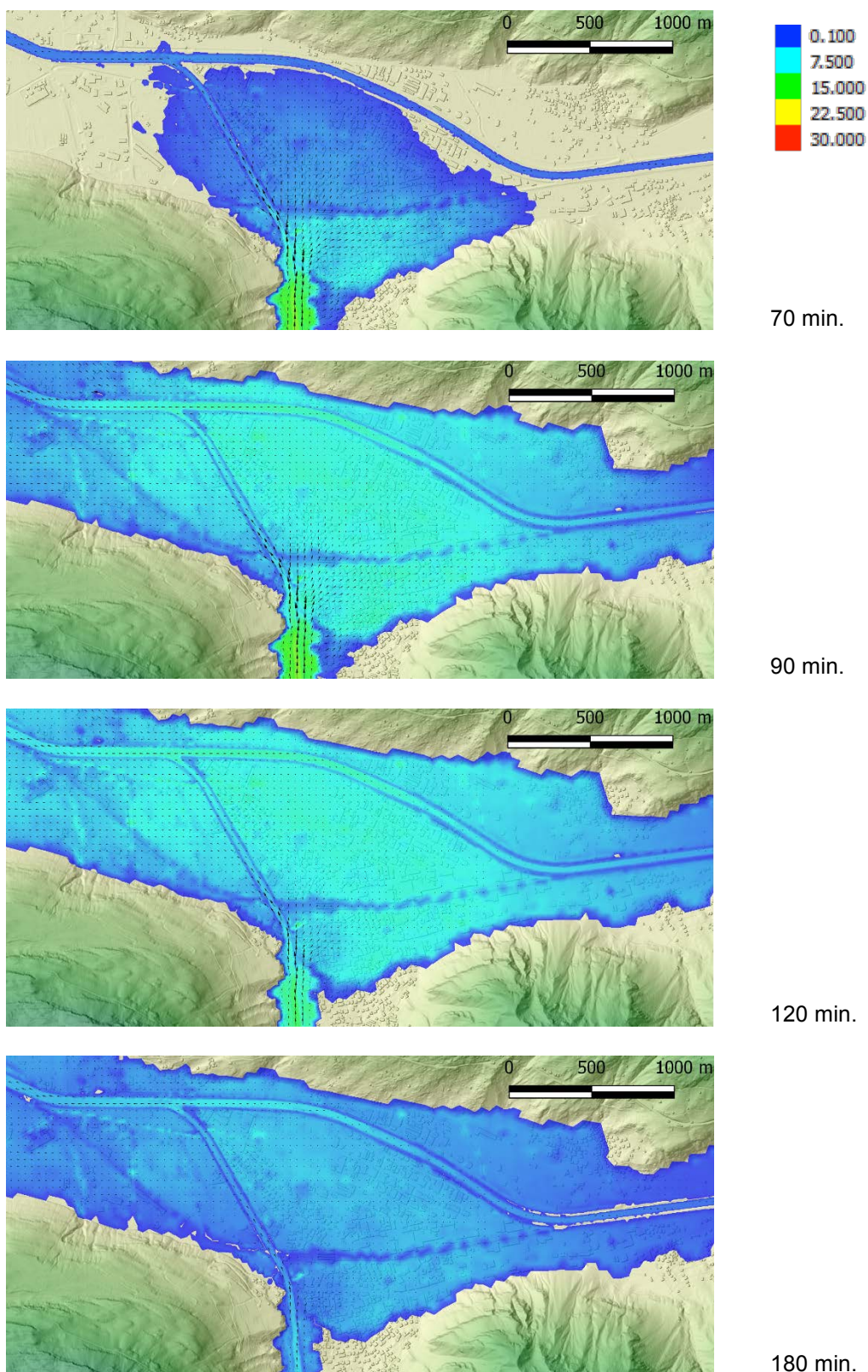


Fig. 3.32 Illustration of numerical simulation results of a dam-break wave simulated following an overtopping and using average breach parameters. Colours represent inundation depth (m) and arrows flow velocity.

Regression of inundation parameters

Similarly to numerical modelling of the hydrograph outflow, flood routing models – particularly 2D – are not practically included with a Monte Carlo method such as GenMR. Unlike breach formation, however, flood routing is not easily reproduced by simplified models. As a means to obtain inundation parameters corresponding to arbitrary dam-break hydrographs, it is proposed that a multiple non-linear regression model is adopted.

In order to achieve this, the set of 21 routed dam-break hydrographs (Fig. 3.30) was characterized by means of three variables: peak discharge (Q_p), slope of the ascending hydrograph (θ_a), calculated between the instant when the outflow equals $0.2Q_p$ and the peak, and the slope of the descending hydrograph (θ_d), computed between the peak and the instant when the outflow returns decreases to values below $0.2Q_p$.

Over the potentially inundated area, the surface is covered by tiles with any desired resolution. In this case, the tile shape was set to hexagonal, with a tile height of 200 m (Fig. 3.33).

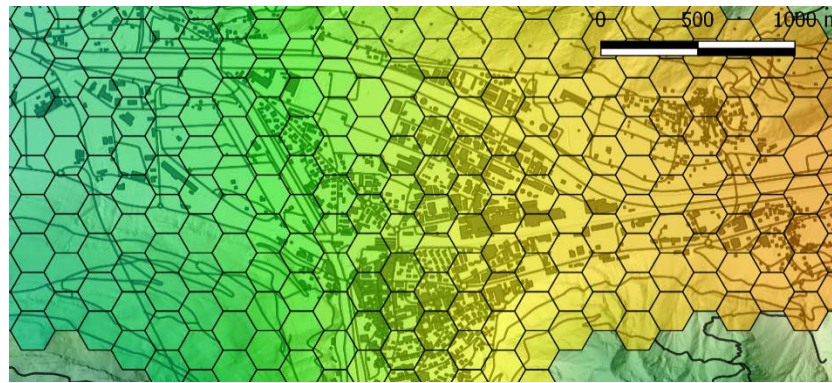


Fig. 3.33 Detail of the tile coverage of the potentially inundated area.

From the 21 time series, maximum inundation depths, maximum flow velocities, and flood arrival times were averaged within each tile. After this step, the regression problem can be framed according to Eq. 3.8):

$$\pi^i = f(Q_p^i, \theta_a^i, \theta_d^i | w^i) \quad (3.8)$$

Where i represents a given tile, $f(\cdot)$ is the regression model, Q_p^i , θ_a^i e θ_d^i are the parameters that characterize the outflow hydrograph, w^i stands for a vector of regression parameters, and π^i is the inundation parameter to be estimated.

For each tile and inundation parameter a regression is fitted based on the number of numerically simulated time series. In this case, a Support-Vector Regression (SVR) model (Drucker et al., 1996) was employed using a non-linear Gaussian kernel. Other choices of regression model could, however, be made. The description of SVR is considered well

beyond this document. For reference, SVR is related to the earlier support-vector machines (Cortes & Vapnik, 1995) and detailed mathematical descriptions of it can be found in numerous publications (e.g. Haykin, 1994).

SVR consists of a linear regression performed in a hypercube that is spanned by the application of the chosen kernel to every pair of fitting points. The SVR model fits automatically a linear hyperplane to the points projected in the hypercube, with non-linearity achieved when the regression hyperplane is projected in the original problem domain. The optimal hyperplane is, however, subject to the choice of three hyper-parameters which is paramount to define.

They are the SVR's capacity, controlling the regularization applied to the regression, the kernel width, affecting the sharpness of the response, and the loss function's insensitive band half-width, related to the inclusion of well-reproduced points in the final solution. While understanding of the effects of hyper-parameters is important, it can be largely mostly overlooked in the scope of an exploratory application such as the present. As such, hyper-parameters were optimized resorting to a cross-validation procedure and kept equal for all tiles.

A view of average errors along the hyper-parameter space for inundation depths is shown in Fig. 3.34. Examples of inundation depths estimated through the regression models fitted for randomly selected tiles are shown in Fig. 3.35.

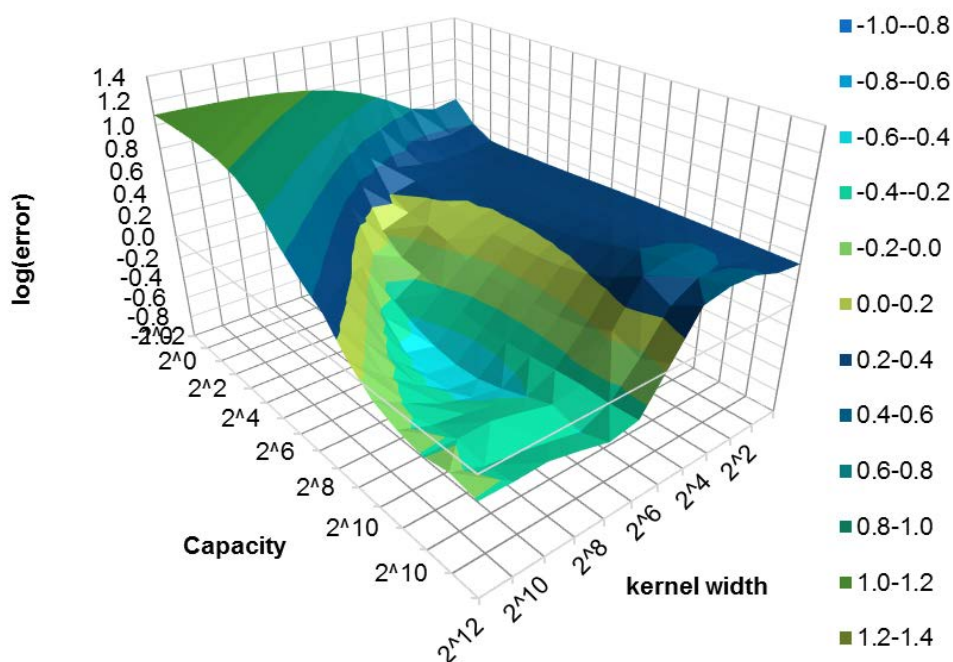


Fig. 3.34 Average error surface for the regression of inundation depth as a function of capacity and kernel width.

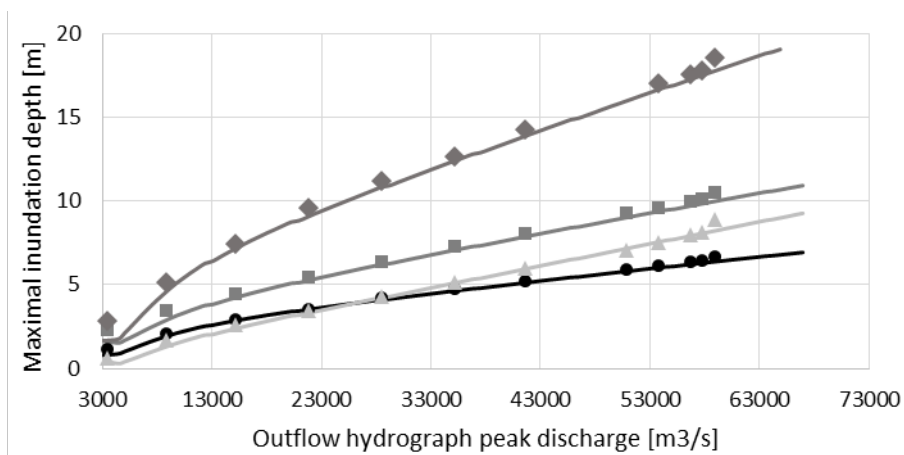


Fig. 3.35 Examples of inundation depths estimated through the regression models fitted for several tiles. Points were numerically simulated. Lines correspond to interpolated values.

3.2.9 Risk model

Likelihood of uncontrolled reservoir release

The GenMR model was employed, sampling over 5 000 000 years of reservoir operations, in order to characterize the dam-reservoir system, including hazard interactions (Matos et al., 2015). Results are synthesized in Table 3.4. From these and extended results, a disaggregation of the main hazards and elements intervening in the main time-lines leading to failure is possible.

In the case of the conceptual large alpine dam under study, the return period of failures was estimated to be slightly over 90 000 years, which agrees with what would be expected of failure rates for large embankment dams. This figure, while giving some reassurance that the proposed methodology does not stray away from historical observation is, however, debatable due to 1) the conceptual nature of the studied system and 2) the uncertainty associated the distinct phases of the methodology.

The 5 000 000 years analysed by the GenMR applications are, put into perspective, probably not enough to attain a stable state of the Monte Carlo Sampling procedure. This is due to the fact that dam failure events are so rare, that even in such a large number of repetitions only a little over 50 were simulated. Of course, this is likely to be insufficient to fully characterize the system's risk. Ways of obtaining a better insight on the nature of the tail of the loss distribution may be increasing the number of years analysed, reducing the number of hazards and elements considered and, possibly, focusing on years in which a rare primary hazards take place (this latter approach entails some risk of biasing the estimate, but is probably also very useful to reduce its variance).

Table 3.4 Summary results of the application of the GenMR framework to the dam-reservoir system. Results rounded from Matos et al. (2015).

Event	Simulated return period
Spillage	1600
Level excess	21900
Marginale overtopping	227300
Spillway severe damage	9700
Dam mild damage	6100
Dam tolerable damage	37300
Dam severe damage	36500
Dam critical damage	64900
Drawdown	9500
Failure	92600

Despite the admitted limitations, the results give information beyond an estimate of the return period of failures. For example, for the analysed conceptual dam nearly all failures followed an internal erosion event, with earthquakes being the final cause of breach in fewer occasions. Floods, on the contrary, had very reduced impacts on the system.

Consequence assessment

The consequence assessment is accomplished by combining information on regressed inundation parameters and fragility curves at each tile.

Below, Fig. 3.37 shows the consequence assessment for buildings under a specific dam-break event. Damages were derived from the application of multiple fragility curves (Fig. 3.25). The same process was carried out for the road infrastructure (Fig. 3.37).

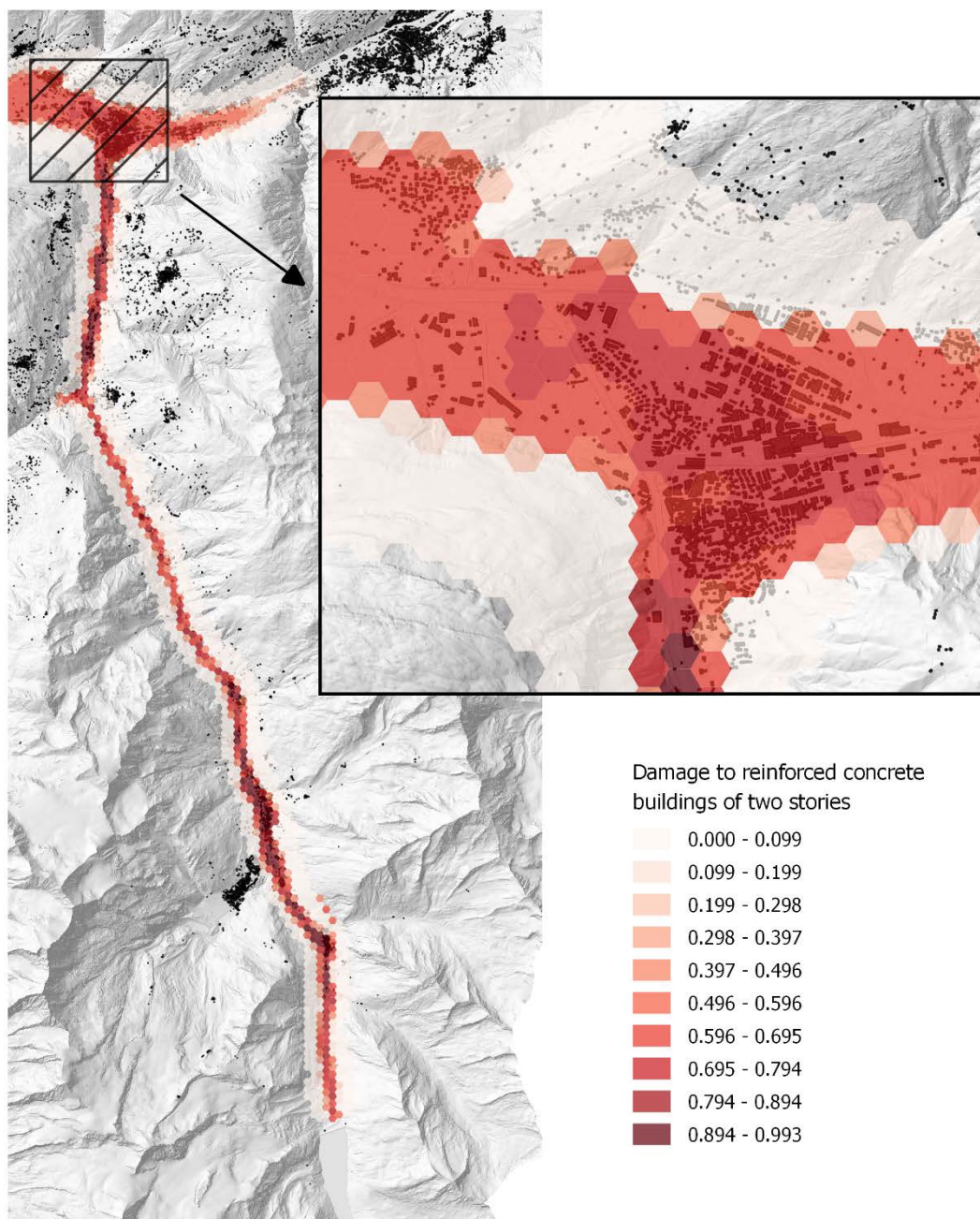


Fig. 3.36 Map of damages to reinforced concrete buildings of two stories corresponding to a specific dam-break event.

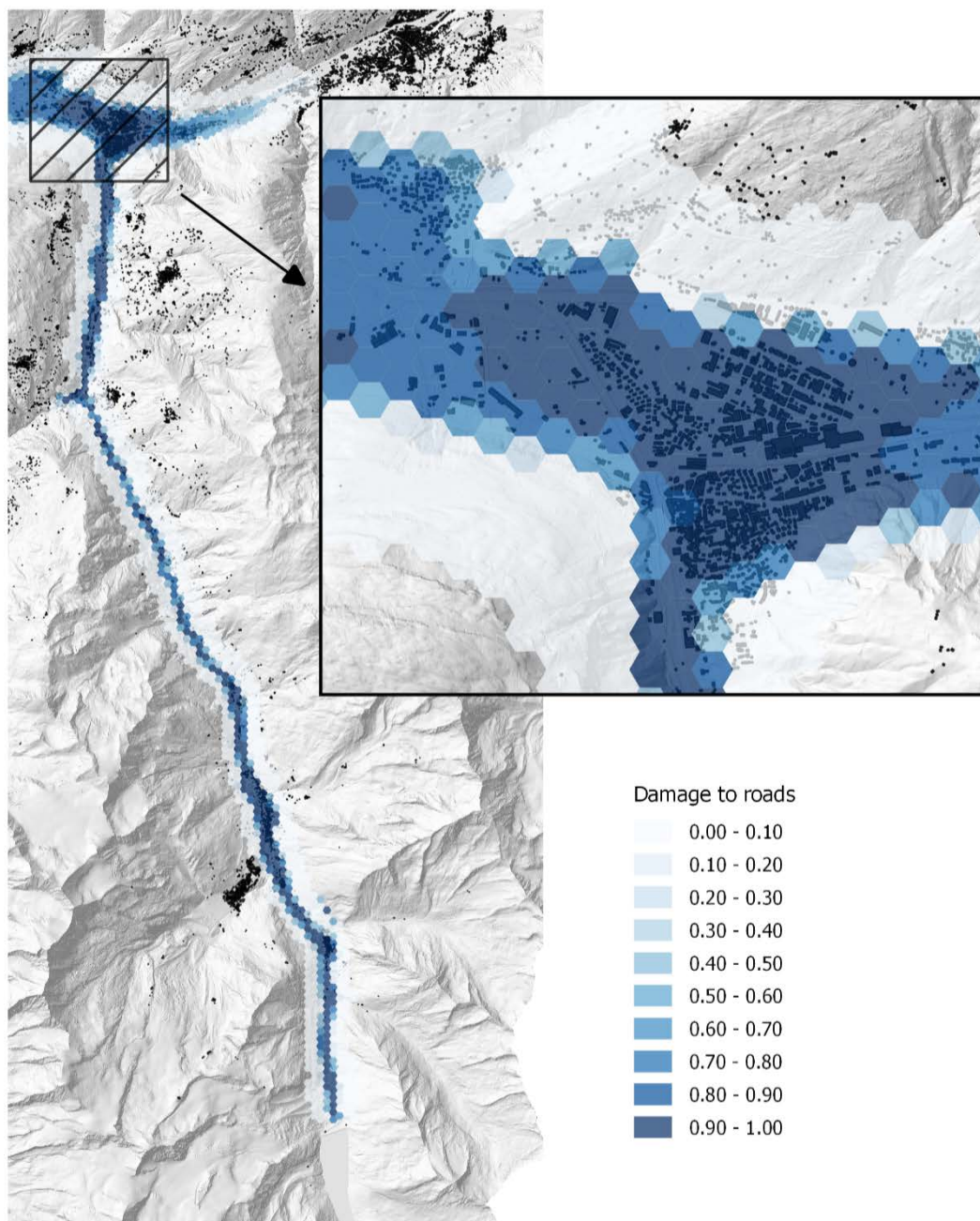


Fig. 3.37 Map of damages road infrastructure corresponding to a specific dam-break event.

Risk

In order to obtain risk, not in terms of monetary losses, but in terms of damage to structures and infrastructure, damage assessments for all simulated dam failures are combined and multiplied by the probability of each event. Results are, again, presented in relation to reinforced concrete buildings of two stories (Fig. 3.38) and roads (Fig. 3.39)

It should be noted that these maps present a way to compute the risk associated with infrastructures of a certain type within the studied area. In that sense, infrastructures of each

type need not be present in a given tile for an expected value to be given. In order to obtain actual losses, one should additionally overlay these maps with information about land occupation and property values.

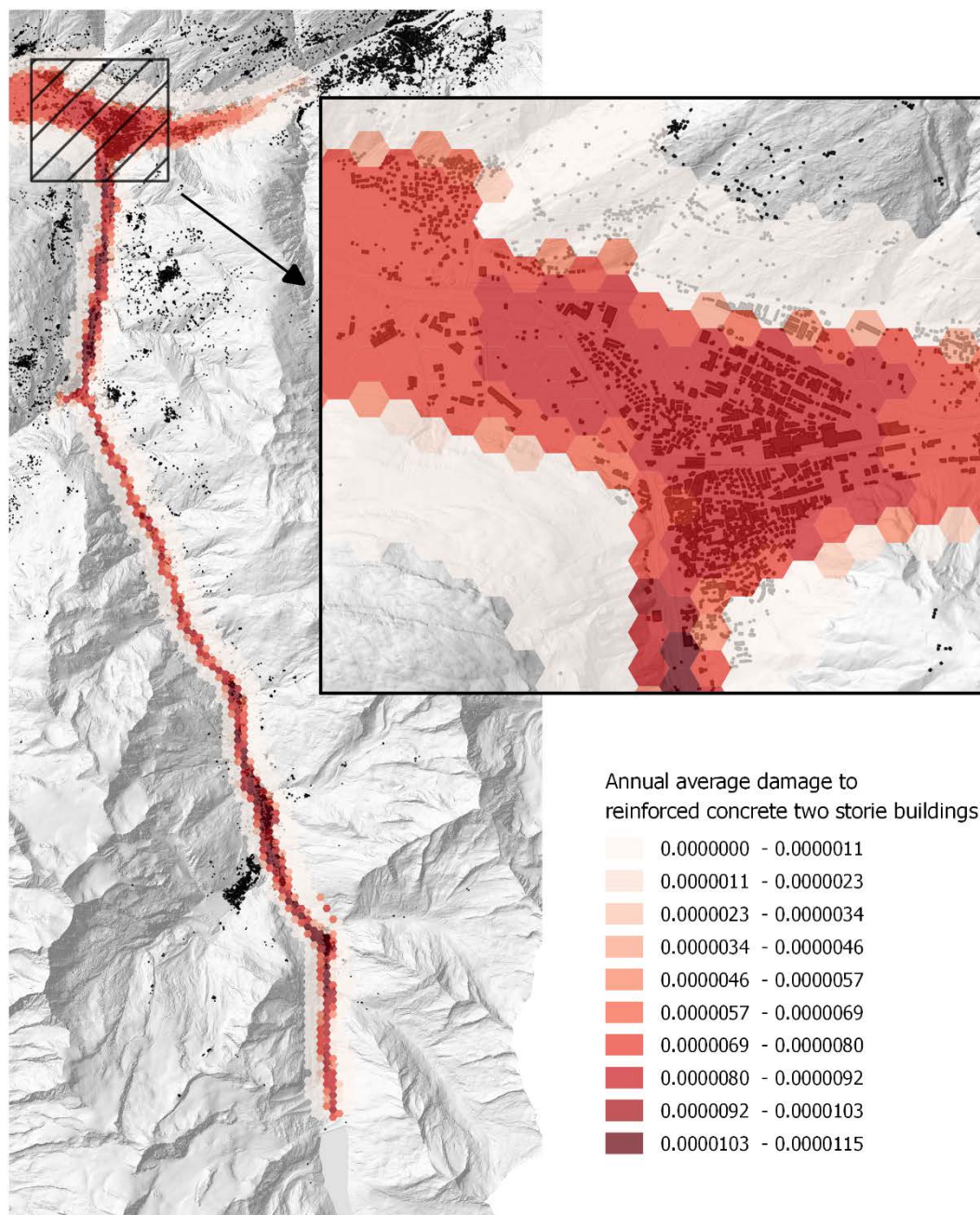


Fig. 3.38 Map of annual expected damage to reinforced concrete buildings of two stories.

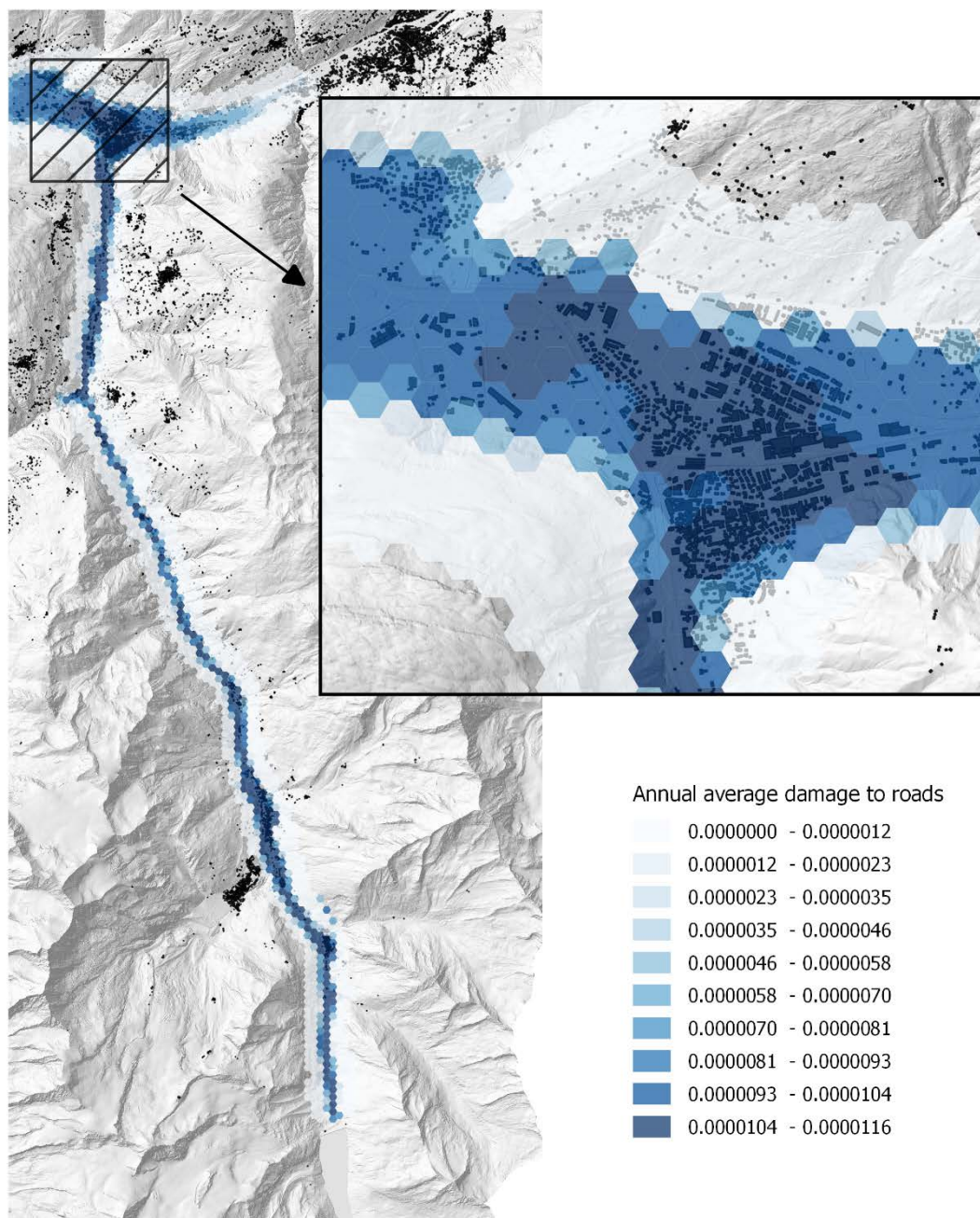


Fig. 3.39 Map of annual expected damage to road infrastructure.

3.2.10 Uncertainties

The analysis proposed for the overall assessment of dam risks is ambitious, going in some ways further than established methodologies such as Failure Modes and Effects Analysis (FEMA), Event Tree Analysis (ETA), and Fault Tree Analysis (FTA).

Every practical risk assessment is necessarily bound to a number of given hazards, as well as elements, damage and limit states. In dam engineering this is particularly evident. Because dams are built to be safe – never to fail – designers and regulators are chiefly invested in testing limit scenarios and pay only moderate attention to risk assessment. These limit scenarios are tested in ever growing detail, through finite element numerical models for structural response, computational fluid dynamics and smoothed-particle hydrodynamics, targeting hydraulic phenomena, or ever more complex extreme event probability estimation techniques, in what concerns hydrology.

These advancements have been remarkable achievements and, today, the engineering community understands to a great level of detail the main processes at work around dams. In a sense, however, while such progresses are being made in the direction of characterizing isolated phenomena better, far fewer advancements have been made towards understanding combinations of these phenomena.

Historically, many dam-related disasters were not the consequence of extreme events alone, but also – and sometimes only – the result of a combination of unforeseen or apparently inconsequential happenings. If only in an attempt to better comprehend such combinations, the development of a methodology capable (and conceived with the purpose) of evaluating hazard interactions is a worthwhile endeavour.

This contribution represents but a small step in that direction and has several shortcomings worth addressing in the future.

Regarding hazards, it did not account for possibilities such as mass slides or icing, which are worth inspecting, and it overlooked most human, control, and mechanical interactions. Also, it did not incorporate a measure of uncertainty into hazards intensity estimates.

The dam-reservoir system was modelled with a very limited number of elements and, at that, with little detail. In order to improve results, some minor elements should also be included in the analysis and vulnerability functions could be derived from, for example, finite element models.

In order to perform the simulation of the reservoir in time, several important assumptions were made. Firstly, “base” inflows were the same for all the tested years. This should not be so. Also, reservoir operations were scheduled based on a very simple procedure that is likely to exhibit a more conservative approach than that of real dam operators due, among other things, to fluctuating prices of energy.

In the event of a failure, dam-breach development was characterized through a simple regression technique which is known to entail a fair degree of uncertainty. Furthermore, the outflows computed on the basis of the estimated breach development were done by resorting to simple weir equations (adequate to much smaller scales) and assuming regular geometry. Some relevant errors due to these simplifications are to be expected.

The flow propagation is affected by uncertainty on several accounts. First, the data that is fed to the hydraulic model is imperfect, particularly in what concerns roughness coefficients, which should be reviewed. Secondly, for practical reasons the model’s mesh is likely too

coarse to reproduce well the effect of buildings and other obstacles on the flow. Thirdly, real dam-break waves erode the soil, tear trees off the ground, wash away buildings and cars. In their wake, valley morphology can be significantly changed. By ignoring these processes during the flow propagation, the analysis incurs in a further departure from reality.

Because it is not practical to numerically simulate the flood's propagation downstream for every outflowing hydrograph, a non-linear regression model was put forward as a means to obtain flood intensity estimates distributed in tiles. Yet again, the needed simplifications lead to some deviations. In this case due to the loss in resolution, now reduced to tile size, and due to the unavoidable errors in the regression.

Finally, in the application of the fragility curves for different kinds of structure, infrastructure, or loss of life, two sources of uncertainty can be highlighted: the possible inadequacy of the curves themselves, and the fact that the analysis is, for the moment, overlooking hazard interactions that might play a role in the downstream areas. For example, a flood wave following a major earthquake can drown people caught in collapsed buildings or routes to higher ground might be blocked.

As described, there are ample sources of uncertainty that need to be addressed as the goal of an overall risk assessment estimate for large dams is to be pursued. The GenMR framework is suitable to deal with these uncertainties, but it is mostly through investment in the characterization of vulnerability, functionality, and interactions of system elements – particularly at the dam level – that more confidence can be placed in the framework's results.

4 CI-B3 - Port infrastructures of Thessaloniki, Greece

4.1 INTRODUCTION

Tsunamis are long-period water waves that can be triggered by undersea shallow-focus earthquakes, underwater or aerial landslides or volcanic eruptions. As observed from historical tsunamis, the vast majority of them are induced by a seismic event. Occurrence of tsunamis can cause tremendous (direct and indirect) losses in terms of human lives and infrastructure damage as seen recently in Japan (2011), Chile (2010) and in the coastlines of the Indian Ocean (2004) (e.g. Suppasriet al., 2013; Mas et al., 2012; Koshimura et al., 2009). In particular for seaport structures, experiences gained from recent tsunamis have dramatically demonstrated their vulnerability increasing the research activities throughout the world to establish new methodologies and technical recommendations for proper design and assessment of seaport structures (Bartolomeiet al., 2008).

Regarding the damage caused to building structures, the damage extent due to tsunamis presents a large dispersion from slight non-structural damage to total collapse or even washing away of structures based on the building characteristics and the tsunami's parameters. Taking into account that tsunamis are a typical example of "low probability – high consequence" events, the prediction of the damage is often subject to a high level of uncertainty. Knowledge of the tsunami-genic sources with their probability of occurrence, size and their probable impact or consequences as well as the structure's characteristics are therefore essential to reduce the great deal of uncertainty associated with the tsunami vulnerability modeling. Generally, the vulnerability of buildings to tsunamis may depend on several factors. Among them, some of the most pronounced are the triggering mechanism (earthquake, volcanic eruption, submerged or aerial landslide), the tsunami wave height and wave period and the corresponding hazard, the coastal topography and the roughness of the coastal inland and the specific strength and stiffness characteristics of the exposed elements.

Tsunami risk assessment is a relatively new and developing discipline, which obtained an increased interest from the scientific community due to the occurrence of recent tsunami events with severe consequences (e.g. the Indian Ocean tsunami on 2004, the Java tsunami in 2006, the Solomon Islands tsunami in 2007, the South Pacific tsunami on 2009, the Chilean Tsunami in Dichato on 2010, and the 2011 Great East Japan tsunami) as well as the great potential for further tsunami events. It is expected that future tsunamis can have a higher impact due to the increasing number of people, buildings and infrastructure that are being exposed to natural hazards as the pressures for urban development extend into areas of higher risk (Jelínek & Krausmann, 2008). However, only a limited number of tools to estimate the potential impacts of tsunami are available until now.

Some of the very first approaches for tsunami risk assessment were developed before the 2004 Indian Ocean tsunami (Shuto, 1994; Papadopoulos & Imamura, 2001; Hatori, 1984). Since the 2004 tsunami, the number of studies has increased significantly. Dalrymple & Kriebe (2005); Stansfield (2005); Ghobarah et al. (2006) focused their studies on qualitative damage analysis, (Rossetto et al., 2007) and Kaplan et al. (2009) categorised building damage. Following the advances in earthquake risk analysis, other existing approaches consist in assessing the tsunami vulnerability quantitatively using damage or fragility functions. Tsunami fragility functions provide for every element at risk (i.e. building, infrastructure) the conditional probability for the element of reaching or exceeding a given damage state, for a range of values of the tsunami intensity, taking into account various sources of uncertainty (both aleatory and epistemic). Tsunami fragility functions define appropriate statistical relationships between damage probability and tsunami flow characteristics inland such as inundation depth, current velocity and hydrodynamic force (i.e., the intensity measures). The damage is commonly classified using field survey data or visual interpretation of high-resolution satellite images while the tsunami flow characteristics are obtained by a field survey (for the inundation depth) and by the numerical simulation in a very fine grid (for current velocity and hydrodynamic force). In the following, a brief review of the available procedures for assessing the vulnerability of buildings to tsunamis through fragility or damage functions is presented.

Peiris (2006) developed vulnerability functions for unreinforced masonry residential properties using the data available for the coastal areas of Sri Lanka. Dias et al. (2009) carried out probabilistic modelling to obtain a synthetic fragility curve for the case of single storey masonry buildings. Koshimura et al. (2009) developed tsunami fragility curves using numerical modelling of tsunami inundation and GIS analysis of post-tsunami survey data of the 2004 Sumatra–Andaman earthquake tsunami disaster, obtained from Banda Aceh, Indonesia. The fragility functions are expressed as the damage probabilities of structures or death ratio with regard to the hydrodynamic features of tsunami inundation flow, such as inundation depth, current velocity and hydrodynamic force. Leone et al. (2011) implemented an original method of damage spatial and quantitative analysis on the building damages based on field surveys of the 2004 Indian Ocean tsunami, photo interpretations and GIS. This analysis was complemented by fragility curves that give the statistical relationships between mean damage intensities and wave heights. (Reese et al., 2011) developed empirical tsunami fragility functions from observational and quantitative data on building damage obtained from the 2009 South Pacific tsunami, and the tsunami demand. (Valencia et al., 2011) developed tsunami damage functions for different typologies of buildings along European-Mediterranean coasts, based on data collected by several authors in Banda Aceh (Indonesia) after the 2004 Indian Ocean tsunami. (Suppasri et al., 2011) developed tsunami fragility curves from the tsunami features (inundation depth, current velocity, and hydrodynamic force) for different types of building materials, using visual inspection of high-resolution satellite images of damaged buildings, based on the remaining roofs, taken before and after tsunami events, as well as a tsunami inundation numerical model of the 2004 Indian Ocean tsunami in Thailand. (Mas et al., 2012) developed fragility curves, in terms of inundation depth, to estimate the structural fragility against tsunami hazard in the town of Dichato. They used surveyed data of inundation depth and visual inspection of satellite images of the 2010 Chilean Tsunami in Dichato to classify the damage to housing and presented a practical method suitable when there are limitations on available data for numerical simulation or damage evaluation from surveys. (Suppasri et al., 2013) developed empirical tsunami fragility functions using a set of building damage data of the 2011 Great

East Japan tsunami, with details on damage level, structural material, number of stories per building and location (town). Finally, (Nanayakkara & Dias, 2013) compared fragility curves from different researchers, in order to explore similarities, and discriminated fragility curves on the basis of different building types.

It's worth noting that, as shown from the above, all existing fragility (or damage) functions for buildings and infrastructures exposed to tsunami hazard are principally based on empirical data (hazard-damage relationships from previous tsunami events) and/or expert judgment, and as such there are limitations in their general application as they are highly specific to a particular seismo-tectonic, geotechnical and built environment. Analytical fragility curves for tsunami hazard for various elements at risk that could be used for general purposes are not yet available in the scientific literature, at least to our present knowledge and review.

To bridge the gap, this study aims at developing analytical fragility functions for Thessaloniki's port critical buildings and infrastructures, i.e. low-code RC buildings, warehouses and container cranes, under tsunami forces. The Port of Thessaloniki is one of the largest Greek seaports and one of the largest ports in the Aegean Sea basin. Considering that, it is really important to improve our ability to estimate the future impacts of tsunamis to port infrastructures, along with the resulting supply-chain impacts. The proposed vulnerability assessment methodologies are based on nonlinear numerical computations and adequate statistical analysis. An extensive numerical parametric investigation is performed considering different combinations of statically applied tsunami loads based on (FEMA, 2008) recommendations for gradually increasing tsunami inundation depths. Structural limit states are defined in terms of threshold values of material strain based nonlinear static analyses (both seismic pushover and tsunami time history analyses). Fragility curves are finally derived as a function of inundation depth for the various building typologies and infrastructures considered. The model results are also compared in terms of fragility curves with field survey data from recent tsunami events (Suppasri et al., 2013). The proposed fragility functions could be used for quantifying the potential tsunami damage to buildings and infrastructures along European-Mediterranean coasts.

4.2 METHODOLOGY

The proposed methodology, largely inspired from earthquake risk analysis, is applicable for the vulnerability assessment of buildings subjected to tsunami forces. It is based on a comprehensive set of numerical computations and adequate statistical analysis. The framework of the proposed methodology is schematically illustrated in Fig. 4.1.

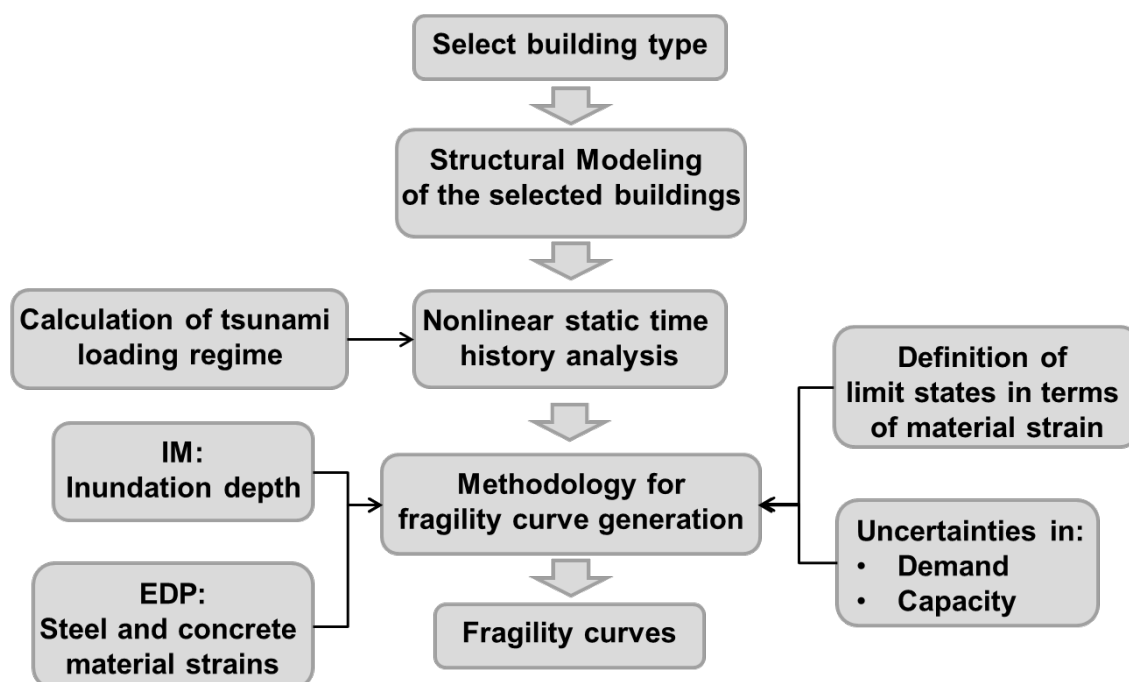


Fig. 4.1 Flowchart of the proposed methodology

Several building typologies (i.e. low-code RC buildings and warehouses) and a large modern container crane representative of Thessaloniki's port critical buildings and infrastructures, respectively, were considered to apply the proposed method (Section 4.3). The numerical analyses were conducted using the finite element code Seismostruct (SeismoSoft, 2015). Nonlinear constitutive models were used to simulate the behaviour of materials since cracking and irreversible deformations are normally expected to govern the building's response. The "fibre approach" is used to represent the cross-section behaviour, where each fibre is associated with a uniaxial stress-strain relationship. It should be noted that all models are fixed-base. It is also worth noting that in this phase of the study (single-risk assessment), far-source generated tsunami is considered, where the epicentre of the earthquake is assumed to be at a long distance from the structure and the structure has not sustained any initial damage due to ground shaking.

Tsunami loading was computed using the FEMA recommendations (FEMA, 2008). In particular, each structure was subjected to buoyant, hydrostatic and hydrodynamic forces combined with forces due to debris, all of which constitute tsunami load effects. A detailed description of the considered tsunami forces is provided in the following section. It is noted that the considered combination of tsunami forces differs for the various building typologies whereas the amplitude of the resultant force increases with increasing tsunami inundation depth. The computed forces are then directly applied as input static loads to an appropriate

nonlinear structural model for gradually increasing inundation depths. Afterwards, the structure's response in terms of material strain (i.e. the engineering demand parameter, EDP) for the different statically applied tsunami loads is estimated. It is noted that a local damage index, such as material strain, is better correlated with structural damage due to tsunami forces compared to a global damage index, as e.g. Macabuaget al. (2014).

Subsequently, appropriate limit damage states are defined in terms of threshold values of the material strain of the structure, based on nonlinear static analyses (both seismic pushover and tsunami time history analyses) for the various critical buildings and infrastructures of the port, engineering judgment and the available literature (e.g. (Crowley et al., 2004; Fotopoulou & Pitilakis, 2013a; Fotopoulou & Pitilakis, 2013b)). Four damage states are applicable in this study associated with none to slight, moderate, extensive and complete structural damage of the building (or the infrastructure).

The vulnerability is assessed through probabilistic fragility curves, which describe the probability of exceeding each limit state, considering various sources of uncertainty. In the probabilistic approach proposed herein, several uncertainties exist with respect to the structural capacity and the demand (in terms of material strain). A key point in the derivation of fragility curves is the selection of the intensity measure (IM) that adequately correlates with damage. According to FEMA (FEMA, 2008), it is noted that numerical predictions of flow velocities are less accurate than predictions of inundation depths, and the grid size for numerical simulations in the runup zone must be very fine in order to obtain sufficient accuracy in velocity predictions. In addition, most existing empirical fragility functions are derived in terms of inundation depth as it is the parameter most easily measured in the field. Based on the above, inundation depth is selected as an IM. For the development of fragility curves, an appropriate relationship between the numerically calculated material strain (i.e. the EDP) and the gradually increasing inundation depths (i.e. the IM) is established through nonlinear regression analysis. Lognormally distributed fragility curves are finally derived as a function of inundation depth for the different damage limit states for the various building typologies and infrastructures considered.

4.3 THESSALONIKI PORT INFRASTRUCTURES

The presence of a seaport represents a remarkable factor of development of a region or even a nation. The interruption of functionality of port structures can have severe direct and indirect effects on the economy and on the social and environmental growth of the broader area of interest, in our case the city of Thessaloniki, or even broader, the country of Greece. The Port of Thessaloniki is one of the largest Greek seaports and one of the largest ports in the Aegean Sea basin with a total annual traffic capacity of 16 million tonnes (7 million tonnes dry bulk and 9 million tonnes liquid bulk). As a free port, it also functions as a major gateway for the Balkan hinterland and south-eastern Europe. Its strategic geographical position increases its importance for the trade and the economy of the region, as it is a crucial point for supply chains, as well as a crucial node of transit of millions of travellers every year.

Critical buildings of Thessaloniki's port mainly consist of low- and pre- code RC buildings and warehouses. Most of them are low-rise (1-3 floors), such as the building of the central offices of the Port Authority, the building of Technical and Financial Services, etc., some are mid-rise (4-7 floors) buildings (e.g. PAEGA multistore warehouse) and there is one high-rise

building (silos). They are also categorised as dual and moment resisting frame (MRF) systems based on the existence or not of shear walls, respectively. The warehouses, which are basically industrial steel structures with or without unreinforced masonry infill walls, constitute a category of their own. The buildings of paramount importance for the operation of the port together with their main characteristics are listed in Table 4.1.

The SYNER-G (www.syner-g.eu) taxonomy is used to describe the different RC building typologies (e.g. Crowley et al., 2011). In particular, the studied RC buildings were classified according to their structural system (i.e. MRF, dual), their height (i.e. low-rise, mid-rise and high-rise), and the existence or not of infill walls (i.e. bare frames, infilled) as well as the seismic design level (i.e. the 1959 Greek seismic code corresponding to low level of seismic design). Based on these criteria, the main RC building typologies considered are summarised in Table 4.2. Fig. 4.2 and Fig.4.3 present floor plans and representative cross-sections respectively of the studied RC building typologies (Kappos et al., 2006). Regarding the warehouses, Fig.4.4 shows a typical warehouse of Thessaloniki port while Fig.4.5 and Fig.4.6 present a floor plan and a representative cross-section respectively of the studied warehouse provided by the Thessaloniki Port authorities and reproduced by AUTH.

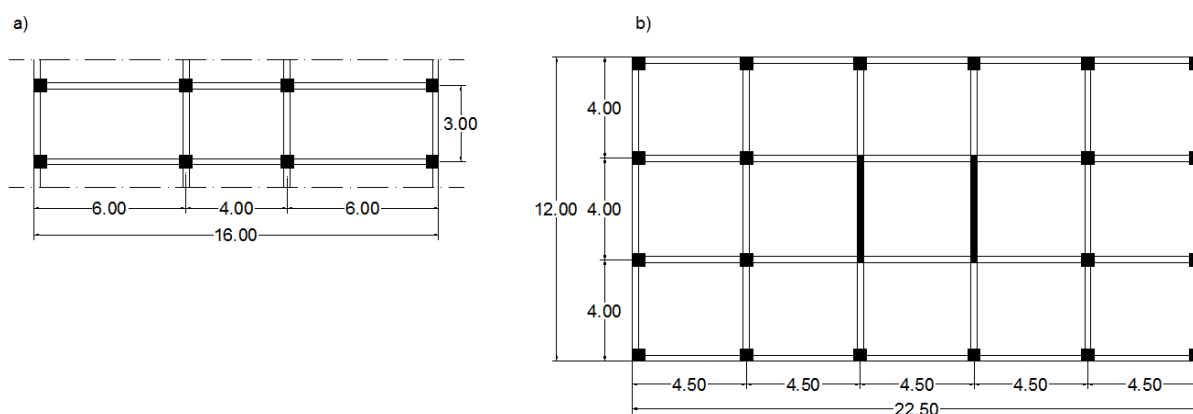
Container cranes constitute one of the most critical components to the functionality of Thessaloniki port. In this respect, a modern jumbo crane (J100) representative of container gantry cranes of Thessaloniki port (personal communication with the Thessaloniki's port authorities) (Fig.4.7) is also studied. The overall dimensions of the crane as well as the section definitions of the major structural elements illustrated in Fig.4.8 have been derived from the study of (Kosbab, 2010). The key structural and nonstructural elements are also labeled in Fig. 4.8 and defined in Table 4.3. The container crane is built using some combination of the following steel sections; built-up hollow boxes, tubes and built-up wide-flange shapes. The dimensions of the different shapes are defined in Fig.4.9. The hollow boxes utilize longitudinal rectangular stiffeners of length BS and thickness t_s ; thus, n_f (or n_w) indicate the number of longitudinal stiffeners equally spaced along the flange (or web) of a given box section. Dimensions for the referenced section definitions are presented in Table 4.3 (built-up hollow boxes), Table 4.5 (tubes) and Table 4.6 (built-up wide-flange shapes).

Table 4.1 Characteristics of Thessaloniki port buildings

Description	Construction year	Height (storey)	Typology	Material	Code
Central offices of the Port Authority	Initially in 1939 then again in 1946	2	Dual	RC	none
Technical & Financial Services	decade of 1975	3	Dual	RC	low
Kindergarden	1963	2	Dual	RC+bricks	-
Offices of the central Port Authority	before 1900	2	MRF	RC	none
Port Security Services	1960	2	MRF	RC	low
PAEGA Multistore Warehouse	1960	4	MRF	RC	low
Silos	decade of 1960	12	-	RC	low
Warehouse 1	1904 reconstr. 1997	1	-	Steel+masonry	-

Table 4.2 Typologies of Thessaloniki RC port buildings

Structural System	Height (number of stories)	Infills	Seismic design level
MRF	Low-rise (1-3)	with/without infills	Greek code '59 (Low code)
	Mid-rise (4-7)	with/without infills	Greek code '59 (Low code)
	High-rise (8+)	with/without infills	Greek code '59 (Low code)
Dual	Low-rise (1-3)	with/without infills	Greek code '59 (Low code)


Fig. 4.2 Plan view of the a) MRF and b) Dual RC buildings

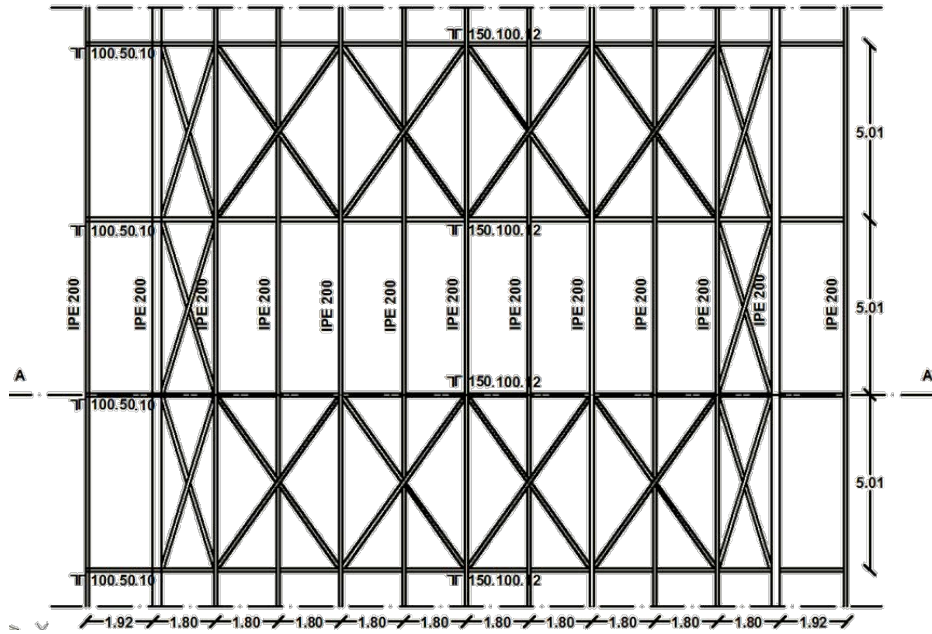


Fig.4.5 Plan view of the warehouse

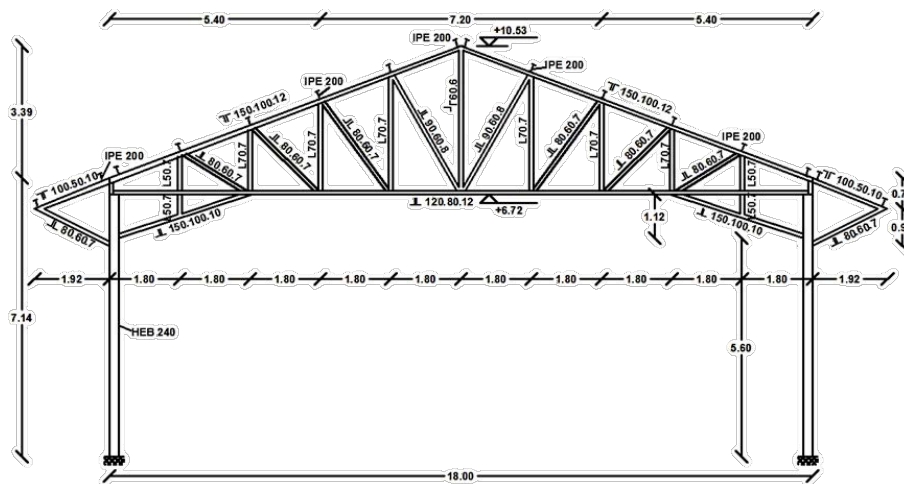


Fig.4.6 Cross-section of the warehouse

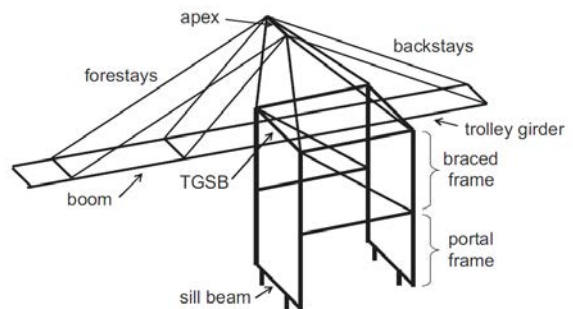


Fig.4.7a) Photo of a typical container crane of Thessaloniki Port and b) 3D schematic view of the analytical container crane model (Kosbab, 2010).

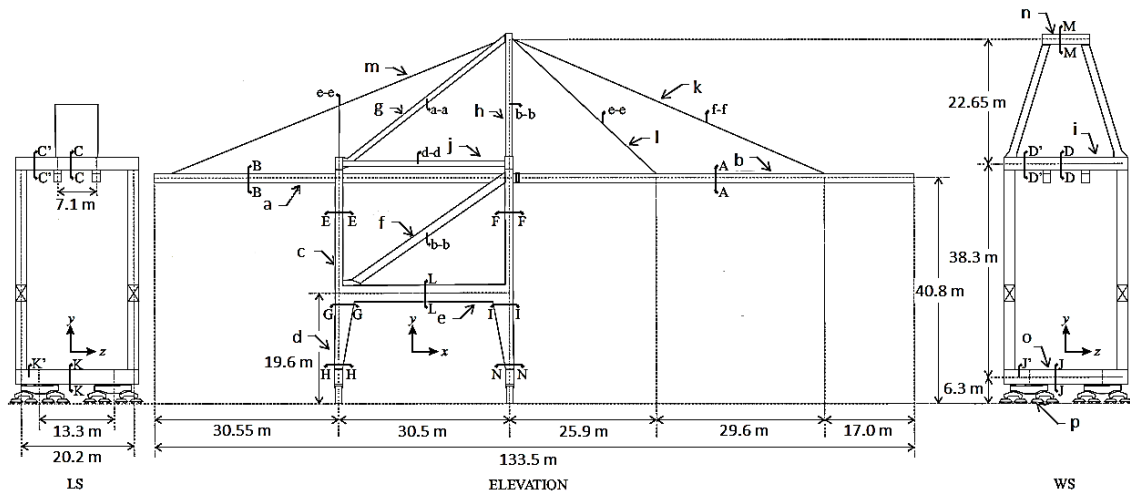


Fig.4.8 Overall dimensions and section assignments (defined in Table 4.3, Table 4.4) and Table 4.5) of the studied container crane (Kosbab, 2010).

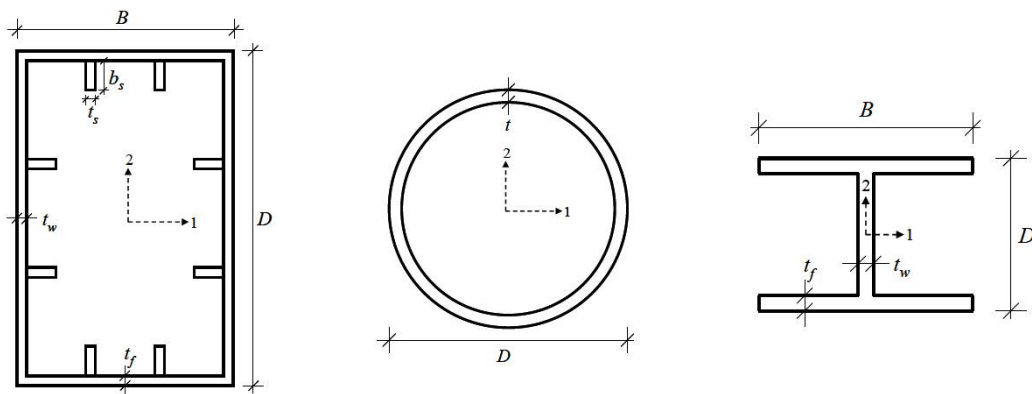


Fig.4.9 Cross-sections employed in the container crane and its dimensions (Kosbab, 2010).

Table 4.3 Terminology of labeled elements adopted in Fig.4.8 (Kosbab, 2010)

Section	Element
a	Trolley Girder
b	Boom
c	Upper Leg
d	Lower Leg
e	Portal Beam
f	Lower Diagonal
g	Upper Diagonal
h	A-Frame
i	Trolley Girder Support Beam (TGSB)
j	TGSB Tie
k	Outer Forestay
l	Inner Forestay
m	Backstay
n	Top Beam
o	Sill Beam
p	Balance Beam/Truck System

Table 4.4 Dimensions of J100 built-up hollow box sections(Kosbab, 2010).

Section	B (m)	t _f (m)	n _f	D (m)	t _w (m)	n _w
A-A	1.52	0.016	1	2.29	0.010	2
B-B	1.52	0.013	1	2.29	0.008	2
C-C	1.34	0.028	1	2.06	0.018	2
C'-C'	1.34	0.028	1	2.06	0.020	2
D-D	1.34	0.028	1	2.06	0.016	2
D'-D'	1.34	0.028	1	2.06	0.020	2
E-E	1.34	0.012	1	1.72	0.010	2
F-F	1.34	0.020	1	1.74	0.016	2
G-G	2.83	0.026	2	1.73	0.014	2
H-H	1.34	0.016	2	1.73	0.016	2
I-I	2.84	0.020	2	1.74	0.020	2
J-J	1.34	0.036	1	2.57	0.020	2
J'-J'	1.34	0.036	1	2.57	0.024	2
K-K	1.34	0.020	1	2.54	0.014	2
K'-K'	1.34	0.020	1	2.54	0.016	2
L-L	1.72	0.012	2	3.02	0.008	4
M-M	1.26	0.020	1	1.84	0.016	2
N-N	1.34	0.024	2	1.75	0.020	2

Table 4.5 Dimensions of J100 tube sections(Kosbab, 2010).

Section	D (m)	t (m)
a-a	1.00	0.016
b-b	1.20	0.016
c-c	0.50	0.010
d-d	1.00	0.014

Table 4.6 Dimensions of J100 built-up wide-flange sections(Kosbab, 2010).

Section	B (m)	t _f (m)	D (m)	t _w (m)
e-e	0.30	0.016	0.33	0.012
f-f	0.42	0.020	0.39	0.016

4.4 TSUNAMI FORCES

Currently available structural design standards and guidelines on loads induced by tsunami inundation (e.g. (FEMA, 2008)) commonly split the tsunami loads into components:

- Buoyant forces;
- Hydrostatic forces;
- Hydrodynamic forces;
- Impulsive forces;
- Debris impact forces;
- Uplift forces.

The preceding tsunami load effects in addition to debris damming forces and additional gravity loads from retained water on elevated floors should be considered for the design of vertical evacuation structures (FEMA, 2008). In the framework of this study, these forces will be applied as static loads to Thessaloniki port buildings to assess their vulnerability to tsunami hazard. In the following, a short description of each component is provided based on (FEMA, 2008) prescriptions.

4.4.1 Determination of tsunami loading (FEMA, 2008)

Buoyant Forces (Fig.4.10)

Buoyant or vertical hydrostatic forces act vertically through the centroid of the displaced volume on a structure or structural component subjected to partial or total submergence.

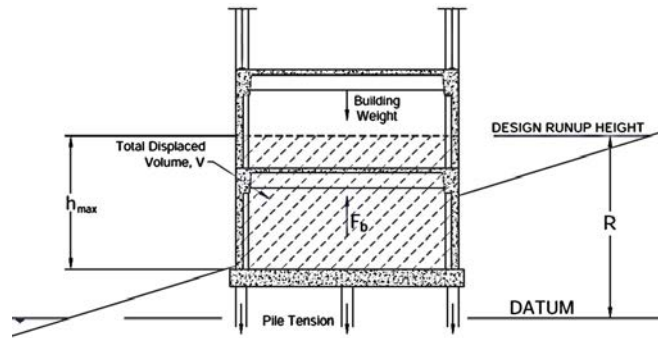


Fig.4.10 Buoyant forces on an overall building with watertight lower levels (FEMA, 2008)

For a watertight structure, the total buoyant force is given by the following equation:

$$F_b = \rho_s g V \quad (4.1)$$

where:

ρ_s is the fluid density including sediment (1200 kg/m^3)

V is the volume of water displaced by the building

Hydrostatic Forces (Fig.4.11)

Hydrostatic forces occur when standing or slowly moving water encounters a structure or structural component. These forces may not be relevant to a structure with a finite (i.e., relatively short) breadth, around which the water can quickly flow and fill in on all sides. They are implemented on walls enclosing watertight areas of a structure.

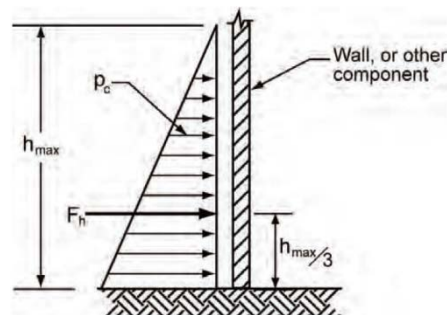


Fig.4.11 Hydrostatic force distribution and location of resultant (FEMA, 2008)

The horizontal hydrostatic force on a wall panel can be computed using the following equation:

$$F_h = p_c A_w = \frac{1}{2} \rho_s g b h_{max}^2 \quad (4.2)$$

where:

- ρ_c is the hydrostatic pressure
- A_w is the wetted area of the panel
- ρ_s is the fluid density including sediment(1200 kg/m³)
- b is the breadth (width) of the wall &
- h_{max} is the maximum water height above the base of the wall at the structure location

Hydrodynamic Forces (Fig. 4.12)

Hydrodynamic forces occur when steady water flows around a structure. Also known as drag forces, they are a combination of the lateral forces caused by the pressure forces from the moving mass of water and the friction forces generated as the water flows around the structure or component.

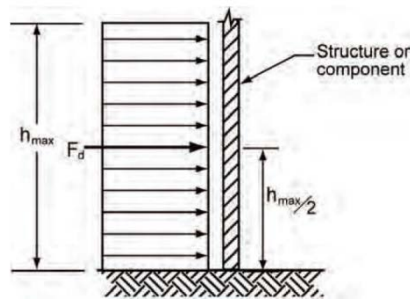


Fig. 4.12 Hydrodynamic force distribution and location of resultant (FEMA, 2008)

Hydrodynamic forces can be computed using the following equation:

$$F_d = \frac{1}{2} \rho_s C_d B (hu^2)_{max} \quad (4.3)$$

where:

- ρ_s is the fluid density including sediment(1200 kg/m³)
- C_d is the drag coefficient (recommended value 2)
- B is the breadth of the structure in the plane normal to the direction of flow
- h is flow depth &
- u is flow velocity at the location of the structure

The hydrodynamic forces are based on the parameter $(hu^2)_{max}$, which is the maximum momentum flux per unit mass occurring at the site at any time during the tsunami. It can be obtained by running a detailed numerical simulation model or acquiring existing simulation data. The value $(hu^2)_{max}$ can be roughly estimated using the following equation:

$$(hu^2)_{max} = gR^2(0.125 - 0.235\frac{z}{R} + 0.11(\frac{z}{R})^2) \quad (4.4)$$

where:

R is the design run-up elevation&

z is the ground elevation at the base of the structure

Impulsive forces (Fig. 4.13)

Impulsive forces are caused by the leading edge of a surge of water impacting a structure.

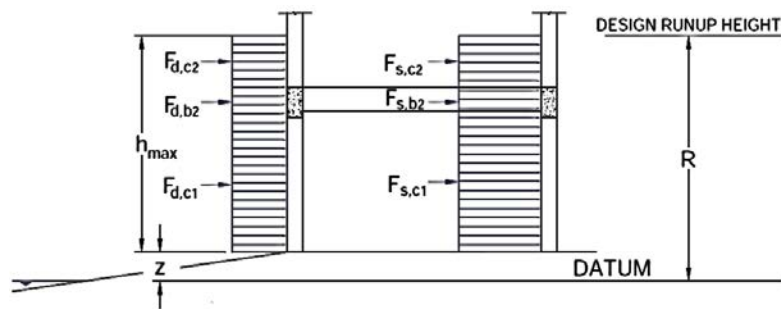


Fig. 4.13 Hydrodynamic impulsive and drag forces on components of a building subjected to inundation by a tsunami bore (FEMA, 2008)

The impulsive forces are conservatively taken as 1.5 times the hydrodynamic force, as shown in the following equation:

$$F_s = 1.5 F_d \quad (4.5)$$

Debris impact forces (Fig. 4.14)

The impact force from waterborne debris (e.g., floating driftwood, lumber, boats, shipping containers, automobiles, buildings) can be a dominant cause of building damage.

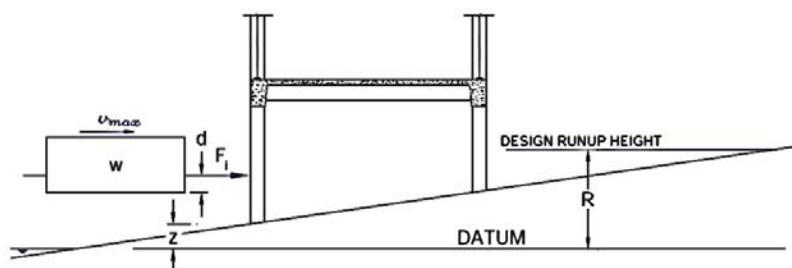


Fig. 4.14 Waterborne debris impact force (FEMA, 2008)

The debris impact force can be estimated using equation:

$$F_i = C_m u_{max} \sqrt{km} \quad (4.6)$$

where:

- C_m is the added mass coefficient (recommended value 2)
- u_{max} is the maximum flow velocity carrying the debris at the site
- m & k are the mass and the effective stiffness of the debris respectively

Approximate values of m and k for common waterborne debris are listed in Table 4.7.

Table 4.7 Mass and Stiffness Properties of Common Waterborne Debris (FEMA, 2008)

Location of Source	Mass (m) in kg	Effective stiffness (k) in N/m
Lumber of Wood Log	450	2.4×10^6
40-ft Standard Shipping Container	3800 (empty)	6.5×10^8
20-ft Standard Shipping Container	2200 (empty)	1.5×10^9
20-ft Heavy Slipping Container	2400 (empty)	1.7×10^9

The magnitude of the debris impact force depends on mass and velocity. Smaller (lighter) debris requiring little or no draft to float can travel at higher velocities than larger (heavier) debris requiring much larger depths to float. Use of maximum flow velocity without consideration of the depth required to float large debris would be unnecessarily conservative.

When a suitable numerical simulation model is unavailable, the maximum flow velocity carrying lumber or a wooden log (with essentially no draft) can be estimated using the analytical solution for tsunami runup on a uniformly sloping beach with no lateral topographical variation, given by equation:

$$u_{max} = \sqrt{2gR \left(1 - \frac{z}{R}\right)} \quad (4.7)$$

where:

- g is the acceleration due to gravity
- R is the design run-up height
- z is the ground elevation at the structure (the datum must be at the sea level)

For a shipping container or other similar large debris with draft d , the ratio of the draft d to the maximum run-up height R can be computed, and Fig. 4.15 can be used to estimate the maximum flow velocity.

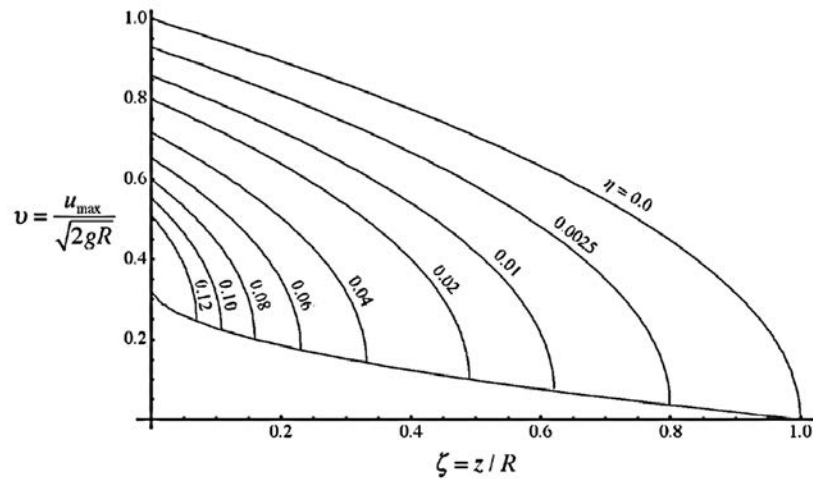


Fig. 4.15 Maximum flow velocity of depth, d , at the ground elevation, z , and maximum run-up elevation, R . The bottom curve represents the lower limit of maximum flow velocity (FEMA, 2008)

Uplift Forces on Elevated Floors (Fig. 4.16)

Uplift forces are due to buoyancy and hydrodynamic forces and are applied to floor levels of a building that are submerged by tsunami inundation.

The total upward buoyant force exerted on a floor system can be estimated using equation:

$$F_b = \rho_s g A_f h_b \quad (4.8)$$

where:

- ρ_s is the fluid density including sediment (1200 kg/m^3)
- A_f is the area of the floor panel or floor framing component, and
- h_b is the water height displaced by the floor (including potentially entrapped air)

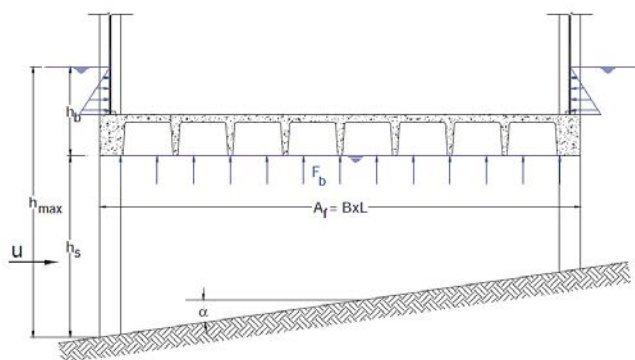


Fig. 4.16 A definition sketch for upward buoyant force exerted on an elevated floor (FEMA, 2008)

4.4.2 Key assumptions for estimating tsunami loading

Tsunami loading is determined using the following key assumptions based on (FEMA, 2008) recommendations and proper engineering judgement.

- Tsunami flows consist of a mixture of sediment and seawater. Based on an assumption of vertically averaged sediment-volume concentration of 10% in seawater, the fluid density of tsunami flow is taken as 1.2 times the density of freshwater, or $\rho_s = 1,200 \text{ kg/m}^3$.
- Considering the significant variability in local tsunami runup heights, based on local bathymetry and topographic effects, and the uncertainty in numerical simulations of tsunami inundation, it is recommended that the design run-up elevation, R , be taken as 1.3 times the predicted maximum run-up elevation, R^* , to envelope the potential variability.
- Considering watertight walls, it is assumed that tsunami flow cannot enter the building for the case of models with masonry infills. Tsunami cannot completely destroy masonry infills. Watertight floor is considered in all models.
- Appropriate combinations of tsunami-induced force components (hydrostatic, hydrodynamic, surge, buoyant and debris impact force) are used in calculating the total tsunami forces acting on the structural models depending on their type.
- Considering that impulsive forces, F_s , are very short duration loads caused by the leading edge of a surge of water impinging on a structure, as the surge passes through a structure, they will be applied sequentially to all structural components, but not at the same time. Once the leading edge of the surge has passed a structural component, it will no longer experience the impulsive force, but rather a sustained hydrodynamic drag force, F_d (FEMA, 2008).
- The worst case lateral load is considered. In particular, when the leading edge of the surge fully impacts the most closed off section of the building, debris impact forces act on the structure.

4.5 NUMERICAL MODELLING

Two-dimensional (2D) numerical simulations of the buildings/cranes are conducted using the fibre-based finite element code Seismostructv7.0 (SeismoSoft, 2015), which is widely and successfully used in structural earthquake engineering.

As noted previously, the RC structures were designed in compliance with the Greek Seismic Code '59 (Kappos et al., 2006) and were realistically reproduced in Seismostruct using nonlinear constitutive models. Inelastic force-based formulations are implemented for the nonlinear beam-column frame element modeling. Distributed material inelasticity is applied based on the fibre approach to represent the cross-sectional behaviour (Neuenhofer & Filippou, 1997). Each fibre is associated with a uniaxial stress-strain relationship and the sectional stress-strain state of the beam-column elements is obtained through the integration of the nonlinear uniaxial stress-strain response of the individual fibres into which the section is subdivided. In the present analysis, the frame sections have been discretized into 300 fibres. The concrete fibres are modelled based on the uniaxial nonlinear model proposed by (Mander, 1988), assuming a constant confining pressure for the confined concrete core fibres throughout the entire stress-strain range. For the reinforcement, a uniaxial bilinear stress-strain model with kinematic strain hardening is utilized.

The nonlinear response of the masonry panel element in the case of the infilled frame models is simulated based on the double strut model proposed by (Crisafulli, 1997). Each panel is represented by strut members that carry the axial loads across two opposite diagonal corners and the shear from the top to the bottom of the panel. This latter strut acts only across the diagonal in compression; hence its activation depends on the deformation of the panel. The axial load struts use the masonry strut hysteresis model, while the shear strut uses a dedicated bilinear hysteresis rule, both developed and initially programmed by Crisafulli(1997) and implemented in SeismoStruct by Blandon(2005). For the simulation of dual frames, appropriate constraints (i.e. *rigid links*) are considered to account for the stiffness of the walls. In addition, in models with more than one frame, *Equal DOF* constraints are used to take into consideration the equal degrees-of-freedom between the frames.

Regarding the warehouse modelling, the uniaxial bilinear model with kinematic strain-hardening is employed for the steel material ($E_s = 2.1 \cdot 10^8 \text{ kPa}$; $f_y = 235000 \text{ kPa}$; $\mu = 0.01$). Columns are modelled using force-based inelastic frame elements (*infrmFB*) with 4 integration sections, while trusses are modelled through truss elements (*truss*). The number of fibres used in section equilibrium computations in both cases is set to 300. The masses are applied as distributed along columns and beams (by assigning the specific weight of steel material) plus concentrated vertical loads on joints due to the existence of trusses on the normal direction.

The 3D container crane model is realistically symmetrical about the trolley-travel direction, with two parallel structural frames joined at top and bottom by trolley girder support beams (TGSBs) and sill beams, respectively (Kosbab, 2010) (Fig.4.7). Thus, a simplified 2D analytical crane model representing the trolley-travel direction may adequately represent the crane's critical response to tsunami forces. Each frame is comprised of a portal frame on the first story and a braced frame second story. Atop the main frame is an A-frame system joining at the apex, or top beam. The trolley girder is rigidly attached to the bottom of the trolley-girder support beams (TGSBs), and supported by a backstay. The boom is pinned to

the trolley girder on the waterside (ws), and held by inner and outer forestays. As for the warehouse, the steel material is simulated using the uniaxial bilinear model with kinematic strain-hardening. The material properties ($E_s = 2.0 \cdot 10^8$ kPa; $f_y = 393000$ kPa; $\mu = 0.01$) are defined based on the study of Kosbab (2010). Beams and columns of portal and braced frames, the boom and the trolley girder are modelled through force-based inelastic frame elements with 4 integration sections while elastic truss elements are used to model the lower and upper diagonals, the A-Frame, the TGSB Tie, the forestays and the backstays (Fig.4.8). The number of fibres used in section equilibrium computations in the former cases is set to 300, while in the latter (i.e. for the forestays and the backstays) is reduced to 100. The mass of the crane is attributed to the mass of structural members (by assigning the specific weight of steel material) and their attachments, as well as major machinery and equipment (by assigning additional distributed or nodal masses). A summary of the assigned overall weight, including the major equipment and machinery is provided in Kosbab (2010). *Equal DOF* constraints are placed between the corners of the structural frame and the attached boom and trolley girder to take into consideration the equal degrees-of-freedom between them. In addition *Equal DOF* constraints are placed between the portal legs and the pseudo-trucks representing the relative equal translational and rotational degrees of freedom. The built-up hollow box sections of cranes (Fig.4.9) are modelled as unstiffened hollow box sections with equivalent thickness which have the same moment of inertia as the corresponding built-up hollow box sections they replace.

Tsunami nonlinear static time-history analyses are performed for all numerical simulations. It is noted that a permanent static analysis is carried out before the onset of tsunami nonlinear analysis to account for the gravity forces. Tsunami forces calculated according to FEMA (FEMA, 2008) are statically imposed on the structures at the location of each load's resultant depending on the inundation depth (d). In particular, the hydrodynamic (F_d) and impulsive (F_s) forces are applied at $d/2$ from the base of the structure, the debris impact force (F_i) is applied at d from the base of the structure while the hydrostatic forces (F_h) are applied at $d/3$ from the base of the structure. Buoyant forces (F_b) are applied at the base of the RC buildings where a connecting beam is considered. The uplift forces are applicable only in the cases where the inundation depth exceeds the height of the first floor (i.e. for the 4-story and 9-story MRFs). The amplitude of the tsunami forces increases with increasing inundation depth. Different combinations of tsunami forces were considered according to (FEMA, 2008) prescriptions as well as the assumptions presented in the previous section. More specifically, two different conditions were considered based on the hypothesis that the tsunami flow may or may not enter the building. In the first one tsunami flow cannot enter the building and cannot completely destroy the existing masonry infills, while in the second one it is assumed that tsunami flow can enter the building considering models without masonry infills. All tsunami loads were applied in proportion to each other assuming linearly increasing time-variant loads with a constant time step up to the (maximum) calculated values. The analyses are performed for different levels of inundation depth (at least 20 levels), varying from very small values (e.g. $d=0.5$ m) which result to negligible structural damage to large ones (e.g. $d=10$ m) which may lead to significant structural damages and potential collapse. All the combinations of tsunami loading for the different analysed building types are presented in Fig. 4.17 to Fig. 4.22.

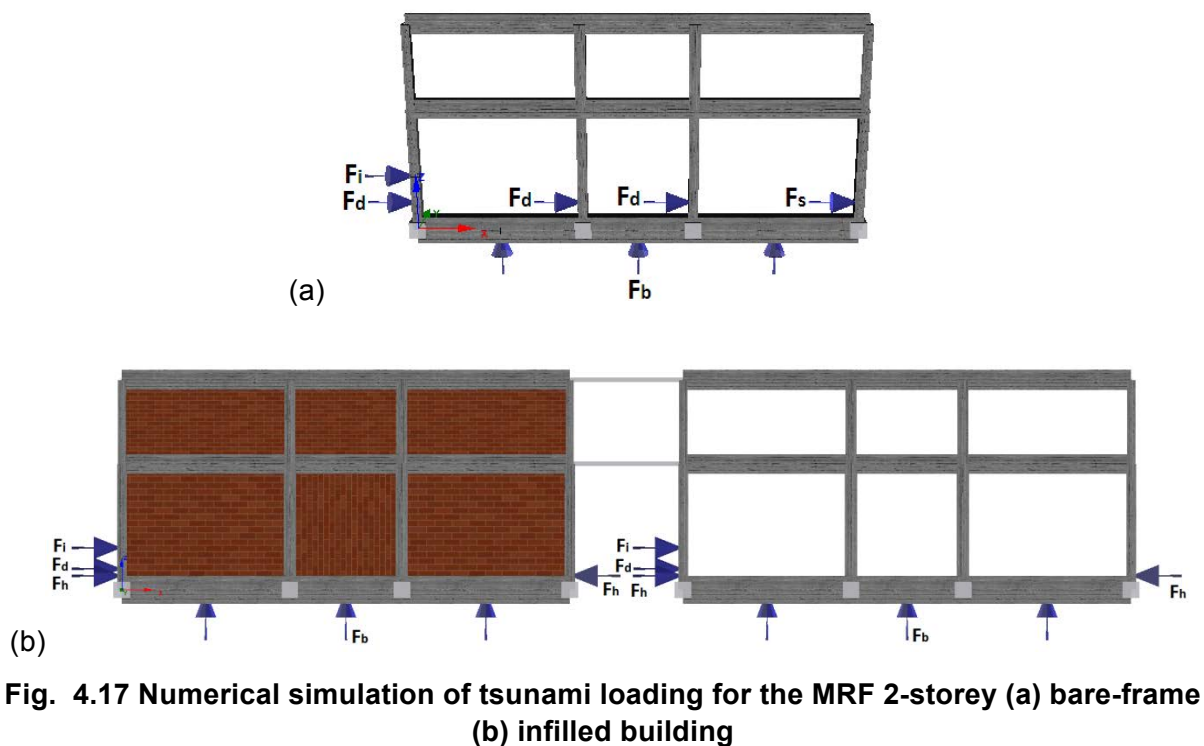


Fig. 4.17 Numerical simulation of tsunami loading for the MRF 2-storey (a) bare-frame (b) infilled building

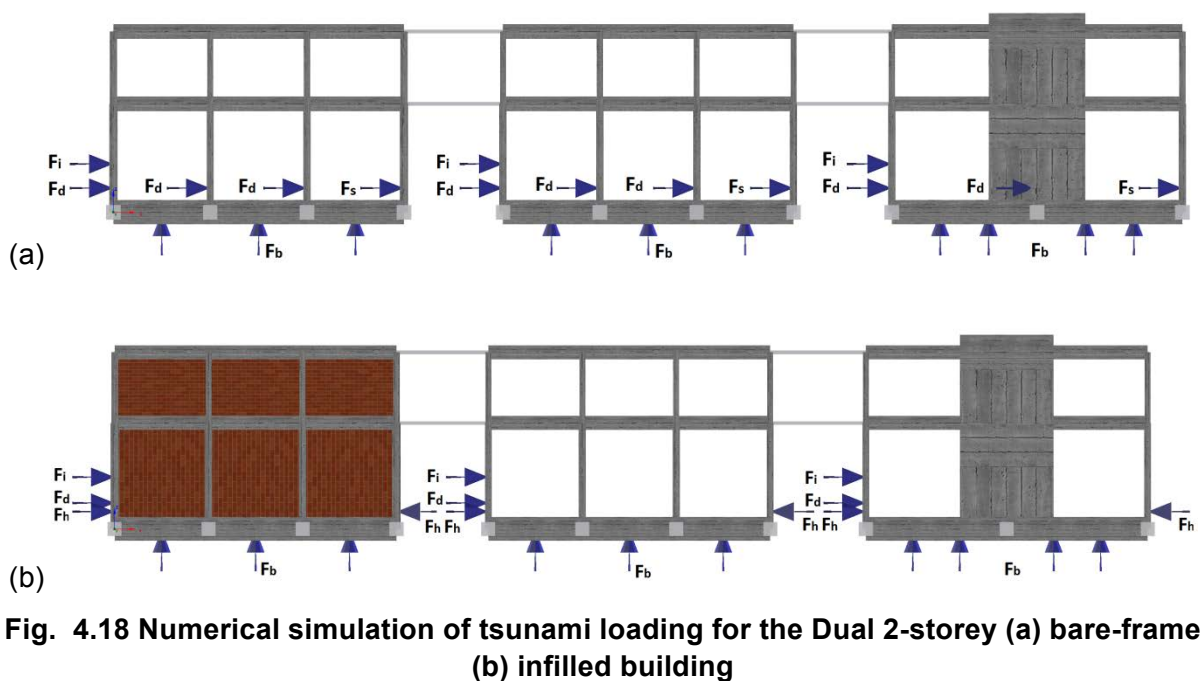


Fig. 4.18 Numerical simulation of tsunami loading for the Dual 2-storey (a) bare-frame (b) infilled building

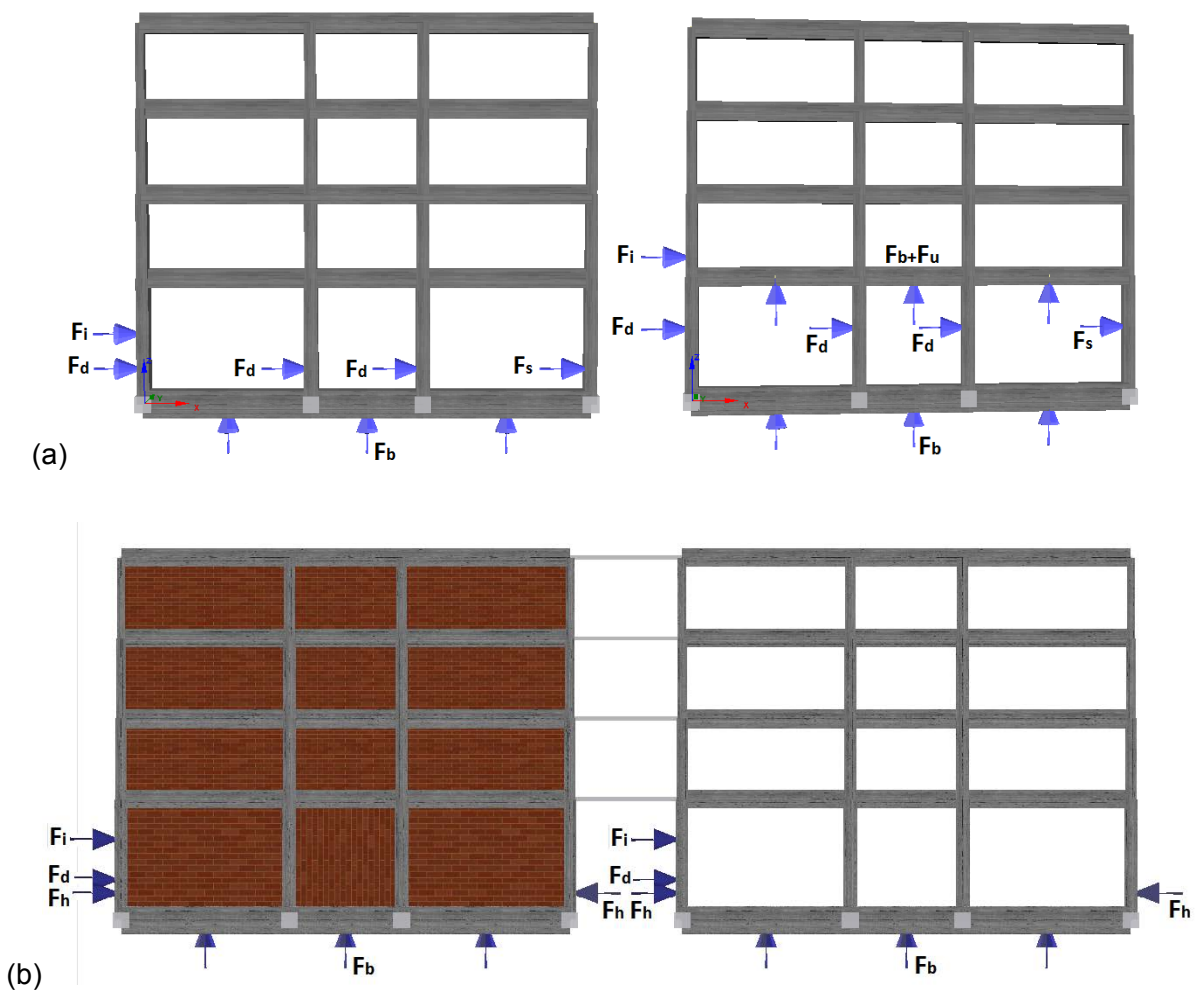


Fig. 4.19 Numerical simulation of tsunami loading for the MRF4-storey (a) bare-frame (b) infilled building

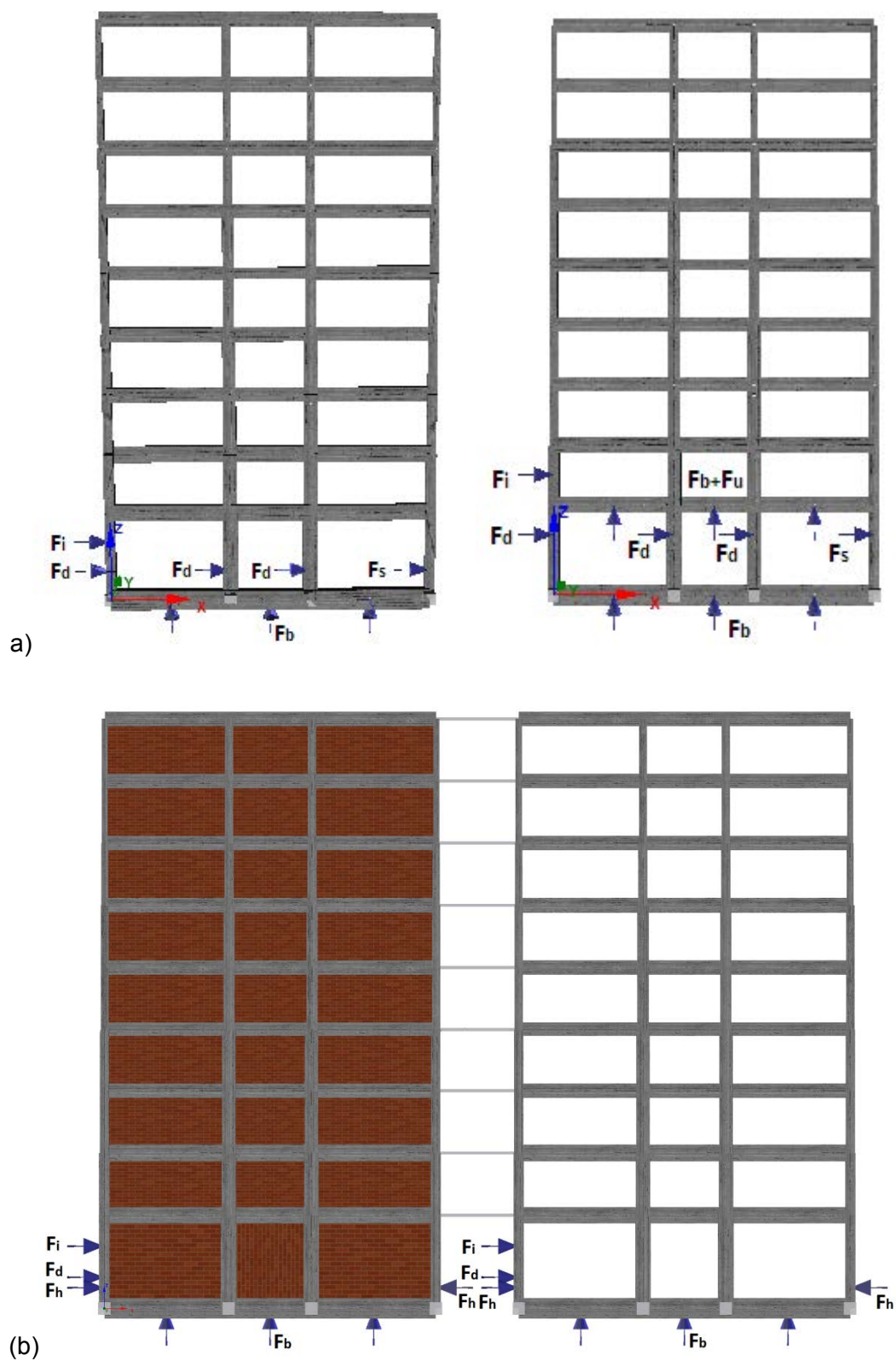


Fig. 4.20 Numerical simulation of tsunami loading for the MRF 9-storey (a) bare-frame (b) infilled building

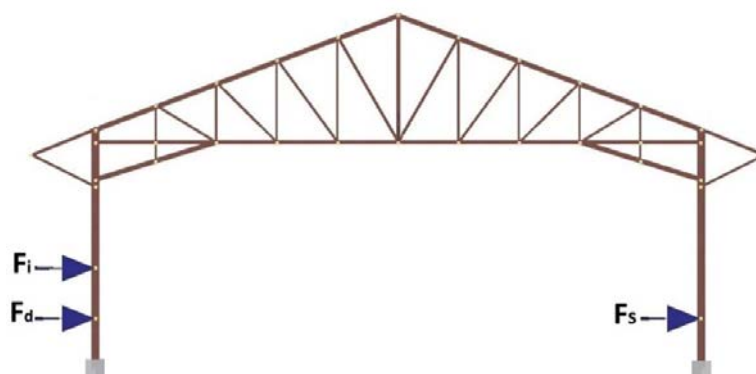


Fig. 4.21 Numerical simulation of tsunami loading for the warehouse

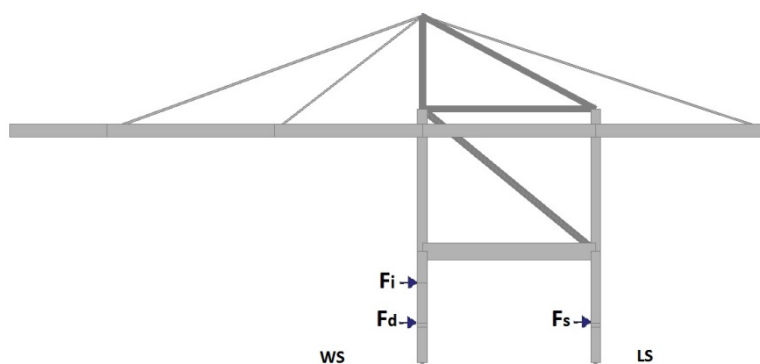


Fig. 4.22 Numerical simulation of tsunami loading for the crane (WS: Water Side,LS: Land Side)

4.6 FRAGILITY CURVES

4.6.1 Definition of limit damage states

The definition of realistic limit damage states is of paramount importance for the construction of fragility curves. The selection of appropriate EDP to correlate with the selected IM (inundation depth) is a challenge as a suitable EDP has not yet been established in literature. When a building response to tsunami comprises structural damage, damage states can be classified using the same schemes used for structural damage triggered by an earthquake (Bird et al. 2005). However, the use of a global damage index such as the interstory drift is not appropriate to be used as a tsunami EDP as the expected deformed shape and damage mechanism of the structure impacted by a tsunami is quite different from that of the same structure subjected to ground shaking. Thus, a local damage index in terms of building's material strain can be used as it shows an improved correlation with structural damage (Macabuag et al., 2014). Four limit states (LS1, LS2, LS3 and LS4) are defined based on nonlinear static analyses (both seismic pushover and tsunami time history analyses) for the various typologies of the buildings and the crane, engineering judgment and the available literature (e.g. HAZUS-MH (2009), FEMA (2004), Crowley et al. (2004), Fotopoulou and Pitilakis (2013a; 2013b)). They describe the exceedance of minor, moderate, extensive and complete damage of the structures. According to (FEMA, 2004), "Steel Light Frames" structures are mostly single story structures combining rod-braced frames in one direction and moment frames in the other. Due to the repetitive nature of the structural systems, the type of damage to structural members is expected to be rather uniform throughout the structure. Consequently, warehouses are considered as "Steel Light Frames" structures. A qualitative description of each damage state for reinforced concrete frames, warehouses and unanchored/rail-mounted port cranes is given in Table 4.8, Table 4.9 and Table 4.10, respectively, while the limit state values finally adopted are presented in Table 4.11 and Table 4.12.

In order to minimize the uncertainties associated with the selection of the appropriate damage state limits, nonlinear static analyses including seismic pushover and tsunami time history analyses are performed for the different analyzed structures to define structure-specific limit state values (in terms of strains) for each damage state.

Regarding the RC buildings, first a seismic pushover analysis is conducted to obtain a preliminary estimation of the damage states defined on the capacity curve. An iterative procedure is followed to derive, for each damage limit state, the steel and concrete strains, which yield the corresponding roof displacement on the curve. It is seen that for all analysis cases, steel strain (ϵ_s) gives more critical results. Hence, hereafter, the proposed limit damage states are defined in terms of steel strain. In particular, for the MRF models with bare frames the first limit state is specified as steel bar yielding while for the infilled ones the infills cracking is assigned as the first limit state and steel bar yielding as the second one. For the rest limit states, mean values of post-yield limit strains for steel reinforcement are suggested. For the dual models, the steel strain limits considered in MRF models cannot be used to characterize the extensive and complete damage of the dual systems, as they lead to lower levels of top displacement on the capacity curve. Thus, increased values of steel strain limits were adopted. It should be noted that the behaviour of the dual models when considering or not infills does not change considerably. This is to be expected considering that the contribution of the infills to the total stiffness of the model is small compared to that

of the shear-wall. Based on the above considerations, the same limit strain values were specified for both bare and infilled dual structures. The same procedure is followed for the definition of the limit state values for the steel structures, namely the warehouse and the crane.

The next Tables show the definition of limit states on the seismic capacity curves for the different RC building typologies and the steel structures considered. Then, tsunami nonlinear static analyses are performed to verify (or potentially slightly modify) the selected limit state values.

Table 4.8 Structural damage state descriptions for RC frame buildings (Crowley et al., 2004).

Damage state	Structural damage	Description
LS1	None to slight	Linear elastic response, flexural or shear-type hairline cracks (<1.0mm) in some members, no yielding in any critical section.
LS2	Moderate	Member flexural strengths achieved, limited ductility developed, crack widths reach 1.0mm, initiation of concrete spalling.
LS3	Extensive	Significant repair required to building, wide flexural or shear cracks, buckling of longitudinal reinforcement may occur.
LS4	Complete	Repair of building not feasible either physically or economically, demolition required, could be due to shear failure of vertical elements or excessive displacement.

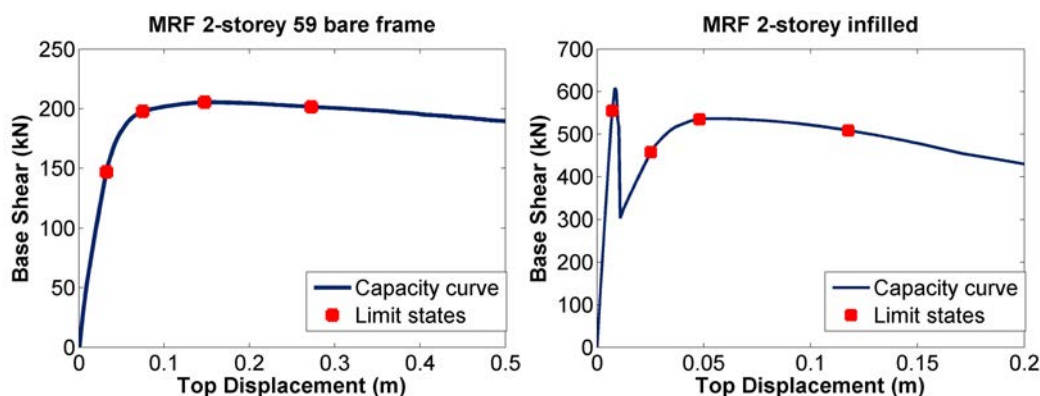
Table 4.9 Structural damage state descriptions for warehouses (Steel Light Frames) (FEMA, 2004).

Damage state	Structural damage	Description
LS1	Slight	Few steel rod braces have yielded which may be indicated by minor sagging of rod braces. Minor cracking at welded connections or minor deformations at bolted connections of moment frames may be observed.
LS2	Moderate	Most steel braces have yielded exhibiting observable significantly sagging rod braces; few brace connections may be broken. Some weld cracking may be observed in the moment frame connections.
LS3	Extensive	Significant permanent lateral deformation of the structure due to broken brace rods, stretched anchor bolts and permanent deformations at moment frame members. Some screw or welded attachments of roof and wall siding to steel framing may be broken. Some purlin and girt connections may be broken.
LS4	Complete	Structure is collapsed or in imminent danger of collapse due to broken rod bracing, failed anchor bolts or failed structural members or connections. Approximately 3% of the total area of the buildings with Complete damage is expected to be collapsed.

Table 4.10 Structural damage state descriptions for unanchored/rail-mounted port cranes (FEMA, 2004).

Damage state	Structural damage	Description
LS1	Slight/Minor	Slight damage to structural members with no loss of function for the stationary equipment, while for the unanchored or rail mounted equipment minor derailment or misalignment without any major structural damage to the rail mount. Minor repair and adjustments may be required before the crane becomes operable.
LS2	Moderate	Derailment due to differential displacement of parallel track. Rail repair and some repair to structural members are required.
LS3	Extensive	Considerable damage to equipment. Topped or totally derailed cranes are likely to occur. Replacement of structural members is required.
LS4	Complete	The same as for Extensive Damage.

The next figures illustrate the corresponding tsunami capacity curves derived from the tsunami nonlinear static analyses. It is noted that the tsunami capacity curves are not extracted from a single nonlinear static analysis as for the seismic case but from the total number of the tsunami nonlinear static time history analyses. This is done considering that the location and amplitude of the applied tsunami forces changes as a function of the inundation depth. It is worth noticing however that the seismic and tsunami capacity curves present consistent results predicting very similar damage state limits.


Fig. 4.23 Definition of limit states on the seismic capacity curves for the different structure typologies considered

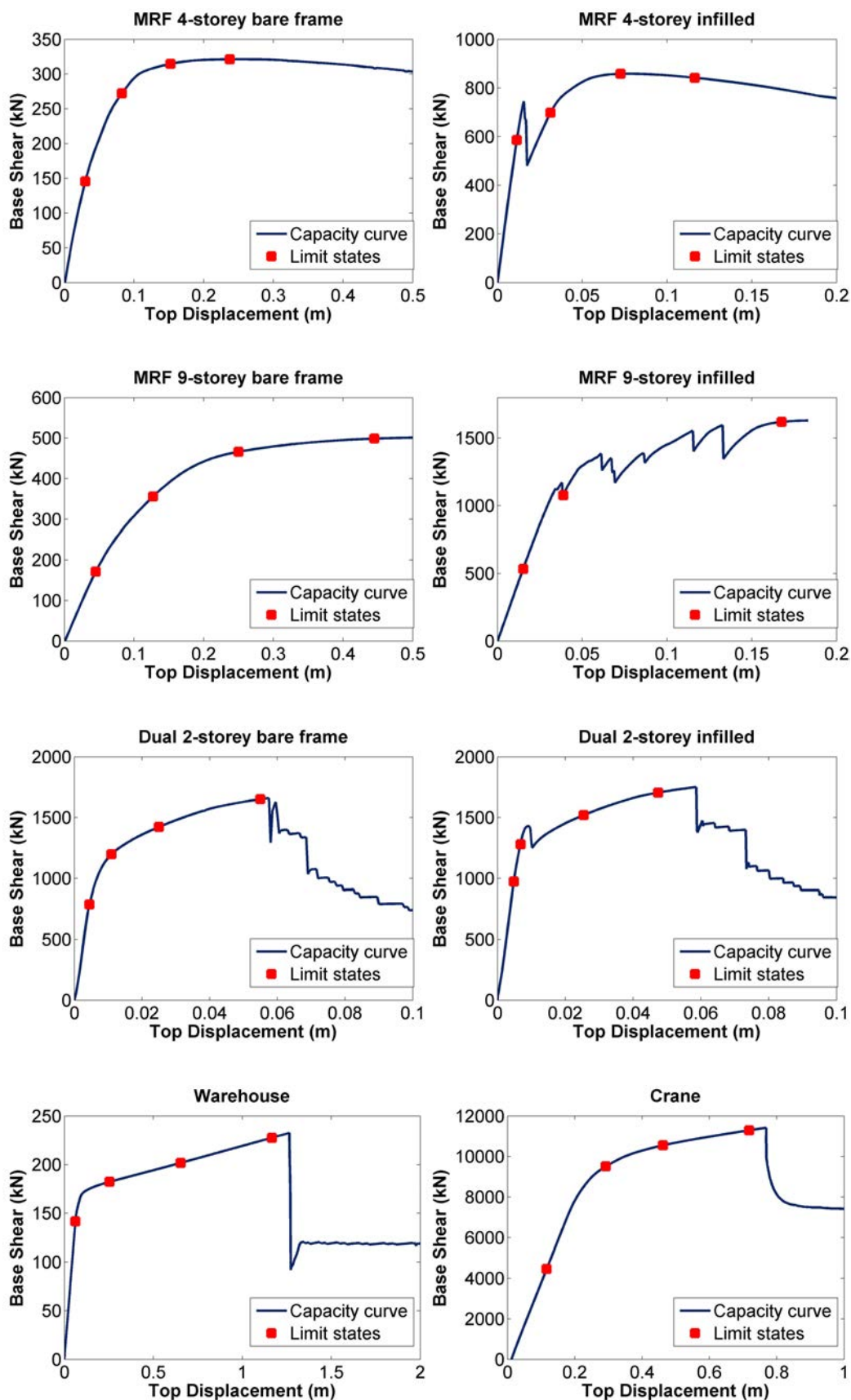


Fig.4.23 Definition of limit states on the seismic capacity curves for the different structure typologies considered (continued)

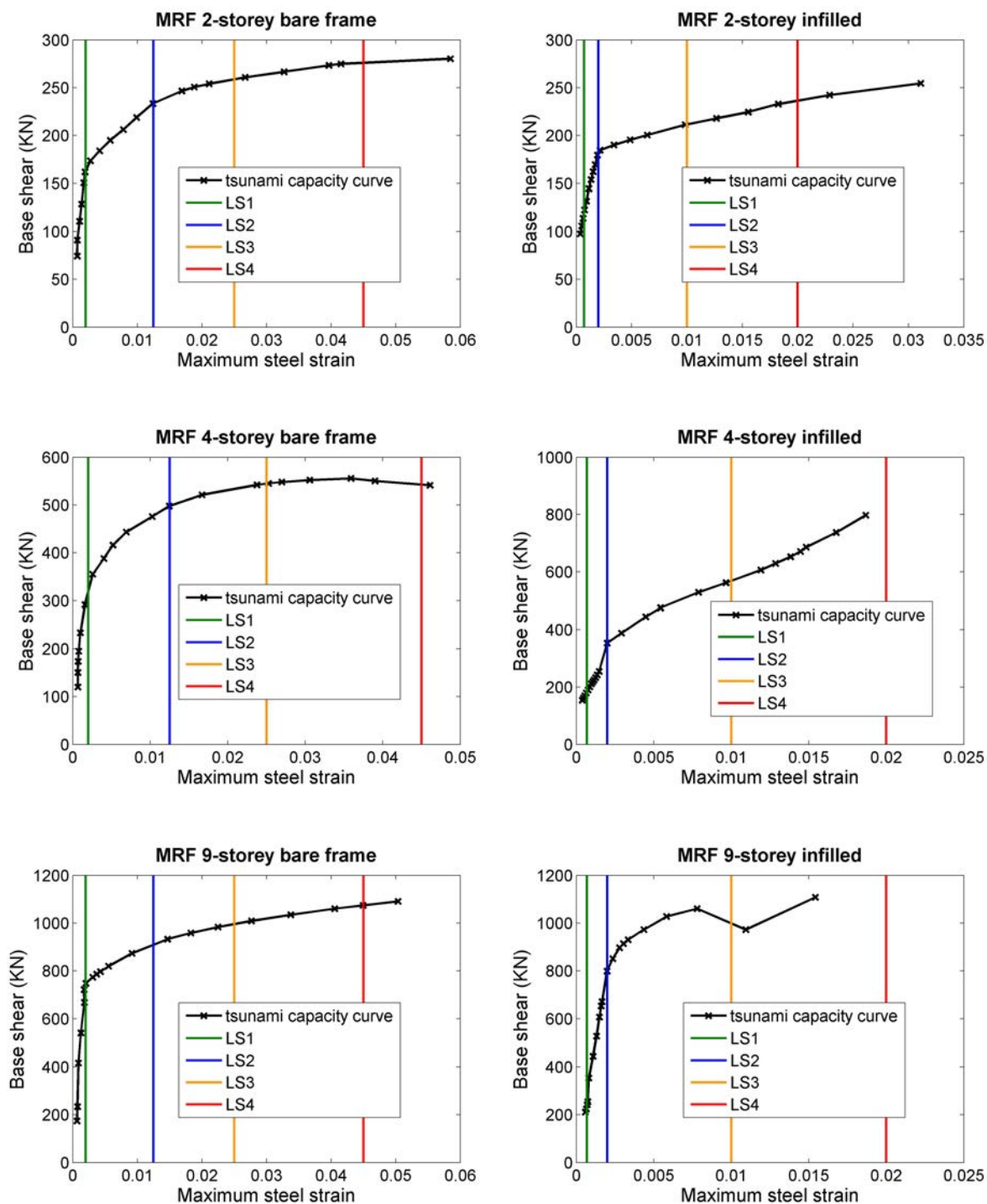


Fig. 4.24 Definition of limit states on tsunami capacity curves for the different structure typologies considered

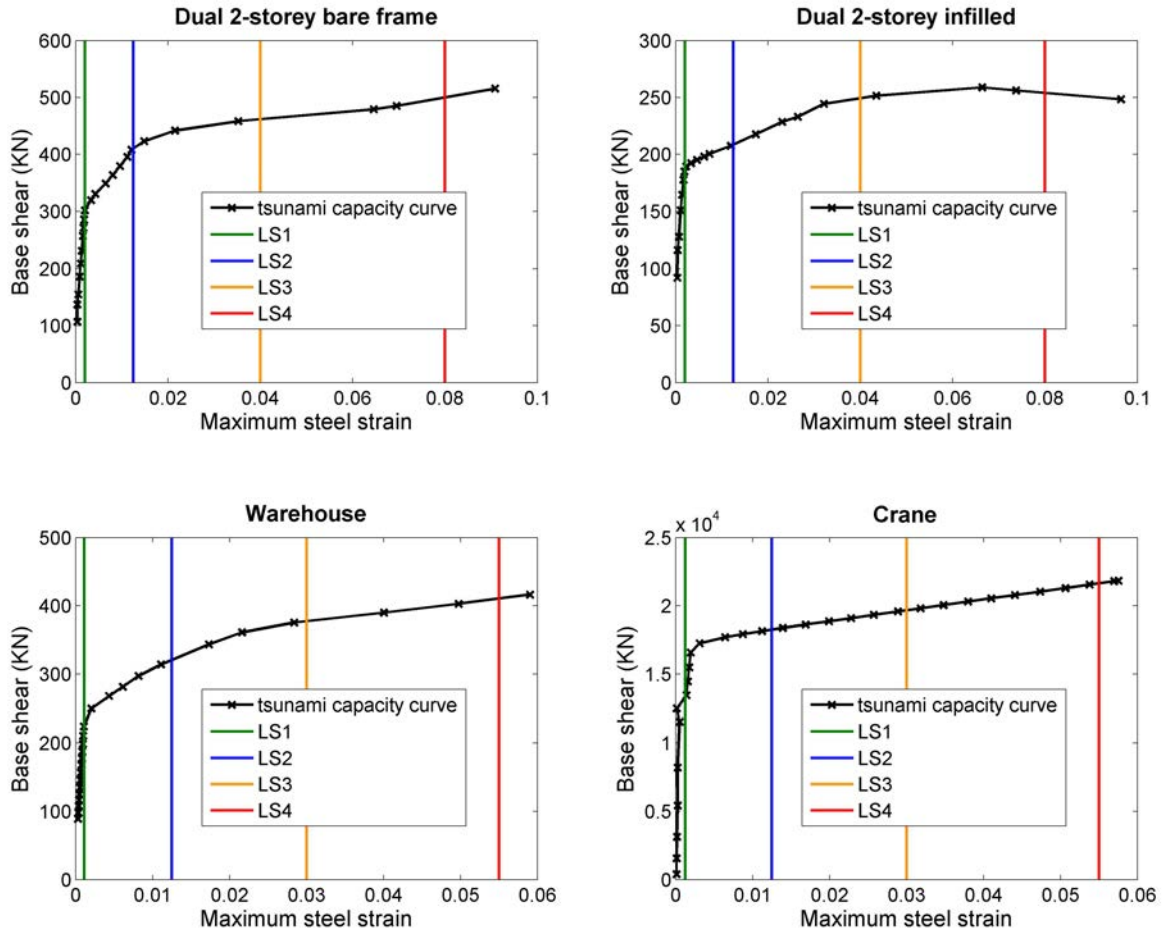


Fig. 4.25 Definition of limit states on tsunami capacity curves for the different structure typologies considered (continued)

The selected limit state values finally adopted for the tsunami vulnerability analysis are presented in Table 4.11 and Table 4.12 for the RC buildings and the steel structures respectively.

Table 4.11 Definition of limit states for the different RC building typologies considered

Limit states	Steel strain (ϵ_s)		
	MRF bare frames	MRF with infills	Dual with/without infills
Limit state 1	0.002 (Steel bar yielding)	0.0007 (infills cracking)	0.002 (Steel bar yielding)
Limit state 2	0.0125	0.002 (Steel bar yielding)	0.0125
Limit state 3	0.025	0.010	0.04
Limit state 4	0.045	0.020	0.08

Table 4.12 Definition of limit states for the warehouse and the crane

Limit states	Steel strain (ϵ_s)	
	Warehouse	Crane
Limit state 1	0.00112 (Steel bar yielding)	0.00125 (Steel bar yielding)
Limit state 2	0.0125	0.0125
Limit state 3	0.03	0.03
Limit state 4	0.055	0.055

4.6.2 Construction of fragility curves

Fragility curves describe the probability of exceeding predefined levels of damage under a tsunami event of a given intensity. The results of the nonlinear numerical analysis (inundation depth - steel strain values) are used to derive fragility curves expressed as two-parameter time-variant lognormal distribution functions.

The following equation gives the cumulative probability of exceeding a DS conditioned on a measure of the tsunami intensity IM :

$$P[DS_i/IM] = \Phi\left(\frac{\ln(IM) - \ln(\overline{IM}_i)}{\beta}\right) \quad (4.9)$$

where, Φ is the standard normal cumulative distribution function, IM is the intensity measure of the tsunami expressed in terms of inundation depth (in units of m), \overline{IM}_i and β are the median values (in units of m) and log-standard deviations respectively of the building fragilities for each damage state i and DS_i is the damage state. The median values of inundation depth respectively corresponding to the prescribed damage states are determined based on a regression analysis of the nonlinear static analysis results (inundation depth - steel strain pairs) for each structural model. More specifically, a second order polynomial fit of the logarithms of the inundation depth - steel strain data, which minimizes the regression residuals, is adopted in all cases. Fig. 4.26 shows indicatively the derived inundation depth – steel strain relationships for the MRF 2-storey infilled building.

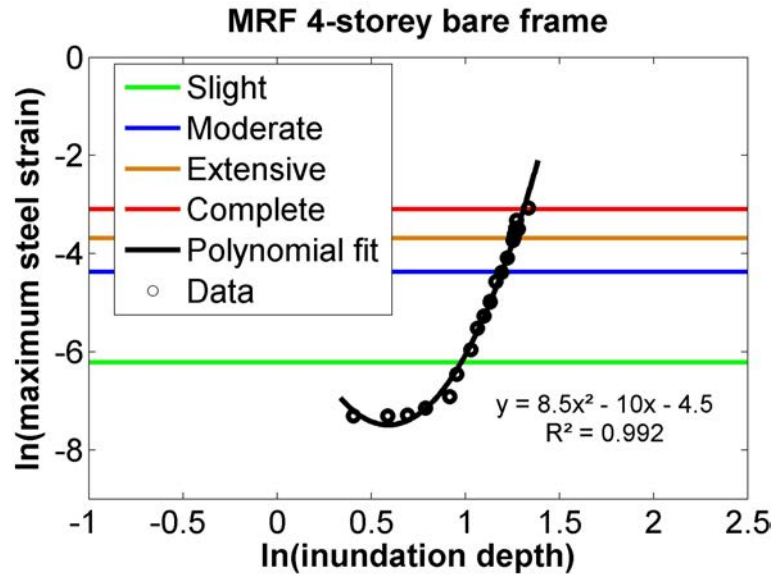


Fig. 4.26 Inundation depth- steel strain relationships for the MRF 2-storey infilled building.

The various uncertainties are taken into account through the log-standard deviation parameter β , which describes the total dispersion related to each fragility curve. The primary sources of uncertainty which contribute to the total variability for any given damage state are those associated with the capacity of each structural type and the demand. The log-standard deviation value in the definition of the capacity is assumed to be equal to 0.3 for low code buildings (FEMA, 2004) and 0.25 for the modern jumbo crane. The uncertainty in the demand is considered by calculating the dispersion of the logarithms of inundation depth - steel strain simulated data with respect to the regression fit. Under the assumption that these two log-standard deviation components are statistically independent, the total log-standard deviation is estimated as the root of the sum of the squares of the component dispersions. The herein computed log-standard deviation β values of the curves vary from 0.33 to 0.59 for all structural models. Table 4.13 presents the lognormal distributed fragility parameters (median and log-standard deviation) in terms of inundation depth, and illustrate the corresponding sets of fragility curves for the various RC building typologies and for the warehouse and the crane respectively (Fig. 4.27 and Fig. 4.28).

Table 4.13 Parameters of fragility functions

Structural system	Median inundation depth (m)				Dispersion β
	LS1 (m)	LS2 (m)	LS3 (m)	LS4 (m)	
MRF 2-storey bare-frames	1.85	2.38	2.56	2.71	0.43
MRF 2-storey infilled	1.16	1.57	2.11	2.33	0.37
Dual 2-storey bare-frames	1.14	1.57	1.83	1.99	0.40
Dual 2-storey infilled	0.96	1.27	1.46	1.57	0.44
MRF 4-storey bare-frames	2.66	3.30	3.52	3.70	0.33
MRF 4-storey infilled	1.81	2.43	3.33	3.74	0.40
MRF 9-storey bare-frames	4.01	4.97	5.30	5.57	0.39
MRF 9-storey infilled	2.27	3.81	5.49	6.19	0.35
Warehouse	2.20	2.79	2.97	3.10	0.57
Crane	13.14	15.37	16.16	16.69	0.59

It may be observed that, the higher the height of the RC building, the lower its vulnerability. It is also shown that the low-rise and mid-rise models with infills are more vulnerable compared with the corresponding models with bare frames. This trend also holds true for the high-rise MRF for the exceedance of slight and moderate damage. This is in accordance with the FEMA guideline, which recommends the design of vertical evacuation buildings with break-away walls or open construction in the lower levels to allow water to pass through with minimal resistance.

In contrast, when extensive or complete damage of the structures is anticipated, the bare RC frame is expected to sustain larger damages in comparison with the corresponding infilled one. This could be attributed to the height of the building, which makes its behaviour unpredictable for higher levels of damage.

Furthermore, it is seen that the low-rise dual RC models are more vulnerable compared to the corresponding MRFs. The latter could be related to the concentration of large tsunami forces in shear walls. This is the reason why FEMA recommends that for the design of vertical evacuation structures, shear walls should be oriented parallel to the anticipated direction of tsunami flow to reduce associated tsunami forces.

Regarding the steel structures, i.e. the warehouse and the crane, it is seen that although the numerically calculated limit state values are the same for all damage states (see

), they present, as it would be expected, a completely different behavior in terms of fragility. In particular, the warehouse presents fragility values that are generally closer to that of the low-rise and mid-rise MRF RC buildings while the crane, as it would be expected, is significantly less vulnerable compared to all building types analyzed. It is also observed that the derived curves for the warehouse are very close together. Thus, once the warehouse has yielded, it will very rapidly also attain the post-yield limit states.

Fig. 4.29 to Fig.4.32 present representative comparisons of the herein developed numerical tsunami fragility curves with the corresponding empirical ones of Suppasri et al. (2011) (Indian Ocean tsunami in Thailand) and Suppasri et al. (2013) (Great East Japan tsunami).

As can be seen, a good agreement between the curves is observed in general. The existing differences can be attributed to the fact that the empirical fragility curves chosen for comparison were constructed based on hazard-damage relationships from previous different tsunami events (i.e. the Indian Ocean tsunami in Thailand and the Great East Japan tsunami) and/or expert judgment. In addition, the proposed fragility curves refer to low code buildings in contrast to the empirical ones that include different design codes. Therefore, only preliminary comparisons of the herein numerically developed fragility curves with the empirical ones can be made as the latter are highly specific to a particular seismo-tectonic, geotechnical and built environment.

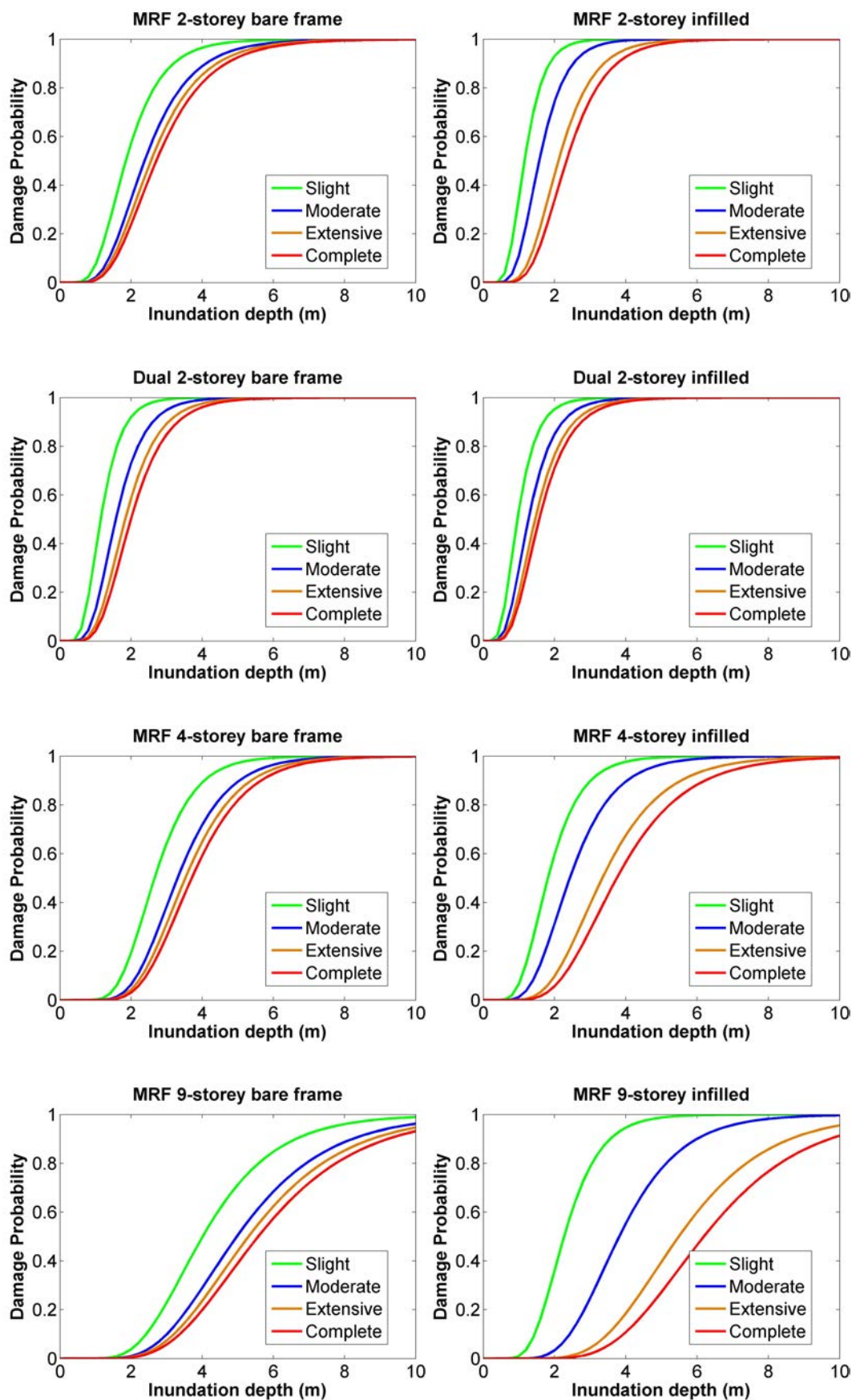


Fig. 4.27 Fragility curves for the different RC building typologies considered.

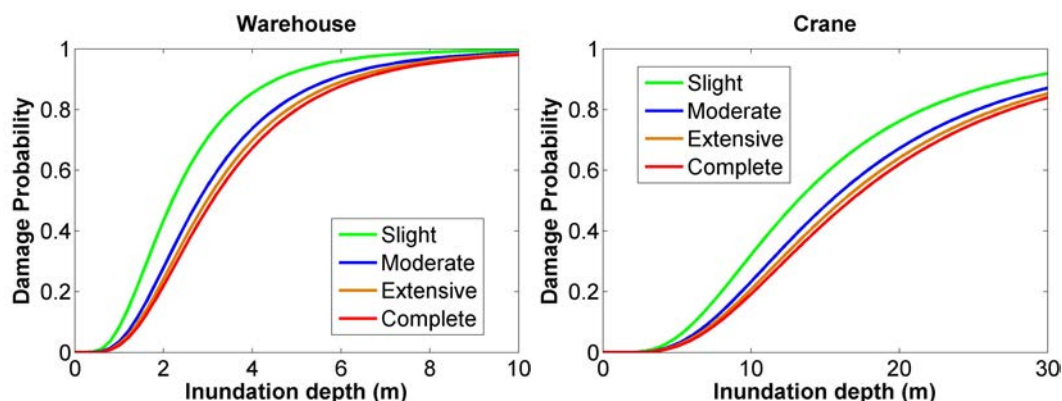


Fig. 4.28 Fragility curves for the warehouse and the crane.

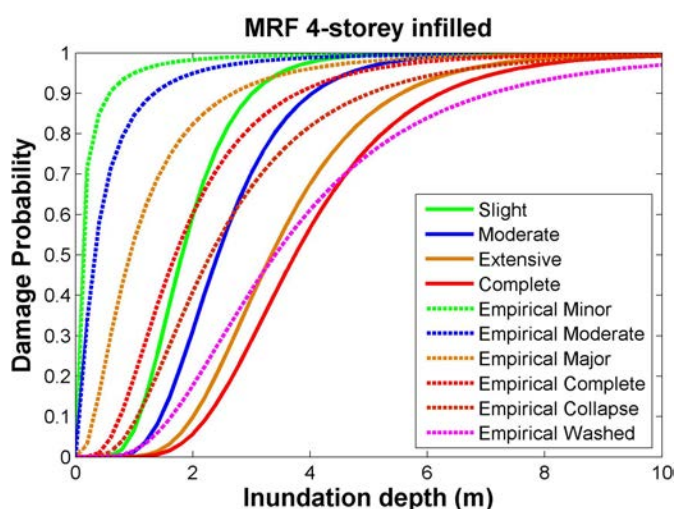


Fig. 4.29 Comparison of the numerical tsunami fragility curves for the MRF 4-storey infilled building with the corresponding empirical ones of Suppasri et al. (2013) (Great East Japan tsunami, RC-mixed structural material)

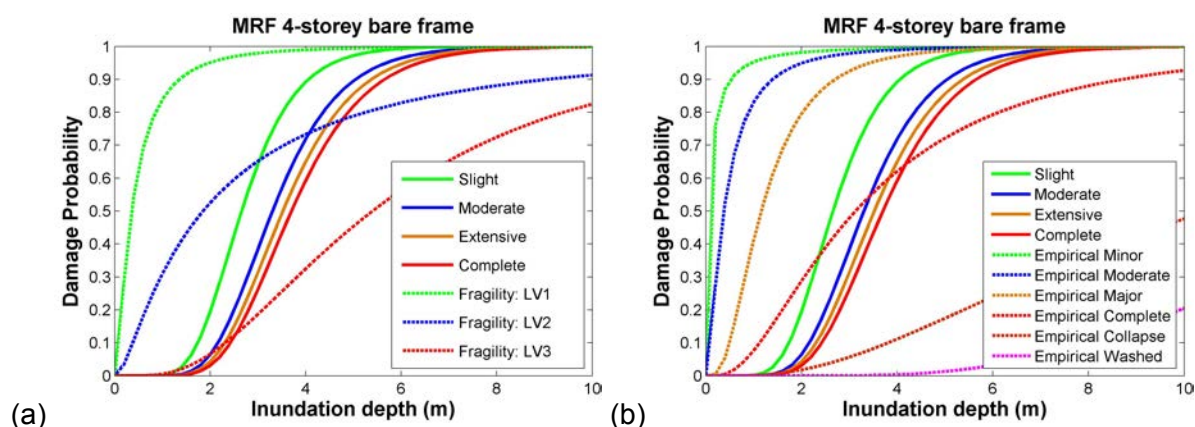


Fig. 4.30 Comparison of the numerical tsunami fragility curves for the MRF 4-storey bare-frame building with the corresponding empirical ones of (a) Suppasri et al. (2011) (Indian Ocean tsunami in Thailand, RC-structures) and (b) Suppasri et al. (2013) (Great East Japan, RC-structures).

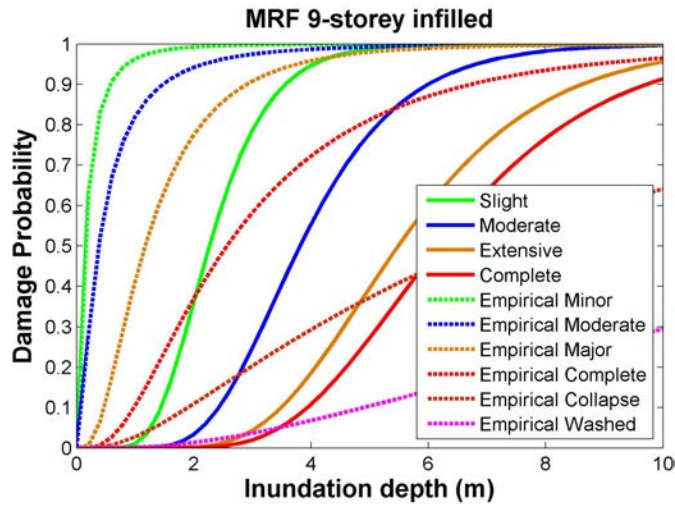


Fig. 4.31 Comparison of the numerical tsunami fragility curves for the MRF 9-storey infilled building with the corresponding empirical ones of Suppasri et al. (2013) (Great East Japan, RC-3stories or more).

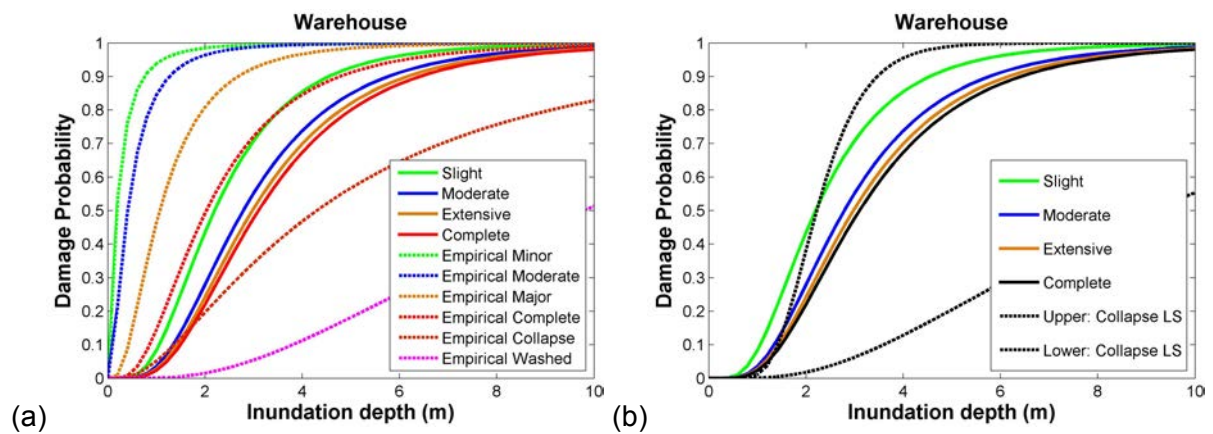


Fig.4.32 Comparison of the numerical tsunami fragility curves for the warehouse with the corresponding empirical ones of Suppasri et al. (2013) (Great East Japan) for (a) steel-structures and (b) dispersion of collapsed steel structures.

4.7 DISCUSSION

Analytical tsunami fragility functions have been developed for various types of low-code RC buildings, a typical warehouse and modern crane as part of the CI-B3 case study (Port of Thessaloniki). An extensive numerical parametric investigation has been performed considering different combinations of statically applied tsunami loads for gradually increasing tsunami inundation depths for the various typologies considered representative of the most strategic Thessaloniki's port buildings and infrastructures. Structural limit states have been defined in terms of threshold values of material strain based on nonlinear static analyses (both seismic pushover and tsunami time history analyses) results. Fragility curves have been finally derived as a function of inundation depth for the various typologies considered.

It has been shown that the higher RC buildings have lower vulnerability values compared to the lower ones. It is also shown that the low-rise and mid-rise models with infills are more vulnerable compared with the corresponding models with bare frames. This trend also holds true for the high-rise MRF for the exceedance of slight and moderate damage. In contrast, when extensive or complete damage of the structures is anticipated, the bare frame is expected to sustain larger damages in comparison with the corresponding infilled one. This could be attributed to the height of the building, which makes its behavior unpredictable for higher levels of damage. Moreover, it is seen that the low-rise dual models are more vulnerable compared to the corresponding MRFs. The latter could be related to the concentration of large tsunami forces in shear walls. Regarding the vulnerability of the steel structures it has been shown that the warehouse presents vulnerability values that are generally closer to that of the low-rise and mid-rise MRF RC buildings while the crane is significantly less vulnerable compared to all building types analyzed.

The developed fragility curves were compared with the available empirical fragility curves from Suppasri et al. (2011; 2013). A good agreement between the curves is generally shown enhancing the reliability of the proposed curves. The proposed fragility curves could be used within a probabilistic risk assessment framework to assess the vulnerability of buildings and infrastructures exposed to tsunami hazard. Knowing the tsunami height from an appropriate tsunami hazard analysis and the characteristics of the exposed infrastructure (geometrical, etc.), one could select and make use of the appropriate set of fragility curves to assess the expected damage state of the structure. The derived fragility curves for the low-code RC buildings could be applicable to typical low-code RC buildings in Greece as well as in Southern Europe in general. Moreover, the suggested curves for the representative warehouse and the container crane provide insight into the tsunami vulnerability of existing port infrastructures (warehouses and cranes). They could be applicable to typical warehouses and modern container cranes for ports worldwide. Stakeholders can use the developed fragility curves to evaluate the risk to their own buildings and infrastructures, and make decisions regarding potential retrofit or replacement to cost-effectively reduce their risk to tsunamis. Future work should also address tsunami vulnerability assessment taking into account additional structural configurations, different combination of tsunami forces as well as soil-structure-interaction (SSI) effects. Finally, comparison of the results with experimental tests would further enforce the validity of the proposed fragility curves.

5 Dissemination

About the project goals, the following documents have been published on an international, specialized journal on industrial risks.

The papers report acknowledgments to the STRESTS project.

- 1) Lanzano, G.; Santucci De Magistris, F.; Fabbrocino, G.; Salzano, E. 2015. Seismic damage to pipelines in the framework of NaTech risk assessment, *Journal of Loss Prevention in the Process Industries*, 33, 159–172.
- 2) Salzano, E.; Basco, A. 2015. Simplified model for the evaluation of the effects of explosions on industrial target, *Journal of Loss Prevention in the Process Industries* 37, 119–123.

6 References

- ALA (2001). Seismic fragility formulations for water system. American Lifeline Alliance (ALA), American Society of Civil Engineers (ASCE) and Federal Emergency Management Agency (FEMA).
- Altarejos-Garcia, L., Silva-Tulla, F., Escuder-Bueno, I., & Morales-Torres, A. (2014). Practical Risk Assessment for Embankments, Dams, and Slopes. In: Risk and Reliability in Geotechnical Engineering, edited by Kok-Kwang Phoon and Jianye Ching. CRC Press.
- Andreev, S. H., & Zhelyazkov, A.Z. (2015). Probability of Failure of an Embankment Dam due to Slope Instability and Overtopping: First Order Second Moment Method for Assessment of Uncertainty. In 13th ICOLD International Benchmark Workshop on Numerical Analysis of Dams. Lausanne, Switzerland.
- API 620 (2015). Design and Construction of Large Welded Low Pressure Storage Tanks. Washington D.C., USA: American Petroleum Institute.
- API 650 (2015). Welded Steel Tanks for Oil Storage. Washington D.C., USA: American Petroleum Institute.
- ASME (2015). Boiler & Pressure Vessel Code. New York, USA: American Society of Mechanical Engineers.
- Bartolomei, A., Lai, C., Corigliano, M., & Tinti, S. (2008). Earthquake and Tsunami-Induced Damage to Seaport Structures in Italy: Application of GIS for Risk Reduction and Monitoring. P. Proceedings of 14th World Conference on Earthquake Engineering. Beijing, China.
- Bird, J.F., Crowley, H., Pinho, R. & Bommer, J.J. (2005). Assessment of building response to liquefaction induced differential ground deformation". *Bul of the New Zealand Society for Earthquake Engineering* 38(4), 215-234.
- Blandon, C. (2005). Implementation of an Infill Masonry Model for Seismic Assessment of Existing Buildings, Individual Study. Pavia, Italy: European School for Advanced Studies in Reduction of Seismic Risk (ROSE School).
- Bommer, J. (2002). Deterministic vs. probabilistic seismic hazard assessment: an exaggerated and obstructive dichotomy. *J. Earthquake Eng.* 6, 43-73.
- Campedel, M., Cozzani, V., Garcia-Agreda, A., & Salzano, E. (2008). Extending the Quantitative Assessment of Industrial Risks to Earthquake Effects. *Risk Analysis* 5, 1231-1246.
- Corbett, G., Reid, S., & Johnson, W. (1996). Impact loading of plates and shells by free-flying projectiles: a review. *Int J Impact Engn.* 18, 141-230.
- Cornell, C. (1968). Engineering seismic risk analysis,. *Bull. Seismol. Soc. Am.* 58, 1583-1606.
- Cozzani, V., & Salzano, E. (2004). Threshold values for domino effects caused by blast wave interaction with process equipment. *J. Loss Prev. Proc.* 17, 437-447.

Cozzani, V., Campedel, M., Renzi, E., & Krausmann, E. (2010). Industrial accidents triggered by flood events: analysis of past accidents. *Journal of Hazard Materials* 175, 501–509.

Crespo, A., Gómez-Gesteira, M., & Dalrymple, R. (2008). Modeling Dam Break Behavior over a Wet Bed by a SPH Technique. *Journal of Waterway, Port, Coastal, and Ocean Engineering*, American Society of Civil Engineers, 134, 313–320.

Crisafulli, F. (1997). *Seismic Behaviour of Reinforced Concrete Structures with Masonry Infills*. (PhD Thesis ed.). University of Canterbury, New Zealand.

Crowley, H., Colombi, M., Silva, M., Ahmad, N., Fardis, M., Tsionis, G., & Erberik, M. (2011). D3.1—fragility functions for common RC building types in Europe, WP3: fragility functions of elements at risk. (FP7): SYNER-G: systemic seismic vulnerability and risk analysis for buildings, lifeline networks and infrastructures safety gain.

Crowley, H., Pinho, R., & Bommer, J. (2004). A probabilistic displacement-based vulnerability assessment procedure for earthquake loss estimation. *Bull Earthq Eng.* 2, 173–219.

Dalrymple, R., & Kriebe, D. (2005). Lessons in engineering from the tsunami in Thailand. *Bridge* 35, 4–13.

Darbre, G. R. (1999). *Dam Risk Analysis*. Bienne, Switzerland.

de Moel, H., & Aerts, J.C.J H. (2011). Effect of Uncertainty in Land Use, Damage Models and Inundation Depth on Flood Damage Estimates. *Natural Hazards* 58, 407–25.

Department of Homeland Security Division Federal Emergency Management Agency Mitigation Division. (2006). *Hazus-MH Technical Manual: Flood Model*. Washington DC, U.S.A.

Dias, W., Yapa, H., & Peiris, L. (2009). Tsunami vulnerability functions from field surveys and Monte Carlo simulation. *Civil Engineering and Environmental Systems* 26, 181–194.

Douglas, J. (2004). *Ground motion estimation equations 1964–2003*. Reissue of ESEE Report No. 01-1: ‘A comprehensive worldwide summary of strong-motion attenuation relationships for peak ground acceleration and spectral ordinates (1969 to 2000)’ with corrections and additions. London, UK: Imperial College.

Eidinger, J. (1998). *Lifelines, Water Distribution Systems in the Loma Prieta, California, Earthquake of October 17, 1989, Performance of the Built Environment – Lifelines*, Report 1552-A. US Geological Survey Professional Paper.

EN 1998-1. (2003). *Eurocode 8: Design of structure for earthquake resistance, Part 1: General rules, seismic actions and rules for buildings*. Bruxelles (BE): European Committee for Standardization.

EN 1998-4. (2003). *Eurocode 8: Design of structures for earthquake resistance - Part 4: silos, tanks and pipelines*. Bruxelles (BE): European Committee for Standardization.

Fabbrocino, G., Iervolino, I., Orlando, F., & Salzano, E. (2005). Quantitative risk analysis of oil storage facilities in seismic areas. *Journal of Hazardous Materials* (12), 361-69.

Favre, A.-C., El Adlouni s., Perreault L., Thiémonge N., & Bobée B. (2004). Multivariate Hydrological Frequency Analysis Using Copulas. *Surface Water and Climate* 40, W01101.

-
- Federal Office for Water and Geology. (2002). Sécurité Des Ouvrages D'accumulation Ver. 1.1 - Ordonnance Sur La Sécurité Des Ouvrages D'accumulation (OSOA). Directives. Biel, Switzerland: FOWG.
- FEMA. (2004). Direct physical damage—general building stock. HAZUS-MH Technical manual, Chapter 5. Washington, D.C: Federal Emergency Management Agency.
- FEMA. (2008). Guidelines for Design of Structures for Vertical Evacuation from Tsunamis - Report P-646. Redwood City, CA: Federal Emergency Management Agency.
- Finney, D. (1971). Probit analysis. Cambridge University Press.
- Folga, S. (2007). Natural Gas Pipeline Technology Overview. Argonne National Laboratory, Environmental Science Division.
- Foster, M., Fell, R., & Spannagle, M. (2011). The Statistics of Embankment Dam Failures and Accidents. Canadian Geotechnical Journal. 1, 1000-1024.
- Fotopoulou, S., & Pitilakis, K. (2013a). Fragility curves for reinforced concrete buildings to seismically triggered slow-moving slides. Soil Dynamics and Earthquake Engineering 48, 143–161.
- Fotopoulou, S., & Pitilakis, K. (2013b). Vulnerability assessment of reinforced concrete buildings subjected to seismically triggered slow-moving earth slides. Landslides 10, 563-582.
- Frazão, S, and Y Zech. (2002). “Dam Break in Channels with 90° Bend. Journal of Hydraulic Engineering 128 (11). American Society of Civil Engineers: 956–68.
- Fread, D L. (1988). BREACH: An Erosion Model for Earthen Dam Failures. National Weather Service, Office of Hydrology. Silver Spring, Md. U.S.A..
- Fritz, H M. (2002). Initial Phase of Landslide Generated Impulse Waves.” Swiss Federal Institute of Technology Zurich (ETHZ).
- Froehlich, D. (2008). Embankment Dam Breach Parameters and Their Uncertainties. Journal of Hydraulic Engineering, American Society of Civil Engineers. 134, 1708–21.
- Fuchs, H. (2013). Solitary Impulse Wave Run-up and Overland Flow. Swiss Federal Institute of Technology Zurich (ETHZ).
- Gee, D., & Brunner, G. (2005). Dam Break Flood Routing Using HEC-RAS and NWS-FLDWAV. In Impacts of Global Climate Change. American Society of Civil Engineers, 1–9.
- Ghobarah, A., Saatcioglu, M., & Nistor, I. (2006). The impact of the 26 December 2004 earthquake and tsunami on structures and infrastructure. Engineering Structures 28, 312–326.
- Grimaldi, S., & Serinaldi, F. (2006). Asymmetric Copula in Multivariate Flood Frequency Analysis. Advances in Water Resources. 29, 1155–67.
- Gruntfest, E., & Pollack, D. (1994). Warnings, mitigation, and litigation: lessons for research from the 1993 flood. Update Water Resour. 95, 40–5.
- Gubinelli, G., Zanelli, S., & Cozzani, V. (2004). A simplified model for the assessment of the impact probability of fragments. Journal of Hazardous Materials. 116, 175-187.
- Gudmestad, O., & Moe, G. (1996). Hydrodynamic coefficients for calculation of hydrodynamic loads on offshore truss structures. Mar Struct. 9, 745–58.

-
- Hager, W.H., & Schleiss A.J.. (2009). *Constuctions Hydrauliques*. Lausanne, Switzerland: Presses polytechniques et universitaires romandes.
- Hartford, D.N.D., & Baecher, G. B. (2004). *Risk and Uncertainty in Dam Safety*. London, U.K.: Thomas Telford Publishing.
- Hatori, T. (1984). On the damage to houses due to tsunamis (in Japanese). *Bulletin of the Earthquake Research Institute*. 59, 433–439.
- HAZUS-MH MR4. (2009). *The Federal Emergency Management Agency's (FEMA's) Methodology for Estimating Potential Losses from Disasters*. National Institute of Building Science, Risk Management Solutions. Menlo Park, CA: Federal Emergency Management Agency.
- Heller, V., Hager W.H., & Minor, H-E. (2009). *Landslide Generated Impulse Waves in Reservoirs. Basics and Computation*” Zurich: Versuchsanstalt für Wasserbau, Hydrologie und Glaziologie (VAW), Swiss Federal Institute of Technology Zurich (ETHZ).
- Heller, V. (2008). *Landslide Generated Impulse Waves: Prediction of near Field Characteristics*. Swiss Federal Institute of Technology Zurich (ETHZ).
- Hendron Jr., A.J., & Patton, F D. (1987). The Vaiont Slide - a Geotechnical Analysis Based on New Geologic Observations of the Failure Surface. *Engineering Geology*. 24, 475–91.
- Hendron Jr., A.J., Ehasz, J.L., & Kermit P. (2006). *Taum Sauk Upper Dam Breach FERC No. P-2277.*, U.S.A.
- Hicks, F E, and Peacock, T. 2005. “Suitability of HEC-RAS for Flood Forecasting.” *Canadian Water Resources Journal / Revue Canadienne Des Ressources Hydriques* 30 (2). Taylor & Francis: 159–74.
- HSE. (2005). *COMAH Guidance for the Surface Engineering Sector*. Health and Safety Executive, UK.
- ICOLD. (1992). *Selection of Design Flood*. Edited by Committee on Design Flood. *Current Methods Bulletin*. Vol. 82. Paris: International Commission on Large Dams (ICOLD).
- ICOLD. (2000). *Reservoir Landslides: Investigation and Management*. Edited by Ad hoc Committee on Reservoir Slope Stability. *ICOLD Bulletin*. Vol. 124. Paris: International Commission on Large Dams (ICOLD).
- ICOLD. (2003). *Dams and Floods: Guidelines and Case Histories*. Edited by Committee on Floods and Dams. *ICOLD Bulletin*. Vol. 125. Paris: International Commission on Large Dams (ICOLD).
- ICOLD. (2012). *Bulletin on Safe Passage of Extreme Floods*. Edited by Committee on Hydraulics for Dams. *ICOLD Bulletin*. Vol. 142. Paris: International Commission on Large Dams (ICOLD).
- ICOLD. (2013). *Guidelines for Use of Numerical Models in Dam Engineering (bulletin 155)*. Technical committee on computational aspects of analysis and design of dams. Paris.
- ICOLD. (2014). *Selecting Seismic Parameters for Large Dams: Guidelines*. Edited by Committee on Seismic Aspects of Dam Design. *ICOLD Bulletin*. Vol. 148. Paris: International Commission on Large Dams (ICOLD).
- Jelínek, R., & Krausmann, E. (2008). *Approaches to tsunami risk assessment*. Luxembourg: EUR 23573 EN, JRC48713.

-
- Kaplan, M., Renaud, F., & Lüchters, G. (2009). Vulnerability assessment and protective effects of coastal vegetation during the 2004 tsunami in Sri Lanka. *Natural Hazards and Earth System Sciences*. 9, 1479–1494.
- Kappos, A., Panagopoulos, G., Panagiotopoulos, C., & Penelis, G. (2006). A hybrid method for the vulnerability assessment of R/C and URM buildings. *Bull Earthq Eng*. 4, 391–419.
- Kosbab, B. (2010). Seismic performance evaluation of port container cranes allowed to uplift. School of Civil and Environmental Engineering, Georgia Institute of Technology.
- Koshimura, S., Oie, T., Yanagisawa, H., & Imamura, F. (2009). Developing fragility functions for tsunami damage estimation using numerical model and post-tsunami data from Banda Aceh, Indonesia”, *Coastal Engineering Journal*. 51, 243–273.
- Kramer, S., Arduino, P., & Shin, H. (2009). Development of performance criteria for foundations and earth structures, *Performance-based design in Earthquake Geotechnical Engineering*, 107-120.
- Krausmann, E. (Ed.) (2014) Report on lessons learned from recent catastrophic events, STREST Deliverable D2.3.
- Krausmann, E., Cozzani, V., Salzano, E., & Renni, E. (2011). Industrial accidents triggered by natural hazards: an emerging risk issue. *Natural Hazards and Earth System Sciences*. 11, 921–929.
- Kreibich, H., Piroth, K., Seifert, I., Maiwald, H., Kunert, U., Schwarz, J., Merz, B., & Thieken, A.H. (2009). Is Flow Velocity a Significant Parameter in Flood Damage Modelling?. *Nat. Hazards Earth Syst. Sci*. 9, 1679-1692
- Landucci, G., Antonioni, G., Tugnoli, A., & Cozzani, V. (2012). Release of hazardous substances in flood events: damage model for atmospheric storage tanks. *Reliability Engineering System Safety*. 106, 200–216.
- Landucci, G., Necci, A., Antonioni, G., Tugnoli, A., & Cozzani, V. (2014). Release of hazardous substances in flood events: Damage model for horizontal cylindrical vessels. *Reliability Engineering and System Safety*. 132, 125-145.
- Lanzano, G., Salzano, E., Santucci De Magistris, F., & Fabbrocino, G. (2013). Seismic vulnerability of natural gas pipelines. *Reliability Engineering & System Safety*. 117, 73-80.
- Lanzano, G., Salzano, E., Santucci de Magistris, F., & Fabbrocino, G. (2014a). Seismic vulnerability of gas and liquid buried pipelines. *Journal of Loss Prevention in the Process Industries*. 28, 72-78.
- Lanzano, G., Santucci de Magistris, F., Fabbrocino, G., & Salzano, E. (2014b). Integrated approach to the seismic vulnerability assessment of industrial underground equipment and pipelines. *Bollettino di Geofisica Teorica ed Applicata*. 55, 215-226.
- Lanzano, G., Santucci De Magistris, F., Fabbrocino, G., & Salzano, E. (2015). Seismic damage to pipelines in the framework of NaTech risk assessment. *Journal of Loss Prevention in the Process Industries*. 33, 159–172.
- Lemperiere, F. (1999). Risk Analysis: What Sort Should Be Applied and to Which Dams?” *International Journal on Hydropower & Dams*. 6, 128–32.

-
- Leone, F., Lavigne, F., Paris, R., Denain, J., & Vinet, F. (2011). A spatial analysis of the December 26th, 2004 tsunami-induced damages: Lessons learned for a better risk assessment integrating buildings vulnerability. *Applied Geography*, 31, 363–375.
- Macabuag, J., Lloyd, T., & Rossetto, T. (2014). Towards the development of a method for generating tsunami fragility functions. *Proceedings of 2nd European Conference on Earthquake Engineering and Seismology*. Istanbul.
- Mander, J. (1988). Theoretical stress-strain model for confined concrete. *J Struct Eng*, 114, 1804–1826.
- Mannam, S. (2005). *Lees' Loss Prevention in the Process Industries, Hazard Identification, Assessment and Control* (3rd Ed. ed.). Burlington, MA: Elsevier Butterworth-Heinemann.
- Mas E., Koshimura, S., Suppasri, A., Matsuoka, M., Matsuyama, M., Yoshii, T., Jimenez, C., Yamazaki, F., & Imamura, F. (2012). Developing Tsunami fragility curves using remote sensing and survey data of the 2010 Chilean Tsunami in Dichato. *Nat. Hazards Earth Syst. Sci.* 12, 2689-2697.
- Matos, J.P., Mignan, A. & Schleiss A.J. (2015). Vulnerability of Large Dams Considering Hazard Interactions: Conceptual Application of the Generic Multi-Risk Framework. In 13th ICOLD International Benchmark Workshop on Numerical Analysis of Dams. Lausanne, Switzerland.
- Mignan, A., Danciu, L., Matos, J.P., & Schleiss, A.J. (2015). Report on Cascading Events and Multi-Hazard Probabilistic Scenarios. Edited by Arnaud Mignan. STREST. Harmonized Approach to Stress Tests for Critical Infrastructures against Natural Hazards. Zurich.
- Mignan, A., Wiemer, S., & Giardini, D. (2014). The Quantification of Low-Probability–high-Consequences Events: Part I. A Generic Multi-Risk Approach. *Natural Hazards*. Springer Netherlands, 1–24.
- Mouyeaux, A., Carvajal, C., Peyras, L., Bressolette, P., Breul, P., & Bacconnet, C. (2015). Probability of Failure of an Embankment Dam due to Slope Instability and Overtopping. In 13th ICOLD International Benchmark Workshop on Numerical Analysis of Dams. Lausanne, Switzerland.
- Müller-Salzburg, L. (1987). The Vajont Catastrophe — A Personal Review. *Engineering Geology*, 24, 423–44.
- Nanayakkara, I., & Dias, P. (2013). Fragility curves for tsunami loading. Special Session on Loading Effects. *Proceedings of 4th International Conference on Structural Engineering and Construction Management*, Kandy, Sri Lanka.
- Neuenhofer, A., & Filippou, F. (1997). Evaluation of nonlinear frame finite-element models. *Journal of Structural Engineering*, 123, 958-966.
- Nurick, G., & Martin, J. (1989). Deformation of thin plates subjected to impulsive loading - a review - Part II: Experimental studies. *Int J Impact Eng*, 8, 171–186.
- O'Rourke, M., & Deyoe, E. (2004). Seismic damage to segment buried pipe. *Earthquake Spectra*, 4, 1167-1183.
- O'Rourke, M., & Liu, X. (1999). *Response of Buried Pipelines Subjected to Earthquake Effect*. University of New York Buffalo: MCEER Monograph No.3.

-
- Papadopoulos, G., & Imamura, F. (2001). A proposal for a new tsunami intensity scale. *Proceedings of International Tsunami Symposium* (pp. 569–577). Seattle, US: IUGG.
- Paquier, A., & O Robin. 1997. "CASTOR: Simplified Dam-Break Wave Model." *Journal of Hydraulic Engineering*. American Society of Civil Engineers. 123. 724–27.
- Peiris, N. (2006). Vulnerability functions for tsunami loss estimation. *Proceedings of 1st European Conference on Earthquake Engineering and Seismology*, (p. Paper No.1121). Geneva, Switzerland.
- Peter, S.J., Siviglia, A., & Boes, R.M. (2015). "Dam Break Analysis under Uncertainty: Introducing BASEbreach." In: 13th ICOLD International Benchmark Workshop on Numerical Analysis of Dams. Lausanne, Switzerland.
- Pilotti, M., Tomirotti M., Valerio G., & Bacchi B. (2010). Simplified Method for the Characterization of the Hydrograph Following a Sudden Partial Dam Break. *Journal of Hydraulic Engineering*. 136, 693–704.
- Pineda-Porras, O., & Najafi, M. (2010). Seismic Damage Estimation for Buried Pipelines: Challenge after Three Decades of Progress. *J. Pipeline Syst. Eng. Pract.* 1, 19-24.
- Pohl, R. (2000). Failure Frequency of Gates and Valves at Dams and Weirs. *International Journal on Hydropower & Dams*. 6, 77–81.
- Reese, S., Bradley, B. A., Bind, J., Smart, G., Power, W., & Sturman, J. (2011). Empirical building fragilities from observed damage in the 2009 South Pacific tsunami, *Earth-Science Reviews*. 107, 156–173.
- Rossetto, T., Peiris, N., Pomonis, A., Wilkinson, S., Del Re, D., & Koo, R. E. (2007). The Indian Ocean tsunami of December 26, 2004: observations in Sri Lanka and Thailand. *Natural Hazards*. 42, 105–124.
- Salzano, E., & Basco, A. (2015). Simplified model for the evaluation of the effects of explosions on industrial target. *Journal of Loss Prevention in the Process Industries*. 37, 119–123.
- Salzano, E., & Cozzani, V. (2007). Quantitative Risk Assessment of Industrial Processes: The Path Towards a Global Approach. In L. G. Mason (Ed.), *Focus on Hazardous Materials Research* (pp. 25-47). New York: Nova Science Publishers.
- Salzano, E., Basco, A., Busini, V., Cozzani, V., Renni, E., & Rota, R. (2013). Public Awareness Promoting New or Emerging Risk: Industrial Accidents Triggered by Natural Hazards. *Journal of Risk Research*. 16, 469-485.
- Salzano, E., Garcia-Agreda, A., Di Carluccio, A., & Fabbrocino, G. (2009). Risk assessment and early warning systems for industrial facilities in seismic zones. *Reliab. Eng. Syst. Saf.* 94, 1577-1584.
- Salzano, E., Iervolino, I., & Fabbrocino, G. (2003a). Seismic risk of atmospheric storage tanks in the framework of Quantitative Risk Analysis. *Journal of Loss Prevention in the Process Industry*. 16, 403-409.
- Salzano, E., Picozzi, B., Vaccaro, S., & Ciambelli, P. (2003b). The hazard of pressure tanks involved in fires. *Ind Eng Chem Res.* 42, 1804-1812.
- Sarrasin, O. (2015). Numerical Simulation and Evaluation of the Risk Posed by Impulse Waves on the Mattmark Reservoir. *École Polytechnique Fédérale de Lausanne*.

Schleiss, A.J., & Pougatsch H. (2011). *Les Barrages. Du Projet À La Mise En Service*. Lausanne, Switzerland: Presses polytechniques et universitaires romandes.

SeismoSoft. (2015). A computer program for static and dynamic nonlinear analysis of framed structures. (SeismoStruct, Ed.) Retrieved from www.seismosoft.com

Seligson, H., Eguchi, R., Tierney, K., & Richmond, K. (1996). Chemical Hazards, mitigation and preparedness in areas of high seismic risk; a methodology for estimating the risk of postearthquake hazardous materials release. State University of NY. Buffalo: National Center for Earthquake Engineering Research.

Shuto, N. (1994). Tsunami intensity and disasters. In S.Tinti, *Tsunamis in the World* (p. 197–216). Dordrecht: Kluwer Academic Publisher.

Soares-Frazão, Sandra, & Yves Zech. (2008). Dam-Break Flow through an Idealised City. *Journal of Hydraulic Research*. 46, 648–58.

Stansfield, K. (2005). Effects of the Asian tsunami on structures. *Journal of Structural Engineering*. 83, 20–21.

Suppasri, A., Koshimura, S., & Imamura, F. (2011). Developing tsunami fragility curves based on the satellite remote sensing and the numerical modeling of the 2004 Indian Ocean tsunami in Thailand. *Natural Hazards Earth System Science*. 11, 173-189.

Suppasri, A., Mas, E., Charvet, I., & Gunasekera, R. (2013). Building damage characteristics based on surveyed data and fragility curves of the 2011 Great East Japan tsunami. *Nat Hazards*. 66, 319–341.

Suppasri, A., Mas E., Charvet I., Gunasekera, R., Imai, K., Fukutani, Y., Abe, Y., & Imamura, F. (2013). Building Damage Characteristics Based on Surveyed Data and Fragility Curves of the 2011 Great East Japan Tsunami. *Natural Hazards*. 66, 319–41.

Talasilidis, D.G., Manolis, G.D., Paraskevopoulos, E., Panagiotopoulos, C., Pelekasis, N., & Tsamopoulos, J.A. (2004). Risk analysis of industrial structures under extreme transient loads. *Soil Dynamics & Earthquake Engineering*. 24, 435–448.

Tilton, J. (1999). Fluid and particle dynamics. In *Perry's Chemical Engineers' Handbook*. 7th Ed. New York: McGraw-Hill.

Timoshenko, S., & Gere, J. (1961). *Theory of elastic stability*. 2nd Ed. New York: McGraw Hill.

Tinti, S., Tonini, R., Bressan, L., Armigliato, A., Gardi, A., Guillande, R., Valencia, N., & Scheer S., (2011). *Handbook of Tsunami Hazard and Damage Scenarios*. Luxembourg.

Tromans, I. (2004). Behavior of buried water supply pipelines in earthquake zones (PhD Thesis). London: Imperial College of Science, Technology and Medicine, University of London.

Tugnoli, A., Cozzani, V., Khan, F., & Amyotte, P. (2013). P. 6 – Missile Projection Effects. In V. Cozzani, & G. Reniers, *Domino Effects in the Process Industries, Modelling, Prevention and Managing* (pp. 116–153).

Valencia, N., Gardi, A., Gauraz, A., Leone, F., & Guillande, R. (2011). New tsunami damage functions developed in the framework of SCHEMA project: application to European-Mediterranean coasts. *Nat. Hazards Earth Syst. Sci*. 11, 2835–2846.

Vetsch, D., Fäh, R., Farshi, D., & Müller, R. (2005). BASEMENT - an Object-Oriented Software System for the Simulation of Natural Hazards." In Festtagskolloquium 75 Jahre VAW. Zurich, Switzerland: Mitteilung VAW 190, Swiss Federal Institute of Technology Zurich (ETHZ).

Volz, C. (2013). Numerical Simulation of Embankment Breaching due to Overtopping. Swiss Federal Institute of Technology Zurich (ETHZ).

Wahl, T.L. (2004). Uncertainty of Predictions of Embankment Dam Breach Parameters. Journal of Hydraulic Engineering. 130, 389–97.

Westberg W., & Borragan V. (2015). Theme B: System Approach to Probability of Failure of an Embankment Dam. In 13th ICOLD International Benchmark Workshop on Numerical Analysis of Dams. Lausanne, Switzerland.

Wurbs, R. (1987). Dam-Breach Flood Wave Models. Journal of Hydraulic Engineering. 113,29–46.